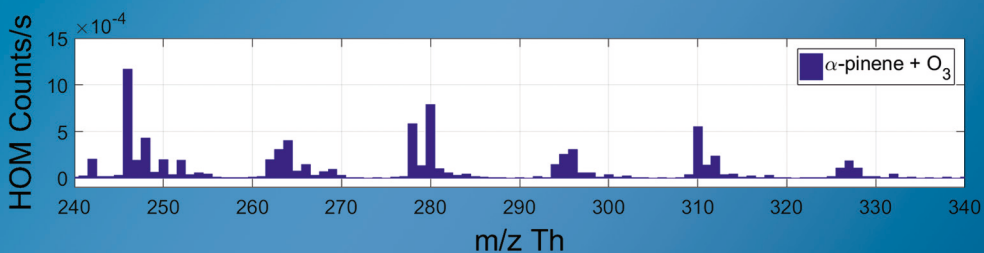
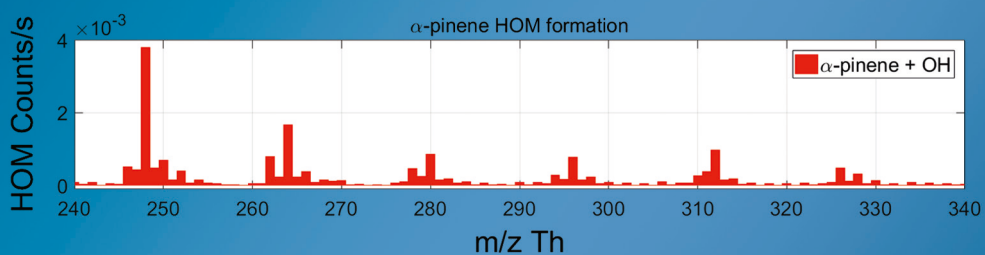


# Photochemistry of Highly Oxidized Multifunctional Organic Molecules: a Chamber Study

Laura Iida Maria Pullinen



Energie & Umwelt/  
Energy & Environment  
Band/ Volume 387  
ISBN 978-3-95806-260-3

Photochemistry  
of  
Highly Oxidized Multifunctional Organic Molecules:  
a Chamber Study

Inaugural-Dissertation  
zur  
Erlangung des Doktorgrades  
der Mathematisch-Naturwissenschaftlichen Fakultät  
der Universität zu Köln

vorgelegt von  
Laura Iida Maria Pullinen  
aus Iitti

Cologne, 2017

Berichterstatter: Prof. Dr. Andreas Wahner

PD Dr. Mathias Schäfer

Prüfungsvorsitzender: Prof. Dr. Tibor Dunai

Beisitzer: Dr. Michael von Papen

Tag der mündlichen Prüfung: 24.10.2016



Forschungszentrum Jülich GmbH  
Institute of Energy and Climate Research  
Troposphere (IEK-8)

# Photochemistry of Highly Oxidized Multifunctional Organic Molecules: a Chamber Study

Laura Iida Maria Pullinen

Schriften des Forschungszentrums Jülich  
Reihe Energie & Umwelt / Energy & Environment

Band / Volume 387

---

ISSN 1866-1793

ISBN 978-3-95806-260-3

Bibliographic information published by the Deutsche Nationalbibliothek.  
The Deutsche Nationalbibliothek lists this publication in the Deutsche  
Nationalbibliografie; detailed bibliographic data are available in the  
Internet at <http://dnb.d-nb.de>.

Publisher and  
Distributor: Forschungszentrum Jülich GmbH  
Zentralbibliothek  
52425 Jülich  
Tel: +49 2461 61-5368  
Fax: +49 2461 61-6103  
Email: [zb-publikation@fz-juelich.de](mailto:zb-publikation@fz-juelich.de)  
[www.fz-juelich.de/zb](http://www.fz-juelich.de/zb)

Cover Design: Grafische Medien, Forschungszentrum Jülich GmbH

Printer: Grafische Medien, Forschungszentrum Jülich GmbH

Copyright: Forschungszentrum Jülich 2017

Schriften des Forschungszentrums Jülich  
Reihe Energie & Umwelt / Energy & Environment, Band / Volume 387

D 38 (Diss., Köln, Univ., 2017)

ISSN 1866-1793  
ISBN 978-3-95806-260-3

The complete volume is freely available on the Internet on the Jülicher Open Access Server (JuSER)  
at [www.fz-juelich.de/zb/openaccess](http://www.fz-juelich.de/zb/openaccess).



This is an Open Access publication distributed under the terms of the [Creative Commons Attribution License 4.0](https://creativecommons.org/licenses/by/4.0/),  
which permits unrestricted use, distribution, and reproduction in any medium, provided the original work is properly cited.

## Zusammenfassung

Hoch oxidierte multifunktionale Moleküle (HOMs) sind eine Klasse von Molekülen deren Existenz in der Gasphase erst kürzlich nachgewiesen wurde. Wegen ihrer hohen O:C Verhältnisse haben HOMs geringe Dampfdrücke und spielen sie eine bedeutende bei der Neubildung von Partikeln und deren Wachstum. Mit dem Ziel ein besseres Verständnis der Mechanismen der Partikelbildung zu erhalten, wurden in dieser Arbeit die photochemische Bildung von HOMs, deren chemische Umwandlungen sowie deren Verlustprozesse untersucht.

OH ist das hauptsächliche Oxidationsmittel in der Troposphäre. Trotzdem wurde die photochemische Bildung von HOMs bislang nicht intensiv untersucht, sondern hauptsächlich deren Bildung aus der Ozonolyse. Es stellte sich daher die Frage nach der Bedeutung der Photochemie bei der Bildung der HOMs. In Fokus der Arbeiten stand die HOM Bildung aus  $\alpha$ -Pinen, es wurde aber auch die photochemische HOM Bildung aus  $\beta$ -Pinen, Methyl salicylat und Benzol nachgewiesen. Methyl salicylat und Benzol haben keine Doppelbindung und reagieren somit nicht mit Ozon. Der Nachweis der HOM Bildung aus diesen bedeutenden biogen- bzw. anthropogen emittierten Verbindungen weist darauf hin, dass auch Reaktionen mit OH eine wichtige Quelle für HOMs sind.

Dominierender Mechanismus der photochemischen HOM Bildung ist die Autoxidation, d.h. die sequentielle Anlagerung von  $O_2$  an Alkylradikale, die sich nach interner H-Migration aus Peroxy- oder Alkoxyradikalen bilden. Die Autoxidation muss sehr effektiv ablaufen da eine Verringerung der  $O_2$  Mischungsverhältnisse auf unter 1% keinen Einfluss auf die HOM Bildung zeigte.

Sequentielle Reaktionen mit OH sind weniger bedeutend obwohl die weitere Oxidation von in hohen Konzentrationen auftretenden Oxidationsprodukten als Quelle von HOMs nicht ausgeschlossen ist. Die Ausbeute von HOMs aus der Photooxidation von  $\alpha$ -Pinen sind abhängig von der OH Konzentration und wurden zu 1.8 and 7% abgeschätzt.

Die Zugabe von Stickoxiden ( $NO_x$ ) führte zur Bildung organischer Nitratre und zu insgesamt verstärkter HOM Bildung. Die Bildung der organischen Nitratre bestätigte die vorherige Zuordnung der Moleküle als Peroxyradikale, Hydroperoxyde und Ketone. Die insgesamt verstärkte HOM Bildung kam durch erhöhtes [OH] zustande was seinerseits auf die Rezyklierung von OH über die Reaktion von NO mit  $HO_2$  zurückgeführt wurde. Auch bei sehr hohen [NO $_x$ ] konnte die Bildung von Terminierungsprodukten aus  $RO_2 + RO_2$  Reaktionen nachgewiesen werden. Grund hierfür ist wahrscheinlich eine Rückbildung von Peroxyradikalen aus Alkoxyradikalen die nicht zerfallen. H-Migration im Alkoxyradikal führt zu einem Alkylradikal und nachfolgender Anlagerung von  $O_2$  und Bildung eines Peroxyradikals. Wie auch Experimente mit CO zeigten, folgt die Umwandlung von HOMs der klassischen Vorstellung der Chemie von Peroxyradikalen.

Wichtige Senke für HOMs ist deren Kondensation auf Partikeln. Hierfür wurden effektive Aufnahmekoeffizienten bestimmt. Für Monomere lagen diese im Bereich von 0.5-0.9 Für Dimere bei eins. Schon bei Massendichten von etwa  $3 \mu g m^{-3}$  konnte die Beeinflussung der Chemie von Peroxyradikalen durch Partikel gezeigt werden. Möglicherweise ist dieser Einfluss in der realen Atmosphäre stärker als in der genutzten Reaktionskammer, zur Abschätzung der Bedeutung dieses Einflusses bedarf es aber mehr Experimente als in dieser Arbeit durchgeführt werden konnten.

## Abstract

Highly oxidized multifunctional organic molecules (HOMs) are a newly-found class of compounds that are formed in volatile organic compound (VOC) oxidation. Due to high O:C ratios of the HOMs, they are suggested to participate in atmospheric processes, such as new particle formation (NPF) and particle mass formation. Thus studying HOMs gives important insight into mechanisms of particle formation and growth under different chemistry regimes.

OH is the main oxidant during daytime chemistry, however so far the photochemical HOM formation has not been studied in detail. This study focusses on the photochemical HOM production from  $\alpha$ -pinene, on chemical transformation of HOMs as well as on their loss processes.

Autoxidation was found to be a dominant process of photochemical HOM formation. However, comparison of the photochemical HOM patterns from  $\alpha$ -pinene and its main primary oxidation product pinonaldehyde showed that also secondary OH oxidation is likely to contribute to some extent. In one experiment the oxygen content of the chamber during the experiment was lowered below 1% and the HOM formation was not affected, which indicates that autoxidation must be very fast.

OH oxidation of pinonaldehyde,  $\beta$ -pinene, cyclohexene, benzene, and methyl salicylate led to HOM formation. If at all, these compounds do not react efficiently with ozone, suggesting that photooxidation might be a source of HOMs in general. The effect of photochemistry on HOM formation from  $\alpha$ -pinene was studied in more detail. The yield of HOMs from  $\alpha$ -pinene photooxidation was found to depend on [OH] and estimated to be between 1.8 and 7%.

Adding  $\text{NO}_x$  led to the formation of organic nitrates as well as to a general increase of HOM formation. The formation of organic nitrates confirmed the assignment of HOMs being peroxy radicals. The general increase of HOM formation observed up to moderate  $\text{NO}_x$  levels was mainly due to OH recycling by  $\text{HO}_2 + \text{NO}$  reactions leading to increased [OH]. Additionally, the presence of  $\text{NO}_x$  also activated the "alkoxy-peroxy pathway". Alkoxy radicals formed in reactions of NO with peroxy radicals might undergo internal H-shifts and subsequent  $\text{O}_2$  additions, instead of degrading. This pathway can form peroxy radicals and explain why even at very high [NO $_x$ ] there were still termination products of  $\text{RO}_2 + \text{RO}_2$  reactions observable.

High [ $\text{HO}_2$ ] favoured hydroperoxide formation and diminished formation of other termination products. Altogether, the behaviour of HOMs was compatible to classical models of peroxy radical chemistry. Effective uptake coefficients for HOMs on particles were determined to be in the range of 0.5-0.9 for monomers and unity for dimers. At mass loads above  $\sim 3 \mu\text{g m}^{-3}$  impacts of particles on peroxy radical chemistry became obvious suggesting an impact of particles on photochemistry also under atmospheric conditions.

# Table of Contents

Zusammenfassung	V
Abstract	VI
Table of Contents	VII
1. Introduction	1
1.1. Highly oxidized multifunctional organic molecules (HOMs) in the atmosphere	1
1.2. Formation mechanism of highly oxidized multifunctional organic molecules via ozonolysis	3
1.3. Volatile organic compounds (VOC) in atmospheric photochemistry	5
2. Methods and experimental set-up	10
2.1. Experiment set-up	10
2.1.1. Jülich Plant Atmosphere Chamber	10
2.1.2. General instrumentation	12
2.2. Chemical ionization mass spectrometer	12
2.2.1. Instrument introduction	12
2.2.2. Calibration	17
2.3. Experiment protocols	19
2.3.1. Experiment overview	20
3. Photochemical HOM formation mechanism: Sequential oxidation versus autoxidation	25
3.1. HOM formation and autoxidation: setting the problem	25
3.2. Cyclohexene versus cyclohexene-d10	26
3.3. Monoterpenes: $\alpha$ -pinene	27
3.3.1. Photochemical HOM formation $\alpha$ -pinene	27
3.3.2. HOM formation from secondary OH oxidation: pinonaldehyde	29
3.4. HOM formation rate comparison	31
3.5. Effect of OH concentration on end product pattern	32
3.6. Conclusion: Autoxidation versus sequential oxidation	34
3.7. Experiment to study the role of O <sub>2</sub> in the photochemical HOM formation	34
3.8. Photochemical HOM formation under reduced influence of ozonolysis	37
3.8.1. Photochemical HOM formation from $\beta$ -pinene	37
3.8.2. Photochemical HOM formation from methyl salicylate and benzene	38
4. Photochemical HOM production	41
4.1. OH dependency of photochemical HOM from $\alpha$ -pinene	41
4.2. Yield estimation from photochemical HOM production from $\alpha$ -pinene	50
4.3. Photochemical HOM production from exocyclic double bonds: $\beta$ -pinene	52
4.4. Concluding remarks on photochemical HOM production	54

5. Chemical transformation of HOMs	55
5.1. Photochemistry of $\alpha$ -pinene in the presence of $\text{NO}_x$	55
5.1.1. Formation of organic nitrates and PAN-like nitrates	58
5.1.2. The effect of $\text{NO}_x$ on peroxy radical chemistry	59
5.2. Photochemistry of $\beta$ -pinene in the presence of $\text{NO}_x$	68
5.3. CO + HOMs	71
5.4. Concluding remarks on chemical transformation HOMs	77
6. Sinks of HOMs: condensation on particles and wall loss	79
6.1. Condensation on particles	82
6.2. Concluding remarks	91
7. Summary and Conclusions	93
References	i
Appendix	viii
Abbreviations	xv
Acknowledgements	xvii

# Chapter 1 Introduction

## 1.1 Highly oxidized multifunctional organic molecules in the atmosphere

Volatile organic compounds (VOC) are important players in atmospheric chemistry. VOC are emitted either from biogenic or anthropogenic sources. They are mainly pure hydrocarbons and are easily oxidized by the major atmospheric oxidants, OH, ozone and NO<sub>3</sub>. The oxidation products of VOC contribute to the formation of secondary organic aerosols (SOA), either by condensation of existing particles or by new particle formation. The oxidation products formed according to established understanding of atmospheric VOC oxidation (e.g. Master Chemical Mechanism 3.3.1.) have too low oxygen content and are thus too volatile to directly contribute to SOA formation. However, the oxygen number is crucial, as increasing the amount of oxygen in a molecule will lower its vapour pressure making it less volatile. So, high oxidation degree of the oxidation products is required to participate in particle formation and growth. It was proposed, that higher oxidation degrees should be achieved by sequential, multiple oxidation of the first generation oxidation products by the OH radical. Besides chemical ageing via sequential oxidation, accretion reactions in the particle phase are forming high molecular oligomers with low vapour pressures (Hallquist et al., 2009).

The search for the non-volatile organic molecules explaining the observed new particle and SOA formation received a new angle when Ehn et al. (2010; 2012; 2014) discovered a new class of organic molecules in measurements made in Hyttiälä, SMEAR II boreal forest measurement station (Finland). Using a new instrument called Atmospheric Pressure interface Time of Flight Mass Spectrometer (API-TOF-MS) they detected a group of naturally negatively charged organic molecules dominating the night-time spectrum at masses between 280-650 Th. These molecules had very high O/C ratios, and were named highly oxidized multifunctional molecules (HOMs)

Several studies show that observed HOMs are obviously produced very fast by  $\alpha$ -pinene *ozonolysis* in gas phase, i.e. by reaction of a monoterpene (a VOC class with large atmospheric source strength) with one of the major atmospheric oxidants, O<sub>3</sub> (Jokinen et al., 2014; Mentel et al., 2015; Rissanen et al., 2015; Berndt et al., 2015; Kurtén et al., 2015).

The atmospheric relevance of HOMs is based on their role in the formation of secondary organic aerosols (SOA) because SOA themselves are important atmospheric compounds. Atmospheric aerosols (particles and the surrounding gas medium) in general have effect on human health and on climate (Nel, 2005; IPCC, 2013). They can scatter and absorb solar radiation, and act as cloud condensation nuclei (CCN), as well as regulate cloud properties (Rosenfeld et al., 2008; Clement et al., 2009). Aerosol particles are also counted as pollution deteriorating air quality (Nel, 2005). A large fraction (up to 90%) of atmospheric sub-micrometre particle mass consists of organic compounds (Jimenez et al., 2009).

To assess the relevance of HOMs on SOA formation it is required to understand the role of organic vapours in new particle formation (NPF) and particle growth, as well as on CCN formation. It was long believed that sulfuric acid is driving new particle formation (Kulmala et al., 2004; Weber et al., 1996; Kerminen et al., 2010; Sipilä et al., 2010), and atmospheric SA has been showed to be linked to particle

formation and growth (Kulmala et al., 2013). However there was a need for additional vapours, likely organic, to explain observed particle formation and growth rates (Kurtén et al., 2008; Loukonen et al., 2010; Ortega et al., 2016; Paasonen et al., 2012; Kulmala et al., 2013), and the role of organic vapours had been hypothesised and tested before (Hoffmann et al., 1998; Yu et al., 1999; Metzger et al., 2010; Paasonen et al., 2010; Wang et al., 2010; Riipinen et al., 2011). ). Also the location of NPF (often clean atmosphere at forested regions with low SA concentration) gives reason to believe SA alone cannot explain all particle formation events (Zhang et al., 2004; Metzger et al., 2010; Paasonen et al., 2010; Donahue et al., 2011; Riipinen et al., 2011, 2012; Ehn et al., 2012, 2014; Riccobono et al., 2014; Schobesberger 2013; Kulmala et al., 2013). However, directly measuring these theorized organic compounds was not possible until development of API-TOF-MS.

Ehn et al. (2014) report on the role of organics (HOMs) on SOA mass formation, and to highlight it they introduce a new concept, extremely low-volatility organic compound (ELVOC), in analogy to the style of pre-existing terms such as low-volatility organic compounds (LVOC) and semi-volatile organic compounds (SVOC). Due to structural properties HOMs are suggested to irreversibly condense on particles, and thus contribute to the growth. The relative importance of HOMs to growth was highest at low particle loading/surface, when nearly all of the growth could be attributed them. Ehn et al. (2014) compar measurements from AMS (Aerosol Mass spectrometer) to the HOMs data, and offer the similarity of O/C and H/C ratios of HOMs to those measured from formed SOA as further evidence of the role of HOMs on particle growth.

From these studies it can be concluded that in the critical range of particle growth, presence of HOMs in the atmosphere can differentiate whether particles grow to relevant sizes. The studies mentioned here concentrate on clean boreal atmosphere (Kulmala et al. 2013) and monoterpene ozonolysis (Ehn et al., 2014), so the importance of HOMs and organics on SOA formation in more polluted areas cannot be concluded yet. HOMs are the (at least one of the) group of organic vapours that have been suggested to be relevant in NPF (Schobesberger et al., 2013; Ehn et al., 2014; Jokinen et al., 2015; Tröstl et al., 2016; Bianchi et al., 2016).

To conclude, Figure 1.1 depicts the relative importance of different vapours in the atmosphere to particle formation and growth as suggested by Ehn et al. (2014). As can be seen, at the very small scale, clusters of few molecules, sulphuric acid and amines/ammonia constitute most of the particle. When the cluster grows, organic vapours (ELVOC/HOMs) begin to contribute to growth, until the particle is large enough and eventually also low-volatility and semi-volatility organic compounds begins to condense, and contribute to growth. Ehn et al. (2014) show results from ambient measurements at Hyytiälä SMEAR II forest station to show how the HOM concentrations measured are abundant enough to explain the growth of particles in the range of 5-50 nm.

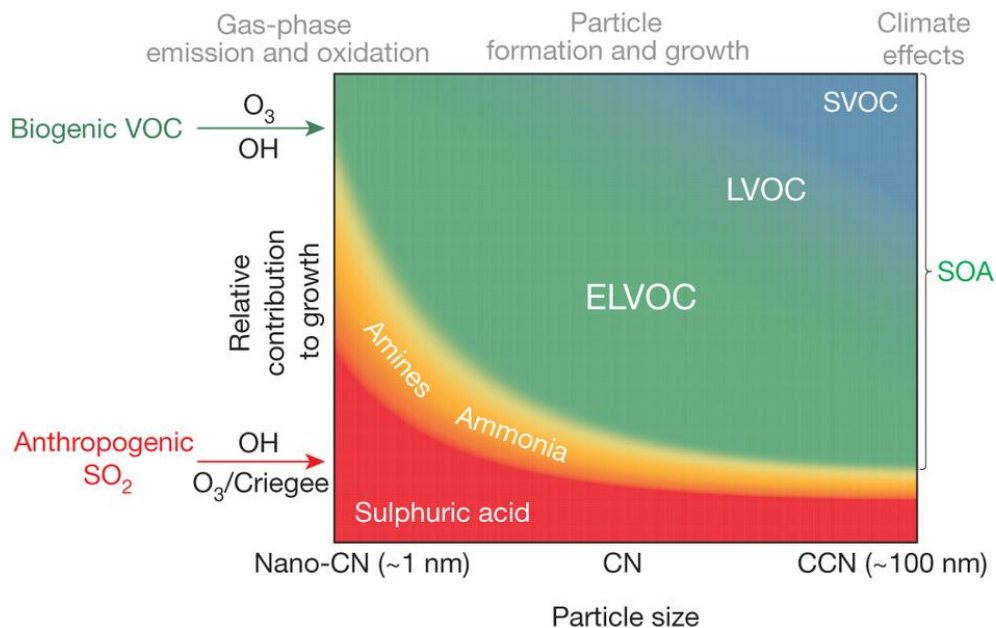


Figure 1.1 Relative importance of ELVOC to particle growth (Ehn et al., 2014).

## 1.2. Formation mechanism of oxidized multifunctional organic molecules via ozonolysis.

Ozone is one of the main oxidants during night time chemistry, and a tropospheric pollutant. It is also involved in primary OH production (R1.3a-b) and it has two important sources in the troposphere. One source is the intrusion from the Stratosphere leading to a background level; the other is photochemical ozone production. Main precursor of O<sub>3</sub> during photochemical production is NO<sub>2</sub> that can be photolyzed at wavelengths below 430 nm:



Ozone is reactive towards VOC with C=C double bond, such as unsaturated alkenes.



The formed peroxy radical then has classical pathways to terminate (see R1.3c-R1.3i).

It has been established that ozonolysis produces highly oxidized multifunctional compounds, HOM (Ehn et al., 2012; Ehn et al., 2014; Jokinen et al., 2014; Mentel et al., 2015; Berndt et al., 2015; Rissanen et al., 2015; Hyttinen et al., 2015). The pathway to ozonolysis HOM formation has been suggested to be

autoxidation and peroxy radical formation (i.e. Ehn et al., 2012, 2014; Mentel et al., 2015; Rissanen et al., 2015).

Mentel et al. (2015) suggest a detailed mechanism of alkene ozonolysis HOM formation. Ozonolysis of endocyclic double bond containing alkenes leads to opening of the ring structure, with Criegee intermediate on one end of the chain, and carbonyl group on the other. The Criegee radical further reacts via several pathways, from which the formation of vinylhydroperoxide is highlighted. When decomposing, vinylhydroperoxide forms a radical with mesomeric structures, and an O<sub>2</sub> addition leads to an oxo-alkyl radical i.e. to a peroxy radical with four oxygens. This vinylhydroperoxide pathway is the starting point of their consideration as HOM compound.

H-shifting ability of C-H bond for peroxy radicals is assumed, which allows addition of O<sub>2</sub> into the molecule, and will lead to a peroxy radical with -OOH functionality. This process is known from high temperature reactions (Cox & Cole, 1985; Glowacki & Pilling, 2010; Jorand et al., 2003; Perrin et al., 1998)), but was not considered of importance at atmospheric conditions until recently (Crouse et al., 2012; 2013). Mentel et al. (2015) conclude that most ozonolysis HOM result from internal H-shift and subsequent O<sub>2</sub> addition of the peroxy radical, combined with intramolecular rearrangement. This addition of O<sub>2</sub> into the molecule would account for the 32 Th progressions observed in ozonolysis HOM spectra, and this process only requires one initial attack by ozone and further oxidation occurs with intramolecular H-shift and molecular O<sub>2</sub> addition. This sequential internal H-shift and addition of molecular O<sub>2</sub> into a compound is what is meant by term “autoxidation” later in this work.

In parallel to internal H-shift and subsequent O<sub>2</sub> addition, the HOM peroxy radicals can undergo termination reactions leading to closed shell HOMs, i.e. HOMs that are no longer radicals but chemically stable molecules. For all peroxy radicals formed by H-shift and subsequent O<sub>2</sub> addition the classical peroxy radical chemistry pathways apply and typical termination products are ketones, alcohols, hydroperoxides, and percarboxylic acids (as shown later, Figure 1.4).

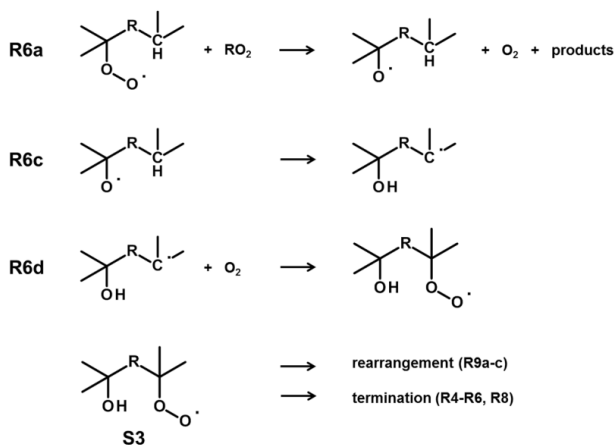


Figure 1.2 Alkoxy-peroxy pathway of alkoxy radical (Mentel et al., 2015).

According to classical peroxy radical chemistry also alkoxy radicals are formed in peroxy radical-peroxy radical reactions. Also alkoxy radicals can undergo H-shifts with the formation of an alkyl radical at which an O<sub>2</sub> molecule is added (Vereecken & Peeters, 2010; Vereecken & Francisco 2012). The forming peroxy radical has one O atom more than the “parent” peroxy radical, and is shown to be of minor importance in case of HOM formation from ozonolysis (Mentel et al., 2015). But as shown in Chapter 5, this pathway is relevant for the results later shown in this work. It will therefore be given a notice here (Figure 1.2). The alkoxy radical RO<sup>•</sup> formed in reaction R1.3h (R6a in Figure 1.2) can undergo intramolecular rearrangement (internal H-shift) and attain O<sub>2</sub>, forming hydroxyl-peroxy radical, with three oxygens attached. This can then terminate in accordance with classical peroxy radical pathways, or experience further rearrangement. In this work the term alkoxy-peroxy pathway is used to refer to this pathway.

The vinylhydroperoxy radical pathway combined with further autoxidation can explain progressions of 32 Th observed in data where the formed HOM molecule has an even number of oxygen, while the alkoxy-peroxy pathway and autoxidation would be plausible explanations for the progression of 32 Th in HOM with odd number of oxygen in the molecule. In the case of ozonolysis formed HOM, most are with even number of oxygen, but with OH it is not as simple, and thus the latter pathway may gain importance.

### 1.3. Volatile organic compounds (VOC) in atmospheric photochemistry

Up to now it is evident that HOM are formed by ozonolysis of endocyclic (biogenic) molecules, and the principle pathways via autoxidation are more or less established. However, in the atmosphere the OH radical is the main oxidant of volatile organic compounds during atmospheric daytime chemistry.

Formation of OH in the atmosphere occurs via ozone photolysis (primary OH production):



OH is unreactive towards O<sub>2</sub>, N<sub>2</sub>, CO<sub>2</sub> or H<sub>2</sub>O, which is why it “survives” in the atmosphere long enough to react with VOC and other trace gasses. Additional to reaction R1.3b, OH is also produced in the atmosphere in HONO photolysis and secondary sources (photolysis of CH<sub>2</sub>=O and HO<sub>2</sub>) in catalytic cycles, which means that it regenerates in the same cycle of reactions that consume it, leading to daytime concentrations in the order of 10<sup>6</sup> cm<sup>-3</sup>.

VOC reactions with OH consume OH in the atmosphere, but VOC also affect OH budget in other ways. For example alkene ozonolysis produces OH (Atkinson, 1997). Alkene ozonolysis can be an important source for atmospheric OH during night-time and, in laboratory experiments, a source for OH during ozonolysis.

Unlike ozone, for example, that requires a carbon double bond where to attack, OH is less selective as a reactant. Although OH mainly attacks a VOC at the double bond (e.g. monoterpenes) it can also abstract hydrogen atoms (for  $\alpha$ -pinene and  $\beta$ -pinene  $\sim 10\%$  of attacks at double bond, MCM version 3.3.1.). OH can also attack C-H bonds in molecules without double bonds. It is therefore also possible that a VOC can be sequentially oxidized by OH even after reaction of the double bond. Addition of OH to double bonds or H-abstraction leads to peroxy radicals (see below R1.3c, R1.3b), which can then undergo autoxidation. This makes it more difficult to find out the pathways of HOM formation from OH initiated VOC oxidation.

A further aspect of photo-oxidation that is important for the interpretation of the results is the impact of  $\text{NO}_x$  ( $\text{NO}_x = \text{NO} + \text{NO}_2$ ) on photochemical systems. NO can react with peroxy radicals. In this reaction  $\text{NO}_2$  is formed without loss of an ozone molecule in contrast to the fast reaction of NO with  $\text{O}_3$ , making the reaction of peroxy radicals with NO to an important source for Tropospheric ozone. Figure 1.3 sketches the basic reaction pathways mentioned so far.

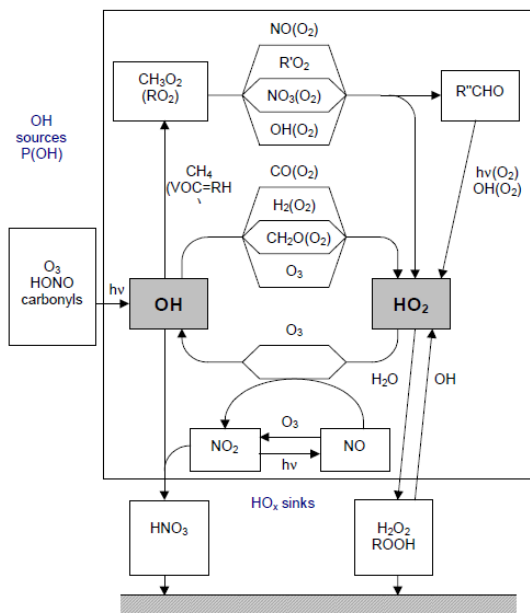


Figure 1.3 Simplified overview on tropospheric OH chemistry (Geyer, 2000).

Photooxidation is at first described for H abstraction (R1.3c):



Where RH is the VOC, R<sup>·</sup> is alkyl radical, and RO<sub>2</sub><sup>·</sup> represents the peroxy radical that is formed from the alkyl radical after addition of O<sub>2</sub>. An overview of the VOC oxidation pathway is shown in Figure 1.4.

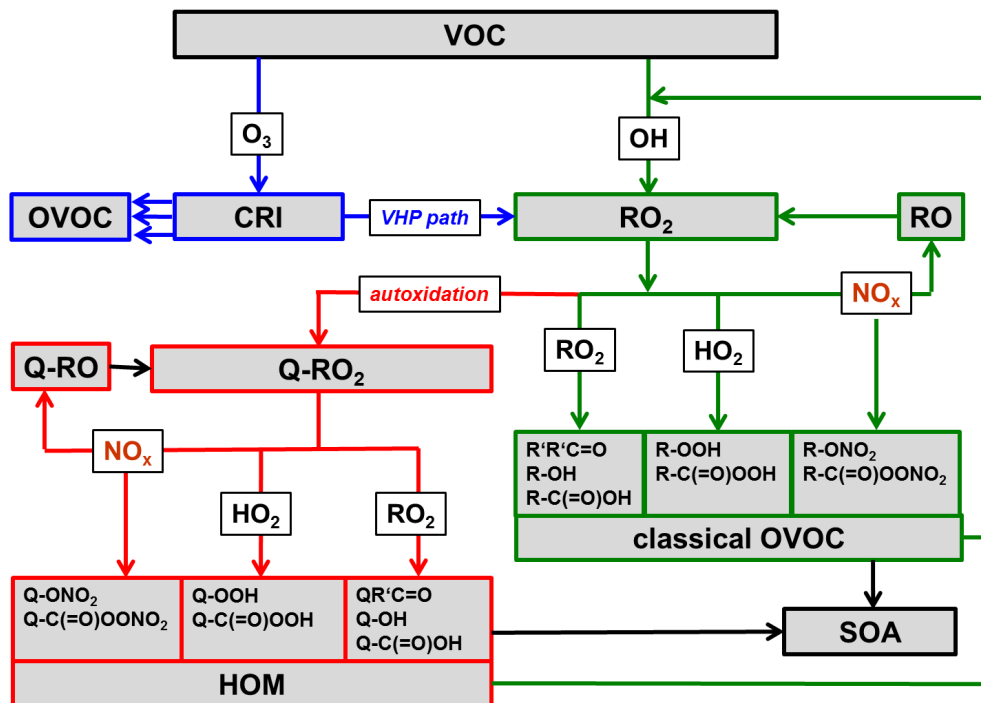


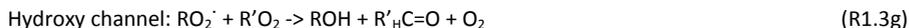
Figure 1.4 Pathways of VOC oxidation. Ozonolysis (blue arrows) also leads to Criegee reactive intermediates (CRI) which on several pathways can form OVOC, similar to those from OH. The vinylhydroperoxide (VHP) path leads to peroxy radicals which can undergo autoxidation. The green frames indicate the established OVOC formation pathway via peroxy radicals (RO<sub>2</sub>) induced by the OH radical. The red frames show the newly discovered additional pathway via autoxidation (H-shift + O<sub>2</sub> addition). The HOM termination scheme is supposedly similar to the classical scheme, however, the very fast autoxidation process led to higher O/C and functionalization as indicate by using Q. The introduction of NO<sub>x</sub> in both subsystems increases the importance of alkoxy radicals. OH can sequentially oxidize OVOC to higher oxidation products. Once the vapour pressure is sufficiently low, HOMs (and OVOC) condense and form SOA.

The fate of the  $\text{RO}_2\cdot$  depends on the atmospheric conditions. When considering low  $\text{NO}_x$  conditions, the peroxy radical chemistry runs via several (termination) pathways.

Hydroperoxy channel:



Carbonyl channel:



Alkoxy channel:



Additional to these there is the dimerization pathway



Where  $\text{RO}_2\cdot$  and  $\text{R}'\text{O}_2\cdot$  can be same or different peroxy radicals.

Presence of  $\text{NO}$  into the system introduces more channels, and those will be further discussed in Chapter 5. Shortly, organic nitrates and alkoxy radicals are formed:



Addition of  $\text{NO}$  in the system has also direct impact on  $\text{OH}$  concentrations.  $[\text{OH}]$  is enhanced via reaction R5.1d, and decreased by reaction R5.1e. At low  $[\text{NO}_x]$  and high rates of  $\text{NO}_2$  photolysis ( $J(\text{NO}_2)$ ), reactions of  $\text{NO}$  with  $\text{HO}_2$  can lead to increased  $[\text{OH}]$ , while under high  $[\text{NO}_x]$  reactions of  $\text{NO}_2$  with  $\text{OH}$  lead to  $\text{HNO}_3$  formation, and subsequent  $\text{OH}$  net loss (R5.1d and R5.1e).



The effect  $\text{NO}_x$  has on total  $\text{OH}$  and  $\text{HO}_2$  concentration will be relevant when discussing the effect  $\text{NO}_x$  on  $\text{HOM}$  formation from photooxidation in Chapter 5.

Dominant pathway of  $\alpha$ -pinene and  $\beta$ -pinene photooxidation is the  $\text{OH}$  attack at the double bond.  $\text{OH}$  adds to the double bond that opens whereby the  $\text{OH}$  radical is attached to one position of the double bond. The other end of the former double bond has alkyl radical character and by this  $\text{OH}$  addition a hydroxy substituted alkyl radical is formed. In analogy to reaction R1.3d a hydroxyl substituted peroxy radical is formed and the principles of further  $\text{RO}_2$  reactions are the same as those given above at the example of  $\text{H}$ -abstraction reactions.

As most of the published results with respect to HOM formation from  $\alpha$ -pinene were obtained from ozonolysis experiments, there are open scientific questions regarding OH induced HOM photochemistry. Therefore this work is focused on OH initiated HOM formation. The possible importance of sequential  $O_2$  addition (autoxidation) on the one hand and sequential OH oxidation on the other hand was studied, as well as whether ozonolysis is required to induce autoxidation (Chapter 3). OH dependency of HOM formation was studied in order to estimate the efficiency of HOM. Herein analysis of product distribution should give indication for the mechanism of HOM formation (Chapter 4). In the atmosphere nitrogen oxides ( $NO_x$ ) react with peroxy radicals and shift the product pattern to alkoxy radicals and organic nitrates. Besides  $NO_x$  the  $HO_2$  radical reacts fast with peroxy radical, on average the reaction of  $HO_2$  with  $RO_2$  is about a magnitude larger than the  $RO_2 - RO_2$  reactions. Both effects were investigated by looking at the changes of HOM abundance and HOM patterns after adding  $NO_x$  or carbon monoxide (CO) to the chemical system. This way also the assignment of HOMs to peroxy radicals and the respective termination products could be confirmed (Chapter 5). As many HOMs are also ELVOC, losses to surfaces are an important factor in the HOM concentration balance. The presence of particles led to substantial losses of HOM in competition to losses onto the wall, moreover the presence of particles affected the radical concentration and thus the HOM formation pathways (Chapter 6).

## 2. Methods and experimental set-up

### 2.1. Experiment set-up

#### 2.1.1. Jülich Plant Atmosphere Chamber

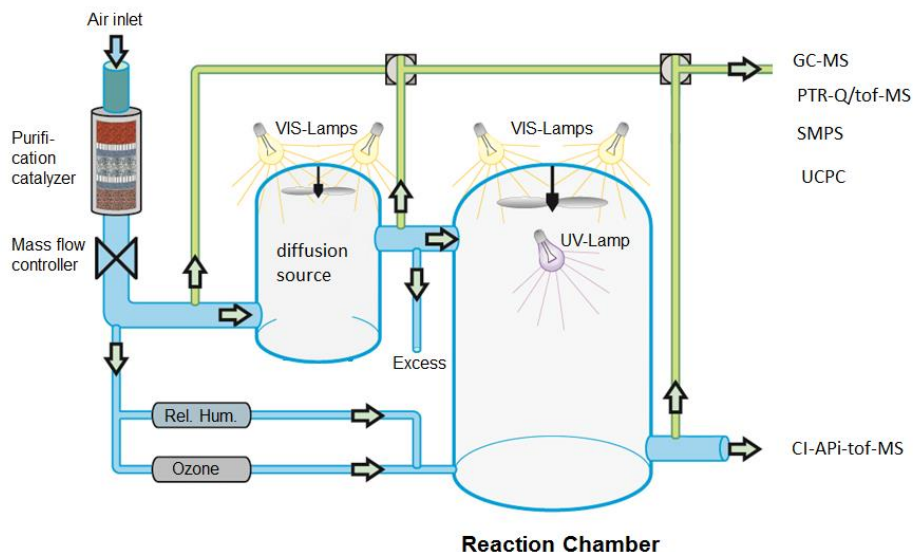


Figure 2.1 (Adapted from Mentel et al., 2009). Schematics of experiment chamber set-up. Purified air is divided into two separate inlet air flows, both which are humidified to similar degree to avoid problems at mixing the air masses in the chamber. To one of these flows the air from a diffusion source containing the wanted VOC was added. The use of different splits at the outlet of the diffusion source allowed varying BVOC concentrations in the chamber. The other flow is guided via an ozonator to introduce ozone into the chamber. The chamber is constantly stirred tank reactor (CSTR), with a mixing time of about 2 minutes. Residence time in the chamber during the experiments was about 45 minutes. The glass chamber is situated in a temperature controlled container. A host of instruments are used to measure the conditions in the chamber during the experiments. Most instruments can be switched to measure either inlet or outlet of the chamber, to gain data on changes, such as reacted VOC.

All the experiments were conducted at Jülich Plant Atmosphere Chamber (JPAC) shown in Figure 2.1. The chamber set-up is well explained by Mentel et al. (2009), but an overview will be given here. The reaction chamber used was a 1450 L Borosilicate glass chamber, and all the connecting tubes were made of either Teflon (PFA or PTFE) or glass. This was to minimize the potential wall losses during transport of gas and air into the analytical devices. The attached fan allowed constant stirring and well mixing of the air in the chamber, leading to a mixing times of about 2 minutes.

The chamber itself was located in a climate controlled container, which allowed temperature stability of  $\pm 0.5$  °C between 10 °C and 50 °C. In the experiments the temperature was set to 15 °C. The lamps in and around the chamber produced some heat, and during experiments the temperature varied between 15-16 °C.

There were two main inlet airflows into the chamber. Both main inlet flows were set between 10-16 LPM, depending on experiment. They were humidified by using double-distilled purified water vapour. One of them was then guided through an ozonator to add ozone in the chamber. To the other air flow, the desired VOC was added. When  $\text{NO}_x$  or CO was introduced into the chamber, the air containing  $\text{NO}_x$  or CO was mixed with this flow. Sometimes additional air flows were introduced, for example for seeding experiments when the aerosol seed was led to the chamber via separate inlet. This 2 LPM flow was not humidified, and the other two flows were usually adjusted slightly to compensate the additional dry air inflow to keep humidity constant in the chamber.

The seed particles were generated using a constant output aerosol generator (TSI, Model 3076) based on atomizing.  $(\text{NH}_4)_2\text{SO}_4$  solution (typical concentration  $\sim 40$  mg/L) was sprayed by a jet of compressed purified air passing through an orifice at a pressure of around 1.4 bar. The generated aerosol then passed through a silica gel diffusion drier and entered the reaction chamber. In the control experiments, distilled water was used for atomization to keep the experimental conditions constant.

Several lamps were used during the experiments. There were 12 discharge lamps (HQI 400 W/D; Osram), which were used to simulate the solar spectrum in the chamber. These are referred to as “top lamps”. There was one internal UVC lamp (Phillips, TUV 40W, with  $\lambda_{\text{max}} = 254$  nm) to photolyse ozone and to produce  $\text{O}^1\text{D}$ , which reacts with water vapour to produce OH. The UVC lamp was covered by adjustable glass tubing, which could be moved to vary the photolysis rate of  $\text{O}^1\text{D}$ , and thus OH production. For  $\text{NO}_2$  photolysis there were 12 discharge lamps (Phillips, TL 60, W/10-R, 60W,  $\lambda_{\text{max}} = 365$  nm). The glass of the chamber had a short wavelength cut-off close to 350 nm, which means no shortwave radiation could enter the chamber through the glass into the chamber to produce  $\text{O}^1\text{D}$  when UVC lamp was off. Additionally, the absorption cross section of  $\text{NO}_2$  at wavelength used by the UVC lamp is over one order of magnitude lower than at 356nm (Davidson et al., 1988). This allowed nearly independently varying  $J(\text{O}^1\text{D})$  and  $J(\text{NO}_2)$ .

The instrument suite did not include a direct OH measurement device, which means that determining OH concentration during the experiment must be achieved indirectly. The method used in the experiments was based on monitoring the concentration of reacting VOC, and its changes during the experiment. When the initial concentration of the VOC is known, the decrease of the VOC can be used to determine the amount of OH reacting with the VOC according to equation Eq.2.2.

$$\frac{d[\text{VOC}]}{dt} = \frac{F}{V} \cdot ([\text{VOC}_{\text{in}}] - [\text{VOC}]) - (k_{\text{OH}} \cdot [\text{OH}] \cdot [\text{VOC}] + k_{\text{O}_3} \cdot [\text{O}_3] \cdot [\text{VOC}]) \quad (\text{Eq.2.1.})$$

Assuming steady state conditions:  $\frac{d[\text{VOC}]}{dt} = 0$ , OH can be calculated using Eq.2.2:

$$[OH] = \frac{F \frac{[VOC]_{in} - [VOC]}{[VOC]} - k_{O_3} [O_3]}{k_{OH}} \quad (\text{Eq.2.2.})$$

Where  $[VOC]_{in}$  is the initial concentration of VOC in question,  $[VOC]$  is the concentration of the VOC in the chamber during experiment,  $F$  is total air flow through the chamber, and  $V$  is the volume of the chamber.  $k_{OH}$  and  $k_{O_3}$  are the rate coefficients of the VOC in question with OH and  $O_3$ , respectively.

Details of the experiments reported here are given in Chapter 2.3.

### 2.1.2. General instrumentation

Several instruments are used to measure the chamber experiment conditions. Ozone was measured by two UV photometric devices: Thermo Environment 49 and Ansynco, O3 42M ozone analyser. For NO measurements, chemiluminescence was used (Eco Physics, CLD 770). For  $NO_2$  measurements NO was measured after photolysis of  $NO_2$  (Eco Physics, PLC 760). In some cases an optimized chemiluminescence instrument with a blue light diode  $NO_2$  converter was used (Eco Physics 780 TR; Details in Li et al., 2014). Particle concentration was measured by CPC (TSI 3783, > 3nm) and particle size distribution (13-740nm) by SMPS (Waltz, TS-1 3081 electrostatic classifier combined with TSI 3025 CPC). To monitor humidity dew point mirrors were used at both inlet and outlet flows. VOC concentrations were measured by Proton Transfer Reaction – quadrupole- Mass Spectrometer (PTR-Q-MS, Ionicon), Proton Transfer Reaction – time-of-flight- Mass Spectrometer (PTR-TOF-MS, Ionicon), or Gas-Chromatography- Mass spectrometer (GC-MS, Agilent). All instruments could be switched from inlet to outlet, to follow the differences caused by reactions in the chamber.

The instrument used to detect HOM in the chamber was connected to a separate outlet, and could not be switched to inlet. More details on this instrument below.

## 2.2. Chemical ionization mass spectrometer

### 2.2.1. Instrument introduction

The instrument used to detect HOMs in the experiments is called Chemical Ionization Atmospheric Pressure interface time-of-flight Mass Spectrometer (CI-API-TOF-MS, from here on termed as “CIMS”). The CIMS can be divided into two main parts; to the mass spectrometer that is used to actually detect and measure HOMs (API-TOF-MS), and an inlet piece that can be attached to the mass spectrometer to enhance HOM detection by increasing HOM ionization (CI). First an overview on the API-TOF part of the instrument will be given, and then an introduction and some details about the ionization method and inlet used during the experiments. A short introduction on a calibration system set-up for CIMS will also be introduced.

The technical details of API-TOF-MS are described in Junninen et al. (2010). The instrument uses three staged pumping process to lower the sample pressure from atmospheric pressures to the range of  $10^{-6}$  mbar needed by the TOF (see Figure 2.2). Sample flow into the API-TOF-MS is determined by a critical orifice, which in the set-up is 300  $\mu\text{m}$  in diameter, allowing 800 mLPM sample flow. There is no ionization in API-TOF-MS (and it should not be confused with atmospheric pressure ionization, *API*). The API-TOF-MS was manufactured by Tofwerk AG, Thun, Switzerland and Aerodyne Research Inc., USA. The instrument has two modes that offer different mass resolving powers (R), V- and W-modes. The letter used depicts the path of ions in the TOF (time-of-flight) region, with W mode offering longer flight path and thus higher mass resolution. All results shown in this work were measured using the V mode. The resolving power achieved in the experiments ranged from 3000 to 4000 Th/Th, with accuracy higher than 20 ppm (0.002 %). Resolving power is defined as

$$R = M/\Delta M$$

Where M is mass/charge and  $\Delta M$  is the width of the peak at its half maximum. The mass range of the instrument was set to 4-1400 Th, which is more than enough for the purposes of this work. More than 95 % of the peaks observed in these studies were at masses below 700 Th.

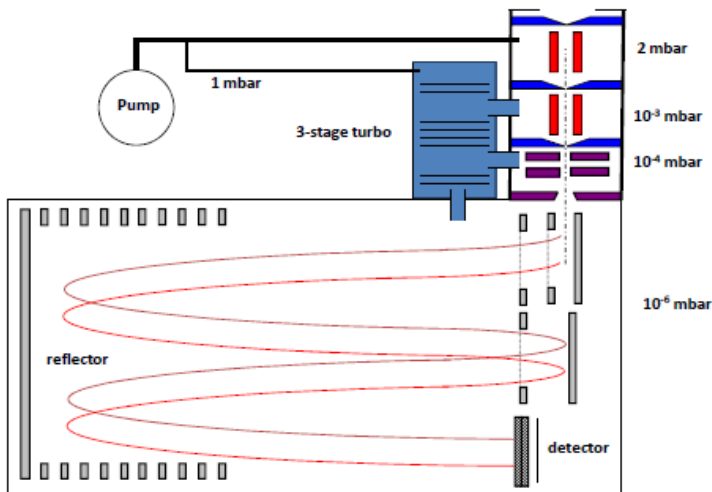


Figure 2.2 Schematic figure of API-TOF-MS (Junninen et al., 2010). There is no ionization method at this stage; ionization happens at an additional inlet configuration (Figure 2.3). Sampling is done at atmospheric pressure, after which the sample is focused and air is pumped out to reach low pressure ( $< 10^{-6}$  mbar) as used at the TOF region. Time-of-flight mass spectrometer (TOF-MS) is used to mass separate and detect ions. Normal operating mode of TOF-MS in the experiments was the V-mode, which gives somewhat lower mass resolution (3000-4000 Th/Th compared to c. 8000 Th/Th at W-mode), but has better sensitivity, and allows higher time resolution. In experiments shown here, only the V-mode was used. Critical orifice (300  $\mu\text{m}$ ) limits the sample flow into the API-TOF-MS system to approximately 800 mLPM.

The chosen ionization method used in the studies presented here was chemical ionization, which is a “soft” ionization method, and doesn’t cause fragmentation of the sample. The CI-inlet design has been described by Eisele and Tanner (1993), Kurtén et al. (2011), and Jokinen et al. (2012). It is specially designed to measure atmospheric sulphuric acid and its clusters, but can be used to modify API-TOF-MS into a specific measuring instrument for HOMs when run with nitric acid (nitrate,  $\text{NO}_3^-$ ) as reagent ion. Figure 2.3 shows a schematic cross view of the inlet design. Simplified, the inlet consists of  $\frac{3}{4}$  inch stainless steel sample line and a stainless steel reaction tube/drift tube. Nitric acid vapour is introduced into a 20 LPM sheath flow of pure air/purified, which is then exposed to  $\alpha$ -radiation from  $^{241}\text{Am}$  source to create nitrate ions. The sheath flow now containing the nitrate ions then flows into the reaction tube. An electric field in the outer wall of the reaction tube is used to guide the nitrate ions from the sheath flow into the sample flow, where they cluster with HOMs. The calculated interaction time between the ions and the sample gas is approximately 200 ms. The volume of the reaction tube/drift tube is  $\sim 240 \text{ mm}^3$ . With 10 LPM sample flow this gives a residence time of 1.5 ms.

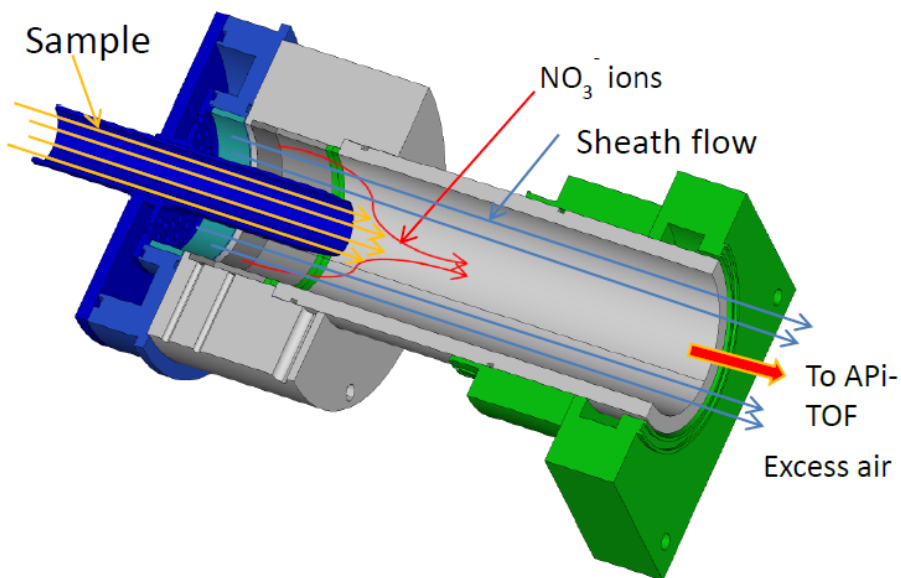
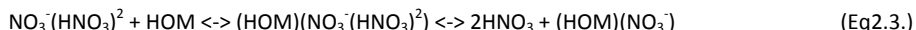


Figure 2.3 Schematic of  $\text{NO}_3^-$  CI-inlet. The inlet is attached directly in front of the critical orifice leading to the API-TOF part of the instrument, and is used to ionize the sample flow before it enters the mass spectrometer for detection. Nitric acid is introduced into the system via 20LPM sheath flow and ionized by alpha radiation from 10 MBq Americium-241 source. Electric field is then used to focus the nitrate ions in the reaction chamber into the sample flow, where they cluster with HOM (adapted from Jokinen, 2015).

The ionization in  $\text{NO}_3^-$  CIMS is done at atmospheric pressure, and it's based on clustering of the HOMs with the reagent ion ( $\text{NO}_3^-$ ), by collisions with nitrate ions (Eq2.1.), nitrate ion-nitric acid dimers (Eq2.2.) and nitrate ion-nitric acid trimers (Eq2.3.):



Eq2.1. leads directly to a formation of HOM- $\text{NO}_3^-$  cluster. The formation free energy of the cluster can be used to calculate the equilibrium constant and collision rate, which in turn determine the evaporation lifetime of the cluster (Hyytinen et al., 2015). Collisions with reagent ion dimer and trimer (Eq2.2. and Eq2.3.) lead to intermediate state clusters, from which either the HOM, or one or two  $\text{HNO}_3$  can be lost depending on the relative stabilities of the clusters.

Nitrate was chosen as a reagent ion since HOMs are known to readily cluster with it in ambient conditions (Ehn et al., 2012). Based on quantum chemical calculations, the HOMs are usually detected when they are able to form two hydrogen bonds with  $\text{NO}_3^-$ , which requires two OOH groups, or, hypothetically, another H donating group such as OH (Hyytinen et al., 2015). These structures allow the HOMs to form clusters with  $\text{NO}_3^-$  that are energetically more favourable than nitric acid dimer or trimer clusters. This means that higher oxidation state molecules cluster efficiently with the reagent ion and are detected, while low oxidation state compounds do not cluster with  $\text{NO}_3^-$  and are not detected. This means the results presented here might be biased towards highly oxidized end product spectrum. However, as the high O/C ratio is what makes HOMs interesting in particle formation and growth, the highly oxidized products were of main interest of this study.

In the experiments reported here, in addition to normal nitric acid ( $\text{H}^{14}\text{NO}_3$ ), isotopically labelled nitric acid ( $\text{H}^{15}\text{NO}_3$ , 98%  $^{15}\text{N}$ ) was used as a reagent ion compound. This was originally done to better distinguish in the mass spectra nitrogen from the reagent ion from nitrogen originating from  $\text{NO}_x$  addition into the HOM molecule. High resolution of the instrument allows differentiation, and could be used to show organic nitrate formation occurring during the experiments.

However, during very high  $\text{NO}_x$  concentration experiments, it was noticed that there was sufficient  $\text{HNO}_3$  formation happening in the chamber to compete with the labelled  $\text{HNO}_3$  in the instrument inlet. Figure 2.4 shows an example mass spectrum from the reagent ion monomer range ( $^{14}\text{NO}_3^-$  at 62 Th and  $^{15}\text{NO}_3^-$  at 63 Th) and dimer ( $\text{H}^{14}\text{NO}_3 \cdot ^{14}\text{NO}_3^-$  at 125 Th and  $\text{H}^{15}\text{NO}_3 \cdot ^{15}\text{NO}_3^-$  at 127 Th) during an experiment without  $\text{NO}_x$  addition, and when we had high  $\text{NO}_x$  addition (~80 ppb at the chamber inlet). A clear decrease in the proportion of labelled  $^{15}\text{NO}_3^-$  can be seen, and an increase in the unlabelled  $\text{NO}_3^-$ . In the case of the dimer cluster, the increase can be seen at one unit mass lower, with only one molecule of the cluster being from  $\text{H}^{14}\text{NO}_3$  (either  $^{14}\text{NO}_3^-$  or  $\text{H}^{14}\text{NO}_3$ ), and the other still from the labelled nitric acid from the inlet source. Same behaviour can be seen in the trimer nitrate peak as well (not shown).

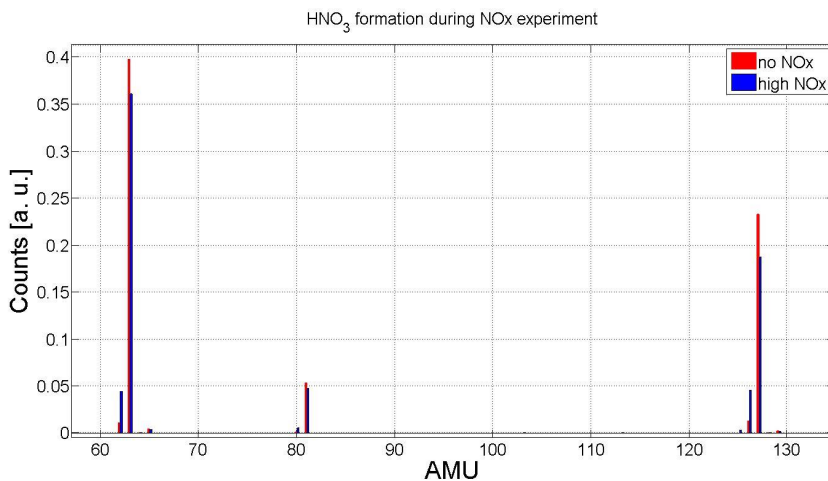


Figure 2.4 Comparison of reagent ion monomer and dimer regions between high  $\text{NO}_x$ -experiment with experiment of no added  $\text{NO}_x$ . The reagent ion used in the experiments was  $^{15}\text{NO}_3^-$ , which gives mean peaks at masses 63 Th (monomer) and 127 Th (dimer). During high  $\text{NO}_x$  experiments there was sufficient  $\text{H}^{14}\text{NO}_3$  formation taking place in the chamber for it to ionize in the inlet, and start competing with the labelled reagent ion. An increase on signal can be seen at 62 Th ( $^{14}\text{NO}_3^-$ ) and 126 Th (either  $\text{H}^{14}\text{NO}_3\text{-}^{15}\text{NO}_3^-$  or  $\text{H}^{15}\text{NO}_3\text{-}^{14}\text{NO}_3^-$ , cannot not be distinguished). The monomer peak at 63 Th decreased from 0.40 counts/s to 0.36 counts/s (a little under 10 % decrease), while the peak 62 Th increased by factor of four (0.011 counts/s to 0.045 counts/s). At reagent ion dimer the fully isotopically labelled cluster decreased by about 20 % (to 0.23 counts/s), while the mixed cluster increased from 0.014 counts/s to 0.046 counts/s (an increase of 240 %). Peak at 81 Th is water cluster ( $\text{H}_2\text{O}\text{-}^{15}\text{NO}_3^-$ ).

This mixing of unlabelled nitric acid from the chamber into the inlet in concentrations high enough to compete with the reagent ion caused some unforeseen complications. With a mixing ion clustering from  $^{14}\text{NO}_3^-$  and  $^{15}\text{NO}_3^-$ , reading the mass spectrum becomes complex, with a portion of all compounds being clustered with either ion. This problem only occurred with the highest concentration of  $\text{NO}_x$  used in this work, and was overcome by using total monomer and dimer concentrations in most analyses shown later. Compound analysis and identification was made with data sets obtained with low enough  $\text{NO}_x$  concentrations that this competing clustering did not happen, and when comparing total HOM formation, integrating over whole monomer or dimer range by-passed this issue. This applies to the  $\alpha$ -pinene +  $\text{NO}_x$  experiments shown in Chapter 5.

However, to prevent this from further confusing the results from later  $\text{NO}_x$  experiments,  $\text{H}^{14}\text{NO}_3$  was used in  $\beta$ -pinene +  $\text{NO}_x$  experiments. The advantage of distinguishing between reagent ion nitrate and reaction product nitrate was lost, but for peak identification one nitrogen atom was always assumed to come from  $\text{NO}_3^-$ .

In following chapters when showing results in a form of mass spectra, the mass from nitrate cluster will be subtracted, and the mass axes will all be the same, showing only the mass of the actual compound. This allows for easy comparison of the results obtained with different isotopic reagent ions, and showcases the mass of the actual reaction product, without additional mass from reagent ion clustering. In practice this means that a compound  $C_{10}H_{16}O_7$ , for example, will be shown at mass 248 Th instead of 310 Th ( $^{14}NO_3^-$  cluster) or 311 Th ( $^{15}NO_3^-$  cluster), and so forth.

## 2.2.2. Calibration

Calibrating the nitrate CIMS has been a challenge since the instrument was first modified to measure HOMs. The combination of low vapour pressures of the compounds of interest, and the very sensitive instrumentation, has proven finding a calibration set-up and suitable calibration compound to be difficult.

In the calibration set-up, there was a temperature controlled diffusion source, with two stage dilution to reach the low ppt levels required by the instrument, while at the same time achieving high enough evaporation loss from the source to calculate reliably the concentration given by the source. The lines leading from the calibration source into the instrument were heated at  $\sim 50^\circ C$  to prevent condensation of the calibration compound into the lines.

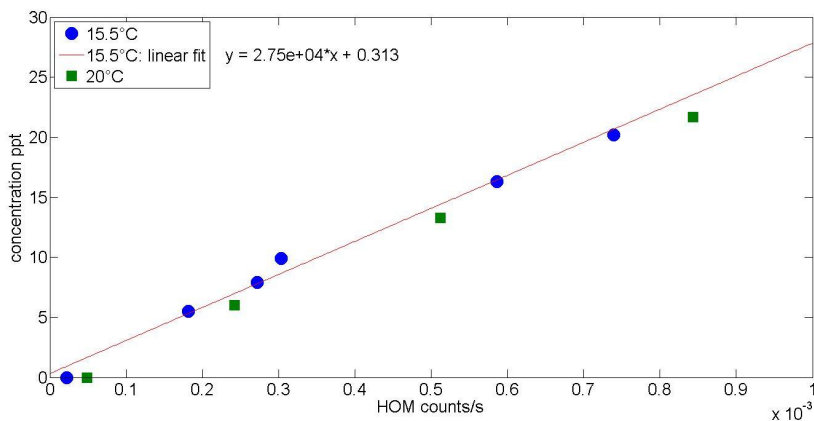


Figure 2.5 Calibration at two separate temperatures.  $15.5^\circ C$  is within the normal operating temperature of the experiments;  $20^\circ C$  was chosen as an example of higher summer time ambient temperatures. Higher temperatures were not possible as the instrument itself was situated in the temperature housing, and higher temperatures may cause mechanistic changes inside the instrument. Using linear regression a concentration calibration equation for HOM was acquired.  $R^2$  for the linear fit was 0.99.

Figure 2.5 shows results from the calibration experiment in two different temperatures, using perfluorooctanoic acid ( $C_8HF_{15}O_2$ ) as a calibration compound. The main peak given by the compound is given at mass 476 Th (as a cluster with  $^{14}NO_3^-$ ; mass without reagent ion 414 Th). This is at the upper limit of the HOM monomer range that is the focus of the results here. The calibration method is still limited by only giving calibration for one mass, and not the whole mass range, so linearity over mass range must be assumed. Both temperatures give very consistent calibration results, with a linear dependence over entire range of concentrations.

Calibration factor  $C_x$  can be calculated using method described by Ehn et al. (2014, supplements):

$$[X] = C_x \cdot \sum_{i=0}^2 [(HNO_3)_i(NO_3^-)(X) + (HNO_3)_i(X-H)^-] / \sum_{i=0}^2 (HNO_3)_i(NO_3^-) \equiv C_x \cdot A$$

Here X is the concentration of the neutral calibration compound that was measured, the numerator consists of the sum of all detected ion clusters containing the calibration compound X, and the denominator is the sum of all reagent ions. A is the ratio that can be determined from calibration measurements. Solving for  $C_x$  gives the calibration factor which can then be used to calculate HOM concentrations.

Previously it was mentioned that linearity over the mass range is assumed when applying the calibration factor due to only having one m/z point to use. According to a study concerning the transmission times in a CIMS, the sensitivity might not be linear over the m/z (Heinritzi et al., 2016). The authors describe how using different fluorinated compounds they charted the transmission over the m/z range used to detect HOMs, and concluded that in their set-up the transmission of average dimer range molecule might be up to twice as strong as that of monomer range molecule. However, the behaviour of charged clusters in the instrument is highly dependent on the tuning of the instrument, and thus the results cannot be directly applied to measurements reported in this work. Yet, the results presented by Heinritzi et al. are a good reminder that linear approach will potentially include large errors when applied to masses far smaller or larger than the mass of the calibration compound we used. In the future it is planned to include a range of different calibration compounds to achieve more accurate calibration over larger m/z range in the CIMS.

When using the calibration measurements made with the set-up, a calibration factor  $C_x$  was calculated to be in  $5 \cdot 10^{11}$ . This is an order of magnitude higher than what has been reported in literature for CIMS (Jokinen et al., 2012; Ehn et al., 2014). It is possible that the CIMS used here, which is one of the older models in use, has much lower sensitivity. It is also possible that there are some errors introduced from weighing the calibration compound (to calculate the mass loss over time to derive the concentration), or that despite heating the calibration set-up tubing there might have been some condensational losses between the calibration source and the instrument. The error of actual concentration calculations is thus in the order of one magnitude.

In this work the concentration will be on the photochemistry side of the HOM formation, and as the goal of this work is to present qualitative and not quantitative results, the actual concentrations are not

crucial. For this reason the results in this work will be given as counts/s, although an example of absolute HOM concentrations will be given in Chapter 4.

### 2.3. Experiment protocols

Several experiments were conducted in the study of photochemical HOM formation. Here an overview on the made experiments is given, as well as the motivation behind each experiment.

Figure 2.6 shows an example experiment of HOM production from OH oxidation. The chamber was run until the system reaches a steady state at ozone regime, then the UVC lamp was turned on to initiate OH production. A typical behaviour of HOM formation was a rapid increase when OH production began, followed by slower decrease into steady state. After a new steady state under OH HOM production was reached, the UVC lamp was turned off and the experiment finished. Figure 2.7 shows an example from NO<sub>x</sub> addition experiment. The difference of NO<sub>x</sub> experiment is that before starting OH production, NO<sub>x</sub> is introduced in the chamber and then waited to reach steady state before initiating OH production. The ending of the experiment varied according to the purpose, with sometimes NO<sub>x</sub> addition stopped before OH production, or vice versa. The two examples for the procedures of experiments are representative, although in individual experiments the procedure might deviate from this pattern depending on the objective of the experiment.

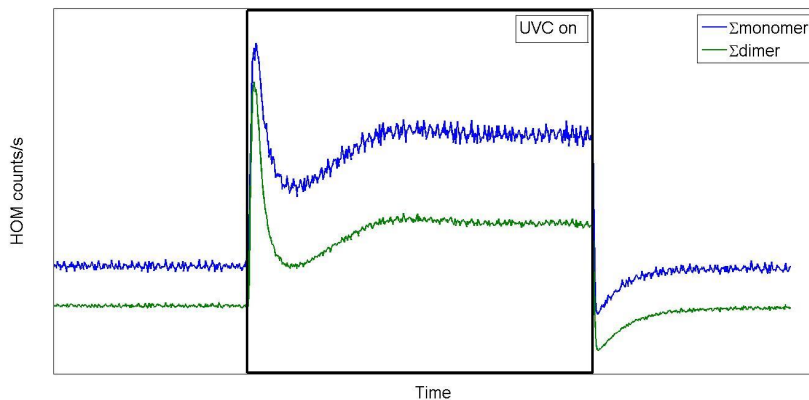


Figure 2.6 Example of experiment run without NO<sub>x</sub>. After chamber has reached steady state under ozone, UVC lamp is turned on to start OH production. Experiment is continued until chamber has reached (pseudo) steady state under OH regime, then UVC lamp is turned off, and experiment ended. Example shown here is with  $\alpha$ -pinene HOM production. Time scale is in hours.

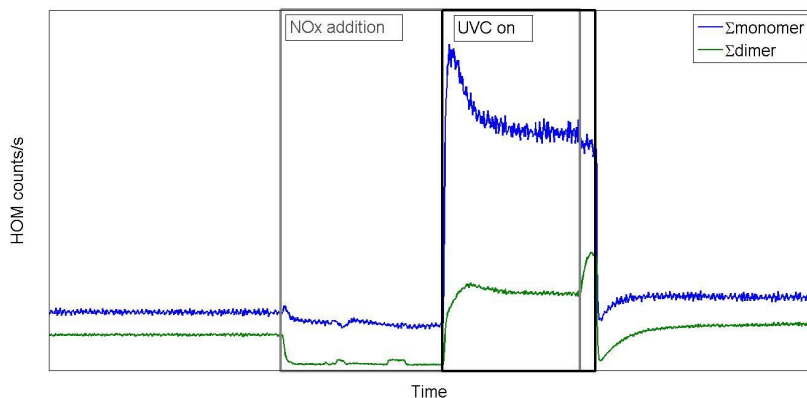


Figure 2.7 Example of  $\text{NO}_x$  dependence experiment run. After  $\text{NO}_x$  addition is started, steady state is waited before starting OH production by switching on UVC lamp. UVA lamp is on during  $\text{NO}_x$  addition to photolyse  $\text{NO}_2$  into NO. Ending of a  $\text{NO}_x$  experiment varied, either first stopping  $\text{NO}_x$  addition, or OH production, depending on the goal of the experiment. Time scale is in hours.

When discussing results in later chapters, a notation introduced by Mentel et al. (2015) is sometimes used. Peroxy radical with a certain molar mass is referred to as  $m$ , hydroperoxide as  $m+1$ , ketone as  $m-17$  and organic nitrate as  $m+30$ . Additionally a notation  $m+46$  to refer to PAN-like nitrates is used. Numbers used are based on the mass differences of the termination products of the peroxy radical.

Reaction rates used for the calculations as well as peak lists for  $\alpha$ -pinene,  $\beta$ -pinene, and cyclohexene can be found in Appendix. Example mass spectra for photochemical HOM formation from  $\alpha$ -pinene with and without  $\text{NO}_x$  can also be found in the Appendix.

### 2.3.1. Experiment overview

The mechanistic side of photochemical HOM formation will be presented in Chapter 3. The purpose was to investigate if the same basic autoxidation mechanism reported to be responsible for ozonolysis HOM formation is behind photochemical HOM formation as well, or whether OH attacks the molecule several times is a sequential oxidation. To better study this, the effects of these two mechanisms needed to be separated.

To start, photochemical HOM formation from cyclohexene and cyclohexene-d10 is compared. In molecules where hydrogen is replaced by deuterium the H-shift is inhibited, suppressing autoxidation (Kurtén et al., 2015). Tables 2.1. and 2.2. give the initial experimental conditions of these experiments,

i.e. the VOC input concentration before any reactions have happened in the chamber. The given [OH] is the actual OH concentration during experiment.

Table 2.1. Initial experiment conditions for cyclohexene experiment. Concentrations are calculated concentrations in the chamber before any reactions have taken place.

Experiment set	OH <sup>a</sup>
[cyclohexene]	26 ppb
[ozone]	54 ppb
[OH] cm <sup>-3</sup>	1.0 · 10 <sup>7</sup> cm <sup>-3</sup>
RH	60 %
particle surface	-
temperature	15 °C

<sup>a</sup>: simple test of initiating OH production in the chamber and observing formed HOMs.

Table 2.2. Initial experiment conditions for deuterated cyclohexene (cyclohexene-d10) experiment. Concentrations are calculated concentrations in the chamber before any reactions have taken place.

Experiment set	OH <sup>a</sup>
[cyclohexene-d10]	95 ppb
[ozone]	54 ppb
[OH] cm <sup>-3</sup>	-
RH	60 %
particle surface	-
temperature	15 °C

<sup>a</sup>: simple test of initiating OH production in the chamber and observing formed HOMs.

In order to investigate the  $\alpha$ -pinene photochemical HOM formation the photochemical reaction system was varied by changing the OH source strength (e.g. J(O<sup>1</sup>D)). The OH experiments served also to compare the formation rates of HOM molecules with different number of oxygen atoms as this is indicative whether they are formed instantaneously (autoxidation) or by sequential oxidation. In same sense it is compared whether the gross pattern of end products is changing with changing [OH]. The initial conditions of OH experiments of  $\alpha$ -pinene can be seen in Table 2.3., column one.

On top of this an oxygen replacement experiment was performed with the idea to inhibit RO<sub>2</sub> formation, thus inhibiting the autoxidation process (compare Jokinen et al., 2014; Berndt et al., 2015). The experiment was conducted by replacing the oxygen in the air flow leading into the chamber by nitrogen. The goal was to reach oxygen concentrations <1 %. During this experiment both photochemical HOM formation and ozonolysis initiated HOM formation was tested.

As pure OH chemistry is an unlikely occurrence in the real atmosphere, next objective was to study the effect of NO<sub>x</sub> addition on HOM formation. The NO<sub>x</sub> concentrations used in this study are given in the

second column of Table 2.3. In addition, CO was added to system in order to study the response of increasing HO<sub>2</sub> (Table 2.3. column 3). Results obtained from these experiments will be covered in Chapter 5.

For chemical mass balance of HOMs it is important to consider the gas-phase loss processes, i.e. condensation on particles due to their low vapour pressures. The particle concentration was regulated by changing the HOM precursor concentrations to change the rate of nucleation, or by introducing seed particles from a particle generator (see Chapter 2.1.1.). Details of these experiments are given in column four of Table 2.3, and will be discussed in Chapter 6.

Table 2.3. Initial experiment conditions for  $\alpha$ -pinene experiments. If several values were used during the experimentation (for example in OH dependency experiment), the total range is given. Concentrations are concentrations in the chamber before any reactions have taken place ([OH] during experiments). Variations of [OH] were obtained by variations of J(O<sup>1</sup>D), variations of [NO<sub>x</sub>] and [CO] were obtained by varying the inflow of the respective trace gas and variation of surface was obtained by changing the inflow of ammonium sulfate particles.

Experiment set	f(OH) <sup>a</sup>	f(NO <sub>x</sub> ) <sup>b</sup>	f(CO) <sup>c</sup>	f(surface) <sup>d</sup>
[ $\alpha$ -pinene]	9.9 ppb	18 ppb	12 ppb	11 ppb
[ozone]	32 ppb	30 – 38 ppb	45 ppb	47 ppb
[OH]	0.5 · 10 <sup>6</sup> – 5 · 10 <sup>7</sup> cm <sup>-3</sup>	2.8 – 7.6 · 10 <sup>7</sup> cm <sup>-3</sup>	2.6 · 10 <sup>6</sup> – 4.3 · 10 <sup>7</sup> cm <sup>-3</sup>	0.5 – 9.4 · 10 <sup>7</sup> cm <sup>-3</sup>
RH	60 %	60 %	60 %	60 %
[NO <sub>x</sub> ]	-	0.5– 121 ppb	-	-
[CO]	-	-	0 – 57 ppm	-
particle surface	-	0 - 6 · 10 <sup>-5</sup> m <sup>2</sup> m <sup>-3</sup>	7.2 · 10 <sup>-5</sup> m <sup>2</sup> m <sup>-3</sup>	0 – 1 · 10 <sup>-3</sup> m <sup>2</sup> m <sup>-3</sup>
temperature	15 °C	15 °C	15 °C	15 °C

<sup>a</sup>: f(OH) = variations of [OH] by changing J(O<sup>1</sup>D).

<sup>b</sup>: f(NO<sub>x</sub>) = variations of [NO<sub>x</sub>].

<sup>c</sup>: f(CO) = variation of [CO].

<sup>d</sup>: f(surface) = variation of particle surface.

Table 2.4. Initial experiment conditions for pinonaldehyde experiment. Concentrations are calculated concentrations in the chamber before any reactions have taken place. Pinonaldehyde could not be measured with the PTR-Q, and thus [OH] and [pinonaldehyde] data are not available. Experiment results will be only qualitative.

Experiment set	OH <sup>a</sup>
[pinonaldehyde]	several ppb
[ozone]	190 ppb
[OH] cm <sup>-3</sup>	-
RH	60 %
particle surface	-
temperature	15 °C

<sup>a</sup>: simple test of initiating OH production in the chamber and observing formed HOMs.

The potential role of secondary OH oxidation as a HOM formation pathway was studied by using pinonaldehyde as a precursor (Table 2.4.). Pinonaldehyde is the main atmospheric primary oxidation product by OH of  $\alpha$ -pinene (Peeters et al., 2001; Capouet et al., 2004).

One goal of this work was to study the HOM formation from compounds with different molecular structures.  $\beta$ -pinene was used as an example of a compound with an exocyclic double bond, opposed to endocyclic double bond in  $\alpha$ -pinene.  $\beta$ -pinene results from OH dependency experiment (Table 2.5. column one) and the experiments with  $\text{NO}_x$  (Table 2.5, column two) were used to support the analyses in the respective chapters (Chapters 3, 4, and 5).

Table 2.5. Initial experiment conditions for  $\beta$ -pinene experiments. If experiment set consist of several values, a total range is given. Concentrations are calculated concentrations in the chamber before any reactions have taken place. Variations of [OH] were obtained by variations of  $J(\text{O}^1\text{D})$ , variations of  $[\text{NO}_x]$  by varying the inflow of  $\text{NO}_x$ .

Experiment set	f(OH) <sup>a</sup>	f( $\text{NO}_x$ ) <sup>b</sup>
[ $\beta$ -pinene]	0.9 ppb	13 ppb
[ozone]	54 ppb	54 ppb
[OH] $\text{cm}^{-3}$	0.5 – $6 \cdot 10^7 \text{ cm}^{-3}$	4.6 – $4.9 \cdot 10^7 \text{ cm}^{-3}$
RH	60 %	60 %
[ $\text{NO}_x$ ]	-	4.9 ppb
[CO]	-	-
particle surface	-	-
temperature	15 °C	15 °C

<sup>a</sup>: f(OH) = variations of [OH] by changing  $J(\text{O}^1\text{D})$ .

<sup>b</sup>: f( $\text{NO}_x$ ) = variations of  $[\text{NO}_x]$ .

HOM formation from two benzenoid compounds was also studied. Methyl salicylate (MeSA) was chosen as an example of a biogenic emission and benzene as an example of an anthropogenic emission. Benzenoid compounds do not react with ozone, and thus HOM formation from these compounds would originate from photooxidation, excluding the possibility of reaction with ozone being required as a first step in photochemical HOM formation. Tables 2.6. to 2.7. show experiment conditions for these compounds.

Table 2.6. Initial experiment conditions for benzene experiment.

Experiment set	OH <sup>a</sup>
[benzene]	12.5 ppb
[ozone]	65 ppb
[OH] $\text{cm}^{-3}$	$2.7 \cdot 10^8 \text{ cm}^{-3}$
RH	60 %
particle surface	-
temperature	15 °C

<sup>a</sup>: simple test of initiating OH production in the chamber and observing formed HOMs.

Table 2.7. Initial experiment conditions for methyl salicylate experiment. [MeSA] and [OH] were data not available.

Experiment set	OH <sup>a</sup>
[methyl salicylate]	-
[ozone]	105 ppb
[OH] cm <sup>-3</sup>	-
RH	60 %
particle surface	-
temperature	15 °C

<sup>a</sup>: simple test of initiating OH production in the chamber and observing formed HOMs.

## Chapter 3 Photochemical HOM formation mechanism: Sequential oxidation versus autoxidation

### 3.1. HOM formation and autoxidation: setting the problem

In systematic studies of HOM formation via ozonolysis the autoxidation has been shown to be a major mechanism behind the HOM formation (Mentel et al., 2015; Jokinen et al., 2014). Ozone attacks the C=C bond in the precursor, creating Criegee intermediate. One reaction pathway of Criegee radical is to form vinylperoxide, which decomposes to a peroxy radical with an aldehyde-functionality (Mentel et al., 2015). The peroxy radical then undergoes internal H-shift, with further O<sub>2</sub> addition into the molecule (see Introduction 1.2. for details).

As an additional test to ozone HOM formation, the effect of endocyclic versus exocyclic double bond in HOM formation was tested, using  $\beta$ -pinene as an example. While  $\alpha$ -pinene has endocyclic double bond, enabling ozone to initiate HOM formation,  $\beta$ -pinene has an exocyclic double bond i.e. outside of the ring. With an endocyclic ring, the breakup of the primary ozonide forms two ends with functional groups but the molecule itself is not fragmenting. This allows intramolecular H-shift. With an exocyclic ring the breakup of primary ozonide also breaks the molecule. There is a peroxy radical at one of the fragments, but the fragment with the complementary group is at the other fraction. Hence, intramolecular H-shift is hindered as there is no aldehyde functionality in the peroxy radical. It was therefore expected that the efficiency of HOM formation from ozonolysis of  $\beta$ -pinene is much lower than from  $\alpha$ -pinene. Indeed, under used test conditions  $\beta$ -pinene can be considered not to produce HOM under ozonolysis. This is consistent with the conclusions given in Mentel et al. (2015) that aldehyde groups strongly promote HOM formation. Taking all evidence from the studies presented here and those presented in the literature, the HOM formation mechanism seems to be clear for ozonolysis. Moreover, ozonolysis requires formation of intermediate with a functional group, as only internal H-shift may carry on further oxidation and HOM formation. From these it can be concluded that HOM formation through ozone oxidation is likely driven by internal H-shifts in peroxy radicals and subsequent O<sub>2</sub> addition. This process is termed autoxidation. Detailed descriptions of suggested pathways can be found in Jokinen et al. (2014), Mentel et al. (2015), Kurtén et al. (2015), Rissanen et al. (2015), Berndt et al. (2015), and Jørgensen et al. (2016).

In cases of VOC with only one double bond (i.e.  $\alpha$ -pinene), ozone is only able to react once with the VOC, and there can be no further ozonolysis of the subsequent oxidation products. This means sequential reactions with ozone are not a possibility in (HOM formation via) ozonolysis. In contrast, since an oxidant OH is not as selective as O<sub>3</sub>, it can react with  $\alpha$ -pinene and subsequent oxidation products several times by sequential H-abstraction. Each H-abstraction step would generate a new peroxy radical which would then terminate in the usual way (see Introduction 1.3.). Thus, it needs to be ascertained whether HOM formation during photooxidation is mainly driven by autoxidation as in the case of ozone, or if sequential oxidation by OH is the more efficient mechanism.

In this chapter the focus is on the mechanism behind the HOM formation through photooxidation, and look at results from experiments relevant to the mechanistic side of it. The examples used here are cyclohexene and deuterated cyclohexene as a simpler model system for  $\alpha$ -pinene, and  $\alpha$ -pinene as an atmospherically relevant VOC.  $\beta$ -pinene, MeSA, and benzene are used as (further) examples of volatile compounds which do not react with ozone but produce HOM under photooxidation.

### 3.2. Cyclohexene versus cyclohexene-d10

To understand the formation of HOM from photooxidation, it is important to understand whether the HOM formation happens by autoxidation or if sequential OH oxidation is the main mechanism, or whether it is both. The effect of these two mechanisms must be separated to study which is dominant. There are few ways to achieve this.

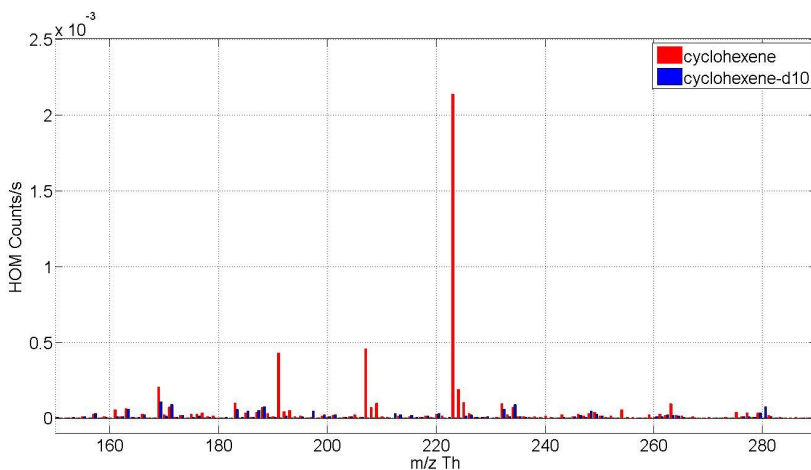


Figure 3.1 Comparison between cyclohexene HOM production and deuterated-cyclohexene HOM production under OH, monomer range. [OH] in cyclohexene experiment  $\sim 1.0 \cdot 10^7 \text{ cm}^{-3}$ , [cyclohexene]  $\sim 13 \text{ ppb}$ . [Cyclohexene-d10]  $\sim 80 \text{ ppb}$ ,  $\sim 30\%$  consumed by OH. Cyclohexene (red) shows a clear pattern of HOM with different number of oxygen atoms, while cyclohexene-d10 (blue) has only few small peaks, without clear pattern. Large cyclohexene peaks at 192 Th, 208 Th, and 224 Th correspond to C<sub>6</sub>H<sub>7</sub>O<sub>7.9</sub>, respectively. This is the projected hydroperoxide (Introduction, R1.3e) corresponding peroxy radicals C<sub>6</sub>H<sub>7</sub>O<sub>7.9</sub>, respectively.

Figure 3.1 shows results of experiments done with deuterated cyclohexene. The compound chosen for this experiment was cyclohexene ( $C_6H_{10}$ ), which forms HOM under OH oxidation (red). The second part of the experiment was done with fully deuterated cyclohexene ( $C_6D_{10}$ , cyclohexene- d10), to see if and how HOM formation is affected (blue). As rate coefficients for cyclohexene-d10 were not found, [OH] is only provided for cyclohexene experiment ( $\sim 1.0 \cdot 10^7 \text{ cm}^{-3}$ ). In cyclohexene case 60 % of the cyclohexene reacted during the experiment, while in the case of cyclohexene-d10 the rate is lower, 30 %. However, it is sufficient to show the cyclohexene-d10 was reacting. Cyclohexene shows clear HOM formation, with few prominent peaks that could be identified, namely  $C_6H_8O_7$  at 192 Th,  $C_6H_8O_8$  at 208 Th, and  $C_6H_8O_9$  at 224 Th. In cyclohexene-d10 spectrum there is no clear evidence of HOM formation, and only few small peaks are present. It is clear that in case of cyclohexene at least deuteration inhibits HOM formation.

Based on quantum chemical calculations Kurtén et al. (2015) show that tunnelling is involved in the rearrangement step of the autoxidation. As a consequence H-shifts are inhibited in molecules when hydrogen is replaced by deuterium. Use of D-substituted molecules provides thus a way to test the importance of the sequential oxidation pathway of HOM formation by suppressing or inhibiting the occurrence of autoxidation. Significant HOM formation from fully deuterated molecules would be an indication that sequential oxidation cannot be excluded as a HOM formation mechanism. However, if HOM formation would be stunted, it would suggest autoxidation to be the major mechanism driving photooxidation HOM formation. From results shown in Figure 3.1 it can be concluded that there was no significant HOM formation from deuterated cyclohexene.

This finding suggests that autoxidation is an important step also in photooxidation. However, this does not exclude the possibility of sequential oxidation, with primary oxidation products further reacting with OH, and forming HOM. Additionally, it must be mentioned that due to kinetic isotope effect of D, the sequential reactions of  $C_6D_{10}$  with OH will also be suppressed by a factor of 2-3. But, at least in case of cyclohexene photooxidation, sequential reactions with OH seem to be of minor importance compared to autoxidation. More of this will be discussed in Chapter 3.3.2.

### 3.3. Monoterpenes: $\alpha$ -pinene

#### 3.3.1. Photochemical HOM formation from $\alpha$ -pinene

Cyclohexene is a simple system containing an endocyclic double bond allowing insights into basic mechanisms, but for atmospheric relevance  $\alpha$ -pinene is the more important compound. As one of the most abundant monoterpenes emitted, it is a prominent SOA precursor especially in boreal regions (Guenther et al., 2012).

To begin, a look into  $\alpha$ -pinene photochemical HOM formation under different OH concentrations is given, and then data from those experiments is used to further elucidate the mechanism behind the

photochemical HOM formation. The OH dependence of HOM formation will be further covered in Chapter 4.

First it needs to be established that HOM formation from  $\alpha$ -pinene observed in the presence of OH is due to photooxidation and not to ozonolysis alone. Figure 3.2 shows  $\alpha$ -pinene HOM pattern under ozone (blue) and OH (red) oxidation. In the ozonolysis HOM it can be clearly seen how the patterns in the clusters repeat a 32 Th progression, which is in accordance with the hypothesis of H-shifts in peroxy radicals and subsequent addition of O<sub>2</sub>.

In case of photooxidation there seems to be a pattern repeating every 16 Th, with each cluster shown exhibiting similar pattern. There are two possible options. Either there is a progression of 16 Th as directly suggested by the data, or there are two progressions of 32 Th, each 16 Th (mass of one oxygen atom) apart.

The progression of 16 Th might hint to the importance of pinonaldehyde ( $\alpha$ -pinene oxidation product, see Chapter 3.3.2.) as an intermediate, but the role of other sequential OH reactions cannot be excluded here.

The first  $\alpha$ -pinene peroxy radical to form via photooxidation has three oxygen atoms (compared to four in ozonolysis). From this it could be expected that in the case of OH formed peroxy radical HOM formation would be shifted by 16 Th compared to ozonolysis case, which is what is observed. This would account for the 16 Th-shifted progression of 32 Th seen in photooxidation HOM spectra that is absent in ozonolysis spectra, but this does not explain the assumed second progression (overlapping ozonolysis pattern). However, if there would be another, an analogous rearrangement of alkoxy radicals, (alkoxy-peroxy pathway) it would produce peroxy radicals with alcohol groups i.e. with only one oxygen atom more than the previous form (see Mentel et al. (2015) for details of the mechanism). This combination of peroxy radical pathways would lead to observed HOM pattern, but at the moment it is not possible to positively determine whether this is the actual formation mechanism, as the alkoxy-peroxy pathway can also explain direct progressions of 16 Th.

Regardless, this is a hint that the alkoxy-peroxy pathway may be more important in photochemical HOM formation than in ozonolysis based.

Additional to the change in pattern density, another difference between the HOM pattern found during ozonolysis and photooxidation is in the end product intensity distribution. In ozonolysis ketones are the main closed shell end product at monomer range (Mentel et al., 2015). With photooxidation, and subsequent increased HO<sub>2</sub> concentration in the system, hydroperoxides become the dominant monomer range end product group, as RO<sub>2</sub> + HO<sub>2</sub> reaction (R1.3e) begins to compete with the RO<sub>2</sub> · RO<sub>2</sub> (R1.3f) pathway. This can be seen as increased signal intensities at peaks 248 Th and 264 Th for example.

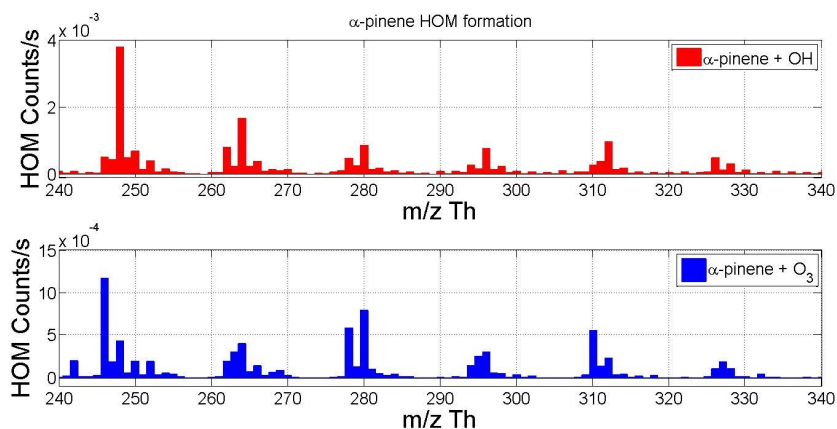


Figure 3.2  $\alpha$ -pinene HOM formation with OH, and ozonolysis at monomer range. In the upper panel it can be seen that under photooxidation there are distinct clusters of HOM at 16 Th apart, while in ozonolysis case the clusters appear ever 32 Th apart. As OH was not quenched during ozonolysis experiment, some OH was present from VOC ozonolysis. For photooxidation: [OH]  $4.6 \cdot 10^7 \text{ cm}^{-3}$ . [ $\alpha$ -pinene] 1.5 ppb; total monomer 0.69 counts/s, total dimer 0.44 counts/s. Ozonolysis: [ $\alpha$ -pinene] 7.5 ppb, total monomer 0.58 counts/s, total dimer 0.33 counts/s. Note the difference in Y-axes.

From the cyclohexene study it is obvious that, at least with some VOC species, HOM formation is driven by autoxidation also during photooxidation. There are some published studies that describe HOM formation from  $\alpha$ -pinene photooxidation (Ehn et al., 2014; Jokinen et al., 2014), and they all conclude  $\alpha$ -pinene is able to produce HOM with OH as well as ozone, albeit in different efficiencies.

So far it has been established that  $\alpha$ -pinene forms HOM with photooxidation, and that the pattern of produced HOM has similarities with the HOM pattern from ozonolysis, which runs via peroxy radical autoxidation. The cyclohexene and cyclohexene-d10 experiment give a clear hint towards autoxidation being the main mechanism behind photochemical HOM formation, at least in the case of cyclohexene.

### 3.3.2. HOM formation from secondary OH oxidation: pinonaldehyde

In atmospheric conditions, the main primary oxidation product of  $\alpha$ -pinene is pinonaldehyde (Peeters et al., 2001; Capouet et al., 2004). To gain further understanding of the formation pathway of photochemical  $\alpha$ -pinene HOM formation, the HOM formation from pinonaldehyde via OH oxidation was tested. For an oxidation product to be relevant in HOM formation, it needs to be produced in high concentration, and be highly reactive. With pinonaldehyde both requirements are met. Additionally, it

has potential for rearrangement, and has an abstractable H-atom, all of which are prerequisites for autoxidation to occur.

Figure 3.3 shows the comparison between  $\alpha$ -pinene and pinonaldehyde HOM spectra, and as can be seen, apart from the signal intensities, the patterns are very similar. This would suggest that at least a part of the photochemical HOM formation from  $\alpha$ -pinene could happen through pinonaldehyde as intermediate. This pathway would require two oxidation steps with OH, first to form the pinonaldehyde, and then another to oxidize the pinonaldehyde to start HOM formation. Note that two step sequential oxidation of main oxidation products is likely to contribute to photochemical HOM formation. It is here not possible to determine if the entire  $\alpha$ -pinene photochemical HOM formation goes by pinonaldehyde channel.

From pinonaldehyde HOM it can also be deduced that a double bond is not a requirement for HOM formation, which is understandable as OH is non-selective oxidant and can attack several different sites. As long as required functionality can be achieved HOM formation can occur.

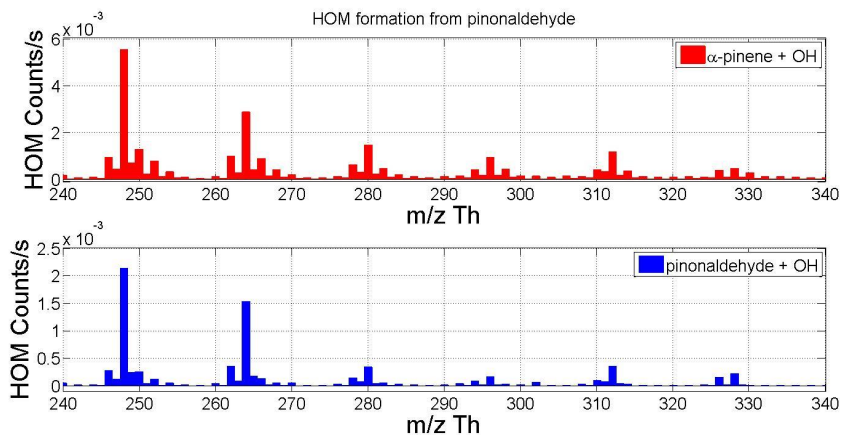


Figure 3.3 Comparison spectra of HOM formation from  $\alpha$ -pinene and pinonaldehyde photooxidation. The pattern is nearly identical, only noticeable difference is in the peak intensities. This is a good indication that a part of  $\alpha$ -pinene HOM formation with OH could go via pinonaldehyde, its main primary OH oxidation product. OH,  $\alpha$ -pinene, and pinonaldehyde concentrations are not comparable, so this result is qualitative, not quantitative. Note the difference in Y-axes.

### 3.4. HOM formation rate comparison

If HOM formation from OH oxidation would go via sequential oxidation, it could be assumed that the formation rate of molecules with different oxidation states (six oxygens vs ten oxygens, for example) would be different, with higher oxidation state compounds forming slower.

Figure 3.4 shows a comparison between the formation rates of  $C_{10}H_{16}O_6$ ,  $C_{10}H_{16}O_7$ , and  $C_{10}H_{16}O_{12}$ , all closed shell end products (hydroperoxides) of  $\alpha$ -pinene OH oxidation. Due to its low number of O atoms,  $C_{10}H_{16}O_6$  is one of the first HOMs that can be observed with the CIMS, although still very inefficiently. The efficiency of its detection is low, meaning that what is seen is only a small portion of the actual concentration, but the changes observed in signal intensities are likely to be proportional to actual changes in concentration of the compound. In contrast,  $C_{10}H_{16}O_{12}$  is a hydroperoxide with one of the highest number of oxygen that can be detected reliably. The peak intensity is quite low, which adds scatter in the data, but it can still be seen that the formation rates are very similar. To rule out coincidence with two particular products,  $C_{10}H_{16}O_7$ , one of the most prominent peaks in the data, has been included. The scatter in the data is much smaller, but the similar temporal behaviour is still present.

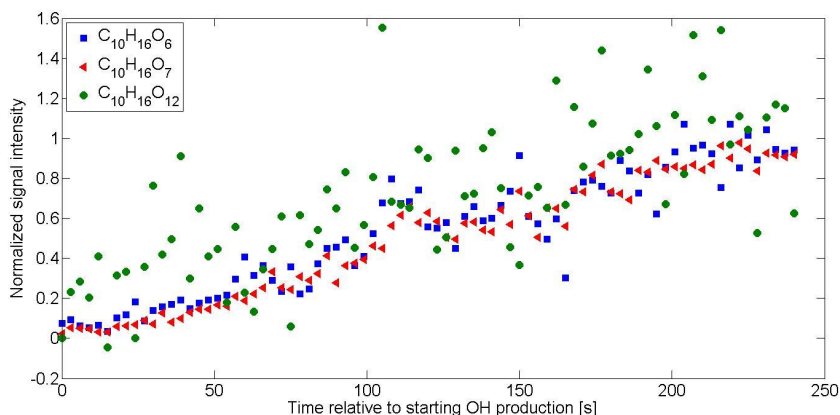


Figure 3.4 Comparison of formation rates of HOM with drastically different oxygen number, i.e. oxidation state. Formation rate was calculated by using data acquired after OH production was initiated. Comparing the normalized intensities of the different compounds shows they have the same formation rate. Normalization was done by dividing each HOM signal with the maximum signal of the respective HOM. Data used is 3 second averaged data, with running average. The compounds used here are  $C_{10}H_{16}O_6$ ,  $C_{10}H_{16}O_7$ , and  $C_{10}H_{16}O_{12}$ .  $C_{10}H_{16}O_6$  is the first hydroperoxide we can detect with the CIMS with any accuracy, while  $C_{10}H_{16}O_{12}$  is the hydroperoxide with highest oxidation state we can reliably detect. As can be seen, it has higher dispersion as the two other compounds shown.  $C_{10}H_{16}O_7$  is the highest intensity hydroperoxide in the photooxidation experiments, chosen here to show that compounds that we are detecting with high intensity have same behaviour as smaller intensity peaks.

All three compounds exhibit similar formation rates, despite having very different number of oxygens being added during formation. This similarity in temporal shapes of production rates of compounds with different oxidation states shows that the process is extremely fast indicating that autoxidation is a strong formation mechanism during photochemical HOM formation.

As there are no data available on the H-shift rates, it would be possible that very slow H-shift could mimic the effect of sequential OH oxidation, and produce different formation rates for heavier HOM molecules. On the other hand, and considering general lifetimes of RO<sub>2</sub> and the quasi-instantaneous formation of HOM (Jokinen et al., 2014) the H-shifts should occur in the order of 10 seconds or faster. If the main mechanism driving HOM formation from photooxidation would be autoxidation, there would be no reason for a difference between the formation rates of a compound with 10 oxygens, compared to one with six oxygens, because O<sub>2</sub> is much more abundant than OH and the intramolecular reactions would be very fast. The differences in formation times would be in too small time scales to see with the instrument used here.

### 3.5. Effect of OH concentration on end product pattern

Assuming sequential OH oxidation, it would be justifiable to expect that with higher OH concentrations the pattern of HOM formation end products would shift towards higher oxidation states, e.g. C<sub>10</sub>H<sub>16</sub>O<sub>7</sub> would decrease in relation to total HOM production and C<sub>10</sub>H<sub>16</sub>O<sub>10</sub> would increase. In the data there are no indications of this. Figure 3.5 shows α-pinene OH HOM formation under two different [OH]. In the low [OH] case the [OH] is less than half of that in the high [OH] case ( $1.92 \cdot 10^7$  and  $4.77 \cdot 10^7$  cm<sup>-3</sup>, respectively). With a difference of this magnitude, it could be expected that differences in oxidation rates would be visible if they existed. In Figure 3.5 there seems to be no systematic change towards higher oxidation states, instead the increase in HOM formation increases similarly regardless of the mass of the HOM.

However, it could be that small relative changes are masked by the overall increase of HOM formation due to increased [OH] and [HO<sub>2</sub>] concentrations. To account for that, Figure 3.6 depicts the relative increase of HOM formation over the mass spectrum from the presented low [OH] case to high [OH] case. Now it can be easily seen that there is no clear shift towards higher masses with higher [OH]. There are differences in the relative increases of different peaks throughout the masses, with variability from roughly 5 % to up to 60 %, but this is more systematic depending on the compound group of the individual compound than the respective oxygen number. For example, peroxy radical peaks show large variation (~5-30 %), while increases in hydroperoxide signals are generally in the range of 25-40 %.

However, as OH could be a potential source as well as a sink to each peak, this result alone does not offer conclusive evidence for autoxidation.

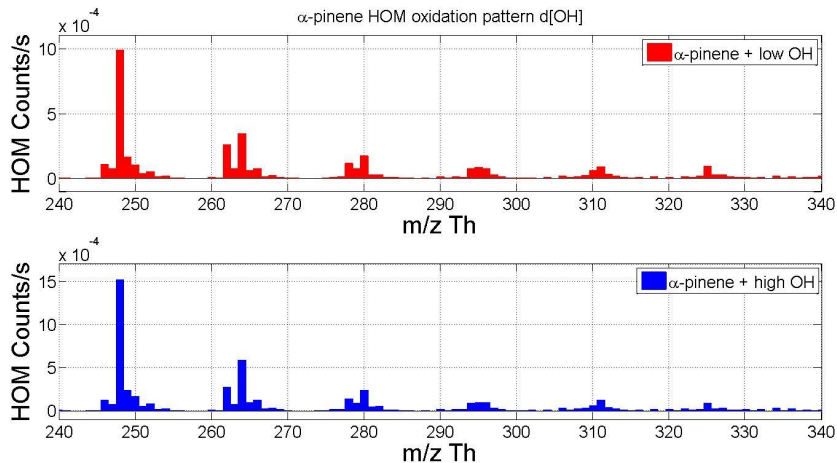


Figure 3.5 Upper panel shows  $\alpha$ -pinene HOM formation under lower [OH] conditions ( $1.92 \cdot 10^7 \text{ cm}^{-3}$ ), and lower same for higher OH concentration ( $4.8 \cdot 10^7 \text{ cm}^{-3}$ ). If HOM formation would be a result of sequential OH oxidation, an assumption would be that the relative intensities in the lower panel (high [OH]) would be shifted towards higher masses, i.e. higher oxidation states, when compared to the lower [OH] case. The total intensity of HOM formation has increased, but there is no indication that there is higher production of more oxidised HOM molecules. Note the difference in Y-axes.

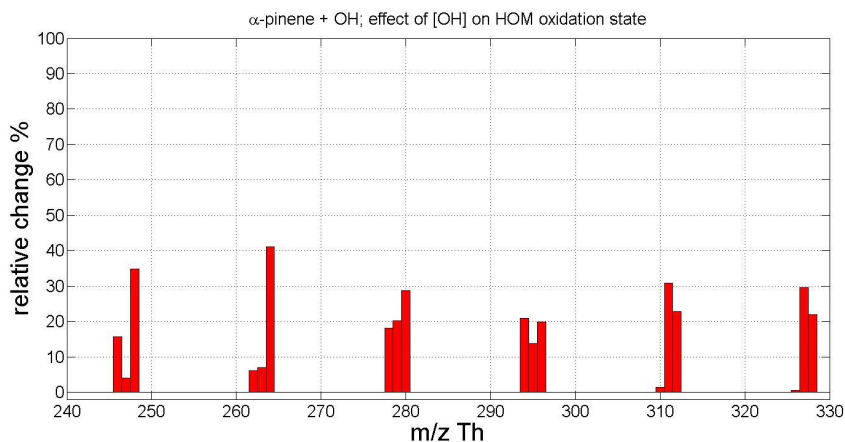


Figure 3.6 Relative increase of selected HOM compounds (order in clusters: ketones, peroxy radicals, hydroperoxides) when comparing  $\alpha$ -pinene HOM formation at low and high [OH] shown in Figure 3.5. There is no higher relative increase in closed shell end products with higher oxygen content at higher [OH]. There seems to be a tendency in peroxy radicals of OH enhancement towards higher masses, but as the signals of peroxy radicals are low compared to the other products, small changes may magnify artificially high.

### 3.6. Conclusion: autoxidation versus sequential oxidation

From the previous experiments, the inhibiting effect using fully deuterated compound instead of hydrogenated version has on HOM formation, the lack of shift towards higher oxidation states with higher OH concentration, and the nearly identical formation rates of compounds with very different number of oxygen atoms in them, it can be concluded that a sequential OH oxidation is not very important for HOM formation once the HOMs have at least six O atoms. The consistent results from different experiments, even if not conclusive on their own, together give enough evidence on the importance of autoxidation as a major mechanism behind photochemical HOM formation.

However, contributions of first generation product oxidation cannot be ruled out. As an example, pinonaldehyde oxidation might contribute to HOM formation from  $\alpha$ -pinene or nopinone oxidation can contribute to HOM formation from  $\beta$ -pinene (see Chapter 3.8.).

In light of the results shown here, autoxidation seems to be more plausible formation mechanism for photochemical HOM formation. This does not exclude that each closed shell HOMs can be attacked by OH and start a new autoxidation sequence.

### 3.7. Experiment to study the role of O<sub>2</sub> in the photochemical HOM formation

It has been shown that under low O<sub>2</sub> conditions ozonolysis borne HOM formation is suppressed strongly (Jokinen et al., 2014; Berndt et al., 2015). To test this in JPAC, most of the oxygen flowing in to the chamber was replaced by N<sub>2</sub>, to reach low enough levels of oxygen to prevent O<sub>2</sub> addition to the alkyl radical. The [O<sub>2</sub>] was reduced in the chamber to levels lower or comparable to those reported by Jokinen et al. (2014).

Figure 3.7 shows the results from the ozonolysis experiment. The time series depicts total monomer and dimer concentrations, and begins with low O<sub>2</sub> concentration with HOM formation in steady state. When O<sub>2</sub> is returned to the chamber (14:15), HOM formation begins to increase immediately until about an hour later it reaches new steady state. When using this as a reference to ozonolysis produced HOM, we can see that the lowered O<sub>2</sub> regime suppressed HOM formation by nearly three quarters. This is due to less oxygen being available to attach into the alkyl radical produced by H-shift in the peroxy radical. This is in accordance with assumption that ozonolysis HOM formation is driven by internal H-shifts.

Individual compound classes had slightly different level of reduction, but no systematic difference between compounds with different oxidation states was observed.

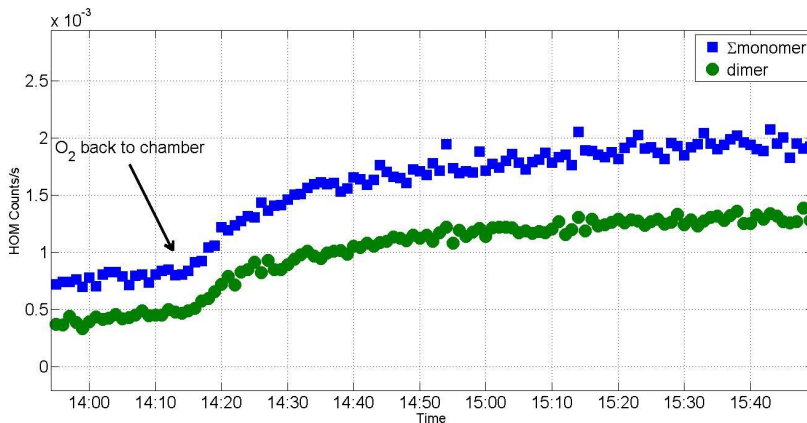


Figure 3.7 Summed monomer and dimer range compounds from  $\alpha$ -pinene ozonolysis HOM formation during low  $[O_2]$ . At the beginning of the time series is depicted HOM formation when  $[O_2]$  has been reduced to below 1%.  $O_2$  is then introduced back into the chamber, and as can be seen both monomer and dimer formation increase 4-fold when comparing low oxygen and normal oxygen parts of the experiment. This is a repeat experiment reported by Jokinen et al. (2014) and Berndt et al. (2015) and shows that their results can be duplicated in JPAC.

Next logical step was to test whether the HOM formation via photochemistry would be similarly suppressed at the same low  $O_2$  concentration. In Figure 3.8 is shown time series for total monomer and dimer concentrations, when  $O_2$  flow is being replaced by  $N_2$  flow, and as can be seen, there is no suppression observed. There is a small fluctuation in the concentration during the replacement, but there is no clear difference in HOM concentrations between  $O_2$  mixing ratio of 21 % and below 1% respectively.

At the same  $O_2$  concentration, the effect of low  $O_2$  on HOM formation via ozonolysis is obvious whereas it is negligible in case of photooxidation. This might be seen as a hint to a significant impact of sequential OH oxidation to HOM formation from photooxidation. But this was ruled improbable based on the results described before. The negligible effect of  $O_2$  removal on photochemical HOM formation is only explainable by a very fast  $O_2$  addition. Indeed, the high pressure limit for  $O_2$  addition to alkyl radicals is reached the earlier the larger the alkyl radical is (Finlayson-Pitts and Pitts, 2000). As  $\alpha$ -pinene HOMs are large molecules with the ability to distribute the excess energy into many internal energy forms, such high efficiency seems possible. However, the difference to the clear effects for ozonolysis born HOMs is not easily explainable and can only be speculated on.

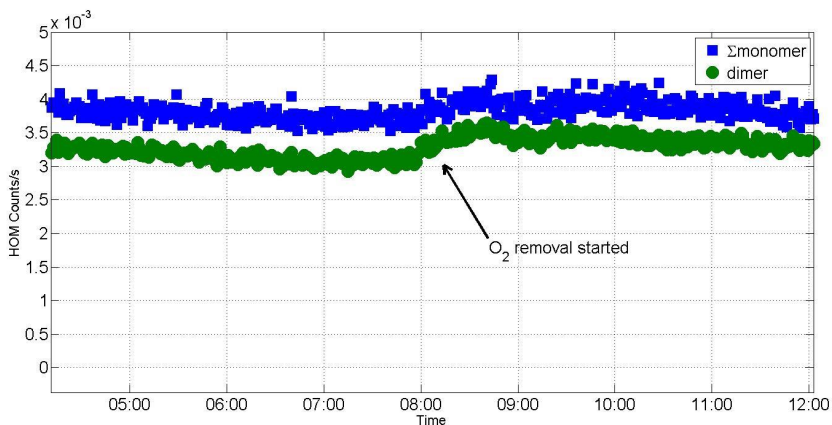


Figure 3.8 Time series with total HOM monomer and dimer concentrations during an experiment, where most of the oxygen in the reaction chamber was replaced by  $N_2$ . The aim of the experiment was to test, whether limiting accessible oxygen in the reaction chamber would slow down, or decrease HOM formation under photooxidation, as has been shown in the case of ozonolysis (Jokinen et al., 2014). In results shown here, the total HOM production did not decrease, which could be due to extremely fast autoxidation.

One possible explanation is that the structure of the peroxy radical that is formed is different depending on the oxidizing agent. With ozone the formation goes via vinylhydroperoxide pathway, and there is a small energy barrier caused by the delocalization of the electron to form the Criegee intermediate before  $O_2$  addition is possible to form the peroxy radical to begin HOM formation. In contrast, OH is added directly to the double bond without breaking the ring, and there is no energy barrier preceding the  $O_2$  addition. This would mean that the difference in formation begins at the first step of oxidation, and that the resulting HOM molecules have very different structures depending on the oxidation agent. The energy barrier in ozonolysis  $RO_2$  formation may be strong enough to cause significant enough difference in the formation thingy to slow the first step peroxy radical formation in ozonolysis case but not enough to inhibit photochemical  $RO_2$  formation.

The conclusion from the experiment is that  $O_2$  concentrations that are sufficiently low to suppress HOM formation via ozonolysis are not low enough to suppress photochemical HOM formation. Likely, the entrance channel in autoxidation is affected differently comparing ozonolysis and OH reaction.

This experiment does not offer more proof to autoxidation directly, but it also does not dispute it. However, these results mean that the autoxidation must very efficient because HOMs are produced effectively even in low oxygen conditions.

## Chapter 3.8. Photochemical HOM formation under reduced influence of ozonolysis

In Chapter 3.6. it was concluded that the likely main mechanism for photochemical HOM formation is autoxidation, but that sequential OH oxidation is likely to contribute to some extent. In this part, the focus will be on compounds that do not react with ozone, or react only very slowly, to estimate how general photochemical HOM formation is, and whether reaction with ozone is required as a first step in photochemical HOM formation. As already described experiment overview the examples used here are  $\beta$ -pinene, methyl salicylate (MeSA), and benzene.

### 3.8.1. Photochemical HOM formation from $\beta$ -pinene

At first the focus will be on  $\beta$ -pinene, as an example of a compound with an exocyclic double bond as opposed to endocyclic one like in  $\alpha$ -pinene, and to study how that effects HOM formation. Figure 3.9 shows an example spectrum from HOM formation from  $\beta$ -pinene photooxidation. Compared to the  $\alpha$ -pinene experiment shown in Figure 3.2, the OH concentration was less than a factor of two lower ( $2.61 \cdot 10^7$  and  $4.55 \cdot 10^7 \text{ cm}^{-3}$ , respectively). OH dependency of  $\beta$ -pinene HOM formation will be covered in Chapter 4.

When comparing the HOM patterns in Figures 3.2 and 3.9, some differences can be seen. In  $\beta$ -pinene the mass spectrum seems more smeared. There is no clear sign of a progression of 32 Th, or 16 Th with few clearly dominant peaks at every cluster, as was the case with  $\alpha$ -pinene. This is a result of fragmentation of  $\beta$ -pinene during oxidation, leading to the formation of  $C_9$ - and  $C_8$ -compounds. Nopinone, an oxidation product from  $\beta$ -pinene, can then further react with OH, to produce another peroxy radical series which HOMs can be formed (see Appendix for peak lists). This leads to overlapping patterns in mass spectrum. In comparison, monomer HOM termination products from  $\alpha$ -pinene photooxidation are almost purely  $C_{10}$ -compounds.

The rate constant of  $\beta$ -pinene-ozone reactions is quite low, and it has been shown that  $\beta$ -pinene is not as efficient in HOM formation under ozonolysis as  $\alpha$ -pinene. Reaction rate of  $\beta$ -pinene with OH, on the other hand, is somewhat higher than that of  $\alpha$ -pinene; photooxidation could thus provide an efficient pathway to HOM formation from  $\beta$ -pinene.

Without endocyclic double bond, there is no ring opening to produce a molecule with two functional groups, a prerequisite of efficient HOM formation (Mentel et al., 2015). For these reasons it has been noted that endocyclic double bonds seem to support HOM formation (Mentel et al., 2015; Ehn et al., 2012; Jokinen et al., 2014). This seems to be the case with ozonolysis, but photooxidation is considerably different process, and thus might offer additional pathways for HOM formation, without attack to the endocyclic double bond, and subsequent ring opening.

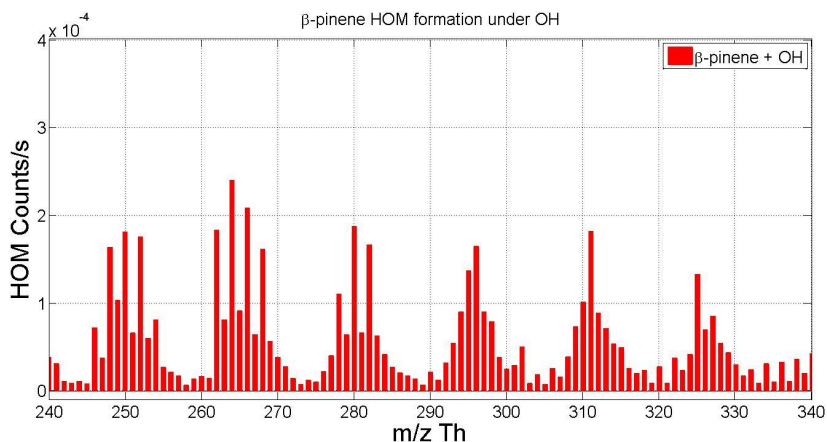


Figure 3.9 Spectrum of photochemical HOM formation from  $\beta$ -pinene, monomer range. Compared to  $\alpha$ -pinene, the pattern of HOM formed from  $\beta$ -pinene is much more complex due to fragmentation of  $\beta$ -pinene into  $C_8$ - and  $C_9$ -compounds, something that is very rare with  $\alpha$ -pinene. Difference in intensities compared to  $\alpha$ -pinene (Figure 3.2) are mainly due to differences in [OH] and [VOC] during the experiments.

The conclusion from  $\beta$ -pinene experiment is that HOM formation is possible from compounds with exocyclic double bonds, i.e. in photochemical HOM formation an endocyclic double bond is not required.

### 3.8.2. Photochemical HOM formation from methyl salicylate and benzene

To further demonstrate the prevalence of HOM formation under photooxidation, results from two benzenoid compounds, methyl salicylate (MeSA,  $C_8H_8O_3$ ) and benzene ( $C_6H_6$ ) are presented. Neither MeSA nor benzene contains a double bond; reactions with ozone are therefore very inefficient and HOM formation from these compounds must originate from photooxidation.

In Figure 3.10 is shown HOM formation from MeSA on monomer range, with few main end products identified as an example to demonstrate the O/C ratios, which are all in four chosen compounds over 1 (1.1. - 1.4).

Figure 3.11 is depicting photooxidation HOM formation from benzene. As can be seen, there are relatively well defined monomer and dimer ranges from benzene. Few example peaks have been identified to highlight the molecular composition of the end products.

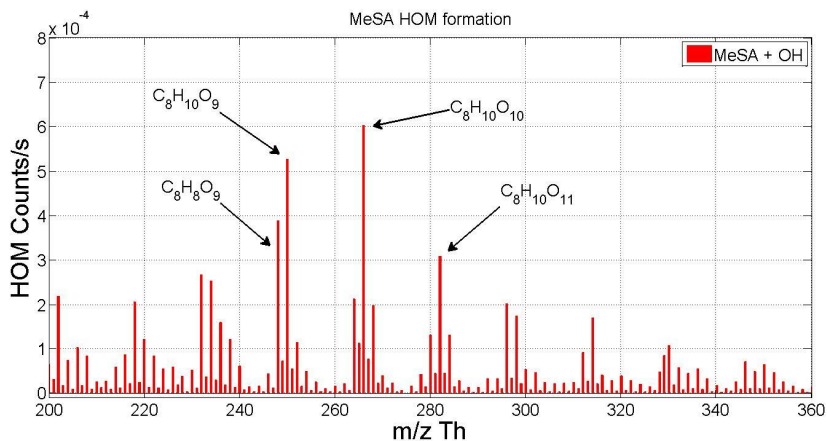


Figure 3.10 Example of methyl salicylate photooxidation HOM spectrum. Identification for few main closed shell end products has been marked.

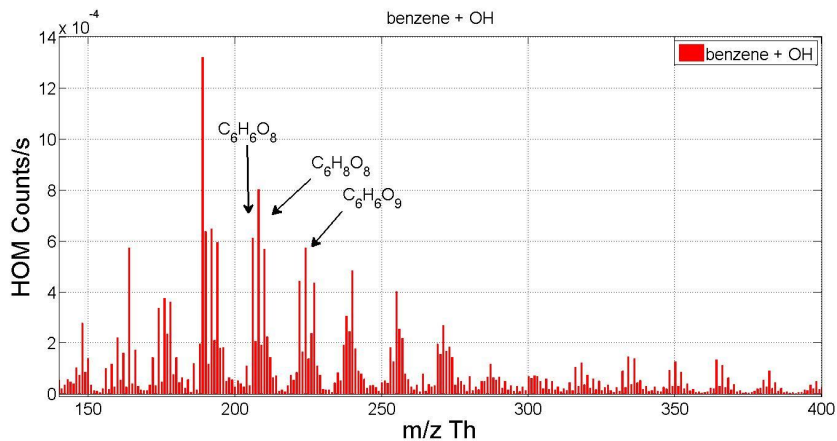


Figure 3.11 Example of benzene photooxidation HOM spectrum showing monomer and dimer ranges. Few main end product peaks have been identified as an example, two hydroperoxides and one ketone. The instrument reagent ion tetramer peak ( $(HNO_3)_3 \cdot NO_3^-$ , here at 188 TH) overlaps with monomer range of the benzene HOM, and appears as the largest peak of the mass spectrum.

When considering the results shown here, from  $\alpha$ -pinene,  $\beta$ -pinene, MeSA, and benzene, it is clear that HOM formation from photooxidation is widely occurring phenomenon, and not as strictly limited as it is in the case of ozonolysis. This is understandable as OH is less specific oxidant than ozone, and can lead to a wide variety of oxidation products, as the possibility of further oxidation by OH of oxidation product increases the variety of end products.

## Chapter 4 Photochemical HOM production

In Chapter 3 the formation mechanism of HOM via photooxidation was investigated, and identified to be mainly autoxidation. In this chapter the focus will be on the details and dependencies of HOM production on [OH] as a function of oxidation rates ( $k_{\text{OH}}[\text{OH}][\alpha\text{-pinene}]$ ). The effect of changing [OH] and [HO<sub>2</sub>] on HOM formation will be covered in this chapter. This is an important factor for Chapter 5 with regard to the effect of NO<sub>x</sub> on photochemical HOM formation and HOM nitrate formation.

### 4.1. OH dependency of photochemical HOM from $\alpha$ -pinene

Figure 4.1 shows total HOM formation from  $\alpha$ -pinene as a function of  $k[\alpha\text{-pinene}][\text{OH}]$ . Due to the response differences of monomer and dimer range HOM to OH oxidation, the concentration of monomer and dimer range HOM have been separated for clarity.

When discussing or showing results, the term monomer is defined to be the sum of all peaks at  $m/z$  range from 240 to 370 Th (C<sub>10</sub>-compounds), while for the term dimer the range of 370 to 530 Th (predominantly C<sub>20</sub>-compounds) was chosen. When referring to peroxy radicals, hydroperoxides, or ketones in this chapter (or nitrates in Chapter 5), all compounds formed in reactions R1.3e – R1.3h and R5.1a-R5.1c, and whose molecular formula has been identified (see  $\alpha$ -pinene peak list in Appendix) are included.

In Figure 4.1 it can be seen that at low [OH], when ozonolysis is the main oxidation agent in the system, the monomer concentration is ~50% higher than the dimer concentration. The monomer concentration increases in pseudo-linear way (non-linear, non-exponential), and exhibits no indication of saturation at higher  $\alpha$ -pinene oxidation rates. Dimer concentration increases faster at lower  $k_{\text{OH}}[\text{OH}][\alpha\text{-pinene}]$  ( $1\text{-}4 \cdot 10^7 \text{ cm}^{-3}\text{s}^{-1}$ ), but slows down with further [OH] increase and reaches saturation at  $k_{\text{OH}}[\text{OH}][\alpha\text{-pinene}]$  of  $\sim 7 \cdot 10^7 \text{ cm}^{-3}\text{s}^{-1}$ . Possible explanations for this dimer range saturation will be presented later, when addressing single peroxy radical termination product groups and their response to increased [OH] and [HO<sub>2</sub>].

Ozonolysis is providing relatively high background HOM formation. For monomers ozonolysis background is approximately  $1.5 \cdot 10^{-3}$  counts/s, or about 25% compared to the total HOM monomer concentration during highest [OH], and for dimers  $1.0 \cdot 10^{-3}$  counts/s, or ~30%. If calculating the ratio of oxidation rates of  $\alpha$ -pinene with OH and  $\alpha$ -pinene with ozone for the duration of the experiment, there is a linear increase of  $\alpha$ -pinene reacting with OH from low to high [OH] going from > 2 at low [OH] to nearly 80 at highest [OH] (cases with ozonolysis alone have been excluded). As a function of  $\alpha$ -pinene oxidation rate the increase is exponential, and thus it can be said that the increase at higher oxidation rates is dominated by HOM formation from  $\alpha$ -pinene photooxidation. Using these numbers it can be estimated that there is an increase of  $5.0 \cdot 10^{-3}$  counts/s in monomer and  $3.2 \cdot 10^{-3}$  counts/s in dimer concentrations that can be attributed to photochemistry.

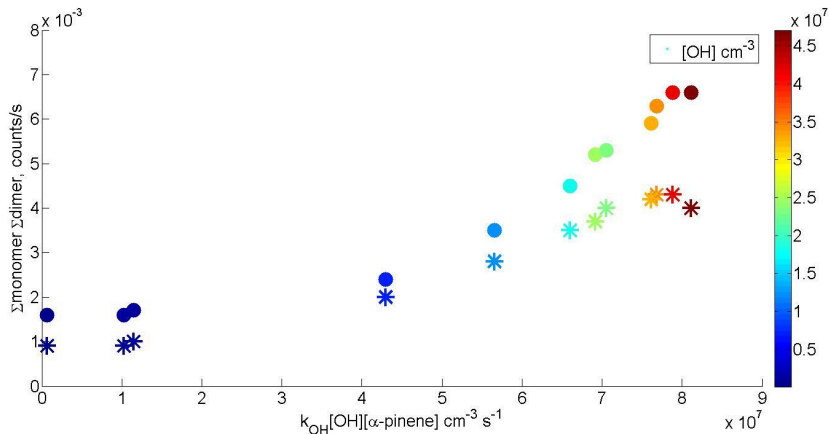


Figure 4.1 Total HOM monomer (circles) and dimer (stars) concentrations from  $\alpha$ -pinene photooxidation as a function of  $\alpha$ -pinene oxidation rate. [OH] is included as colour code to further highlight the [OH] dependence of HOM production. HOMs produced by ozonolysis can be seen as relatively high background (about  $1.5 \cdot 10^{-3}$  counts/s for monomers and  $1.0 \cdot 10^{-3}$  counts/s for dimers). Monomer concentrations increase clearly with increasing [OH] and  $k_{OH}[OH][\alpha\text{-pinene}]$ . Dimer concentrations show faster response to increased [OH] at lower [OH] range, but reaches saturation at oxidation rates of around  $\sim 7 \cdot 10^7 \text{ cm}^{-3} \text{ s}^{-1}$  ([OH]  $3.5 \cdot 10^7 \text{ cm}^{-3}$ ).

Increasing either OH or  $\alpha$ -pinene concentrations (or both) enables faster  $\alpha$ -pinene + OH reactions, which at higher concentrations leads to particle formation. This set limits to the range of [ $\alpha$ -pinene] and [OH] used during the experiment. When investigating gas phase concentrations of easily condensing vapours, particle formation has to be avoided, as increased particle surface in the chamber increases the condensational sink of the vapours, and thus changes the vapour loss rates. Another issue with too high OH concentrations is the possibility of adding sequential OH reactions as an oxidation mechanism, which would lead to very complicated systems. For these reasons the OH concentrations used in the experiments were limited to maximum  $5 \cdot 10^7 \text{ cm}^{-3}$  (for  $\alpha$ -pinene) and  $7 \cdot 10^7 \text{ cm}^{-3}$  (for  $\beta$ -pinene). Despite this, the OH concentrations used in experiments shown in this chapter are an order of magnitude above realistic atmospheric concentrations in clean environments. This high [OH] is used due to the short residence time in the chamber ( $\sim 45$  minutes) and by using higher OH concentrations aging effect that takes place in the atmosphere after half a day or more can be mimicked within the chamber residence time.

Before looking at the results from individual end product groups, a few comments about distinguishing the hydroperoxides from alcohols needs to be given. R1.3e and R1.3f both give out the same molecular sum formula for the end product, however with different functionalization. R1.3e is the hydroperoxide termination product pathway from peroxy radical  $m$ , giving a mass  $m+1$ . From R1.3f mass  $m'-15$  (when

$m'$  is  $RO_2$  with one more oxygen atom than  $m$ ) can be determined, which cannot be distinguished from mass  $m+1$  in our instrument.

In practice this means that for the results for hydroperoxides, the sum of “hydroperoxides” also includes alcohols from the  $RO_2 + RO_2$  reactions. However, assuming that ketones and alcohols are produced in an approximately 1:1 relation, we can use ketones as proxy/first estimation for alcohol production. This approach assumes additionally that the instrument is similarly sensitive to both alcohols and ketones, which cannot at present be verified. However, even with this limitation, this is the best available approach currently.

Figure 4.2 shows the ratio of the sum of all “hydroperoxides” to the sum of all ketones (used here as proxy for alcohols). It can be seen that apart from low  $[OH]$  conditions when ozonolysis is the main oxidant and  $HO_2$  concentration in the system is low, hydroperoxide formation clearly surpasses alcohol production. It is therefore justifiable to continue interpreting this signal as predominantly hydroperoxide when considering high  $HO_2$  concentration cases, as is done in this work. Hydroperoxide formation induced by OH begins at  $k_{OH}[OH][\alpha\text{-pinene}]$  of  $1\text{-}3 \cdot 10^7 \text{ cm}^3\text{s}^{-1}$  (ratio  $\sim 1$ ,  $[OH] \sim 5 \cdot 10^6 \text{ cm}^{-3}$ ), and at  $k_{OH}[OH][\alpha\text{-pinene}]$  of  $\sim 7 \cdot 10^7 \text{ cm}^3\text{s}^{-1}$  ( $[OH] \sim 2 \cdot 10^7 \text{ cm}^{-3}$ ) the ratio of hydroperoxide to ketone reaches 2.5, and it can be assumed that the hydroperoxide concentration exceeds the alcohol concentration. At higher  $[OH]$ /oxidation rates the increase in signal can be attributed to increased hydroperoxide concentration.

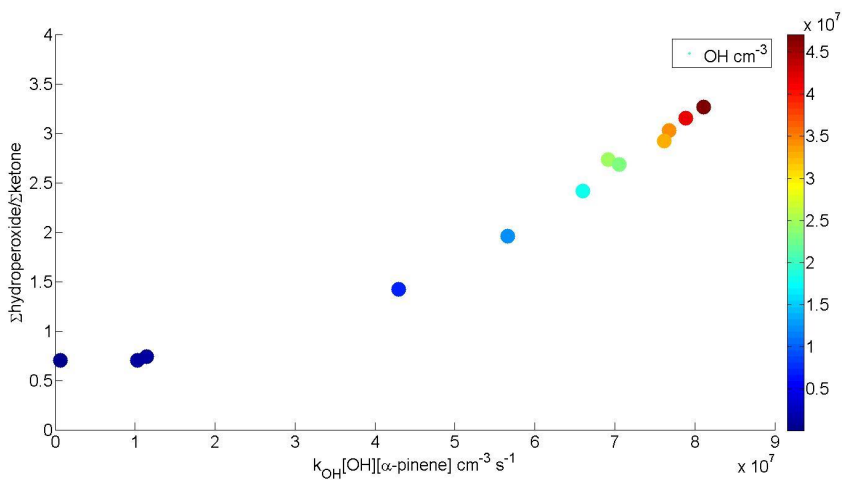


Figure 4.2 Ratio of the total signal of all hydroperoxide peaks to total ketone signal, used here as a proxy to alcohol formation.  $[OH]$  indicated by colour code. Ratio increases to above 2.5 at  $\sim 7 \cdot 10^7 \text{ cm}^3\text{s}^{-1}$  after which hydroperoxide can be assumed to dominate the  $m+1$  signal.

In this work, when using the term hydroperoxide in reference to measurement results, it needs to be kept in mind that there is a small contribution from alcohols included in that signal, unless otherwise mentioned.

In the following more details about the OH dependency of specific termination product groups will be given. Figure 4.3 shows the total production of peroxy radicals, hydroperoxides, and ketones as a function of oxidation rates. At low [OH] and [HO<sub>2</sub>], when ozone is the dominant oxidant, ketones are the main termination products at monomer range, although, as there was no OH scavenging during the experiment, some OH produced hydroperoxides may have been formed. This is in accordance with known peroxy radical chemistry under ozonolysis. With increasing [OH] and [HO<sub>2</sub>] the amount and fraction of hydroperoxides begin to increase. From classical peroxy radical chemistry it can be concluded that most of this increase is due to increased reactions of RO<sub>2</sub> + HO<sub>2</sub> (R1.3e), and thus the increase in HOM monomer production can be mainly attributed to higher hydroperoxide production.

The results in Figure 4.3 show that under photochemical HOM formation hydroperoxides by far dominate the monomer range end product formation. Even if assuming the “ketone/alcohol correction”, at  $k_{OH}[OH][VOC] > 5.0 \cdot 10^{17} \text{ cm}^{-6}$  hydroperoxides are dominating the end product formation, and show a strong increase as the oxidation rate increases. Both peroxy radical concentration and ketone concentration show increase of about 50 %, but as all peroxy radicals and ketones have small intensities compared to hydroperoxide signals, even these relatively large changes do not contribute much to the overall HOM concentration which is dominated by hydroperoxides.

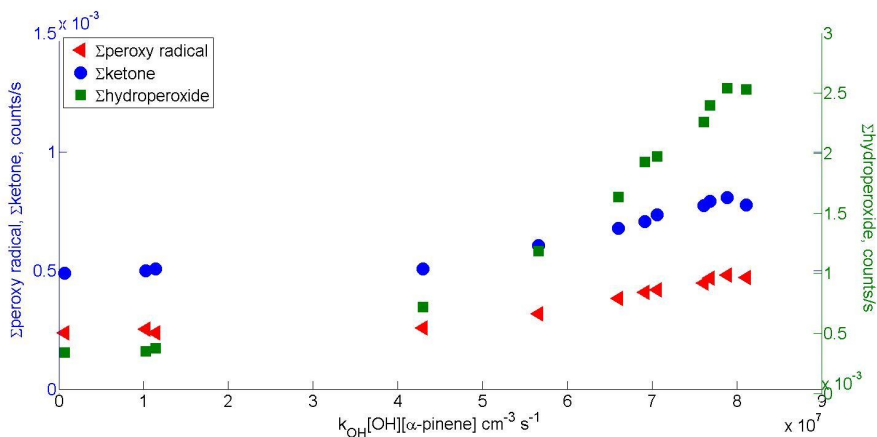


Figure 4.3 Summed peroxy radical, hydroperoxide, and ketone signals as a function of oxidation rate. As can be seen, increasing [OH] (and thus increasing  $\alpha$ -pinene · OH reactions) increases both the absolute amount and the portion of hydroperoxides produced. In general the increase is most clear in case of hydroperoxides, but there is an increase observed in ketones and peroxy radicals as well (~50%, a large change in relative terms, but small in comparison to the actual increase of hydroperoxide concentration).

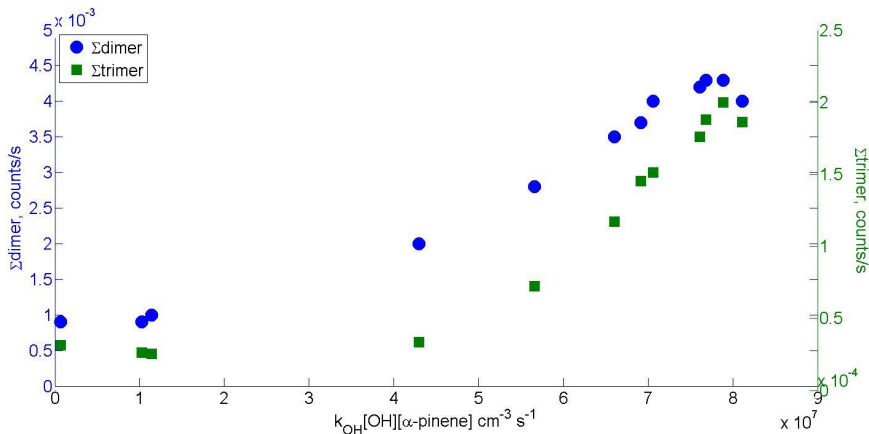


Figure 4.4 Total HOM dimer and “trimer” concentrations as a function of  $\alpha$ -pinene oxidation rate. Term “trimer” is here used to refer to observed compounds in the mass spectrum at masses > 600 Th, with  $\sim 30$  C-atoms. The “trimer” concentration increase begins at higher oxidation rates than for the dimer and is also steeper. This might indicate a source from dimer oxidation.

The decrease of the total dimer concentration at high oxidation rates in Figure 4.1 could be an indication of this shift from ketones and alcohols to hydroperoxides. Dimer production reaches saturation, while such clear saturation was not observed for the HOM-monomers. If  $[\text{HO}_2]$  increases with increasing  $[\text{OH}]$ , more hydroperoxides are formed on cost of other termination products, such as dimers. In this light the decrease of the dimer to monomer ratio is conceivable.

It is also possible that at high  $[\text{OH}]$  HOM dimers react with OH, introducing a new/additional sink to dimers. Due to lower wall losses of dimers compared to wall losses of monomers (Chapter 6) the lifetime of dimers in the chamber is somewhat longer than that of monomers. Assuming similar rate coefficients of  $\text{OH} +$  closed shell HOM-monomer reactions and  $\text{OH} +$  dimer reactions, a decrease of the dimer to monomer ratio with increasing  $[\text{OH}]$  is also conceivable. Indications for this can be seen at high  $[\text{OH}]$  when there is an observable increase in signal at high  $m/z$  compounds (> 600 Th) with  $\sim 30$  C-atoms (HOM “trimers”, see Figure 4.4). The existence of these compounds could be explained by reactions of OH with HOM dimers, producing peroxy radical and then further terminating in dimer- $\text{RO}_2 +$  monomer- $\text{RO}_2$  – reactions. This is however hypothetical.

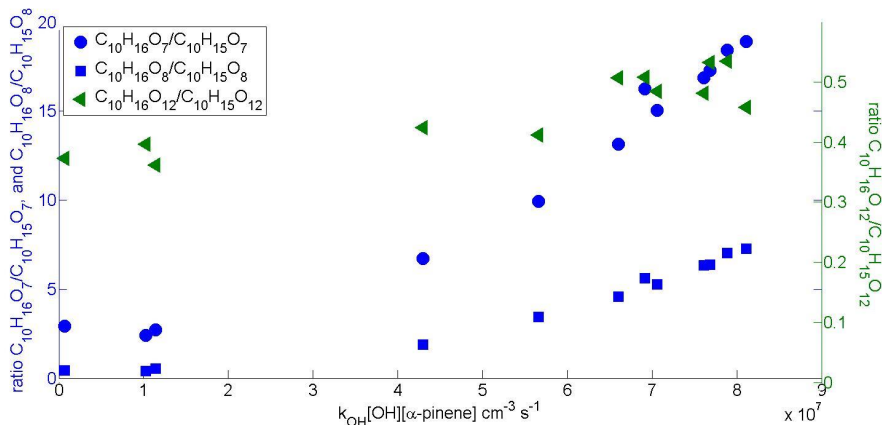


Figure 4.5 Fractions of peroxy radicals and corresponding hydroperoxide plotted here as a function of oxidation rate. With increasing [OH] and [HO<sub>2</sub>] the ratio of hydroperoxide is increasing linearly compared to peroxy radicals. Increasing peroxy radical production competes with increased sink via additional RO<sub>2</sub>' + HO<sub>2</sub>' – reactions leading to hydroperoxide, a termination product. At high oxidation state (green triangles, 12 oxygen atoms) the signal intensities become small, and the observed change is negligible.

Figure 4.5 illustrates examples of fractions of three peroxy radicals and their corresponding hydroperoxide as a function of  $\alpha$ -pinene oxidation rate. It further demonstrates that the reaction pathways are shifting towards RO<sub>2</sub> + HO<sub>2</sub> – reactions, with more hydroperoxides produced at higher [OH] and [HO<sub>2</sub>]. With higher [OH], more peroxy radicals are produced, but there is an increase of the peroxy radical sink as well, when more HO<sub>2</sub> is available to react with the peroxy radicals. This leads to an increase in hydroperoxide concentrations, but no significant further increase in peroxy radical concentrations.

For comparison, Figure 4.6 shows the ratio between a ketone (C<sub>10</sub>H<sub>14</sub>O<sub>7</sub>) and the related peroxy radical (C<sub>10</sub>H<sub>15</sub>O<sub>8</sub>) development with different oxidation rates. A small fluctuation of the ratio can be seen, but as the intensities of both signals are relatively low, extreme caution is needed in interpreting results as quite small changes in intensity can lead to large apparent changes of the ratio. Furthermore, the variation of this ratio lies mainly within the chosen error limit (standard deviation of ketone signal during one experiment), and therefore it can be stated that there is no discernible trend in ketone/peroxy radical ratio.

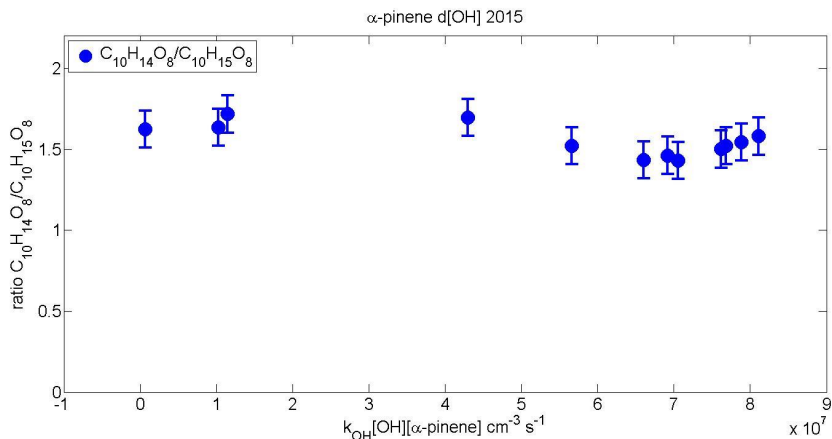


Figure 4.6 Ratio of ketone ( $C_{10}H_{14}O_7$ ) and the corresponding peroxy radical ( $C_{10}H_{15}O_8$ ) as a function of  $k_{OH}[OH][\alpha\text{-pinene}]$ . Ketones are the main termination products for ozonolysis HOM formation, and it can be seen that with increasing  $HO_2$  concentration, there is a small decrease of the ratio. However, as signal strengths of both HOMs are small, care has to be taken when interpreting results. Error bars shown are standard deviations of the respective signals during one experiment and are used as an example of minimum errors. As can be seen, nearly all changes fit within this minimum error range. Therefore it can be concluded that the ratio does not change substantially.

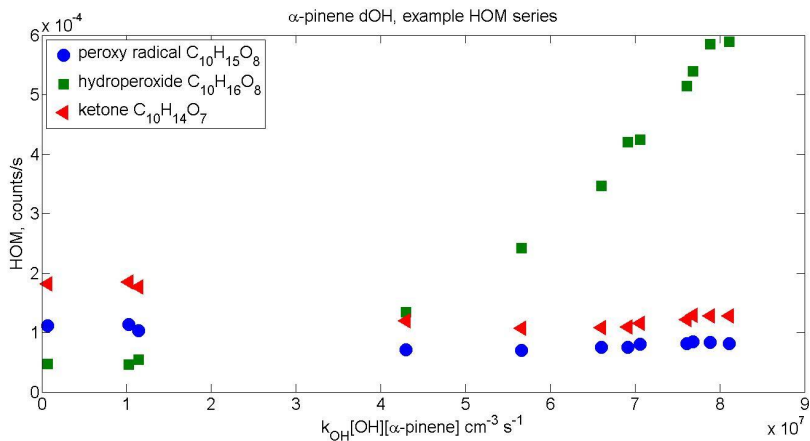


Figure 4.7 An example of single peroxy radical “series” as a function of  $k_{OH}[OH][\alpha\text{-pinene}]$ . There is a decrease in ketones and peroxy radicals, with a strong increase in hydroperoxide production. Both ketone and peroxy radical productions seem to reach steady state relatively soon, but the increase of the hydroperoxide continues linear during the experiment range. This is a good example on how the increased sink into hydroperoxide production can mask the increase of peroxy radical formation.

Using the peroxy radical  $C_{10}H_{15}O_8^{\cdot}$  as an example, Figure 4.7 shows a single peroxy radical series, and how the intensities of the different end products change as a function of  $k_{OH}[OH][\alpha\text{-pinene}]$ . Compared to the concentrations of all summed compounds shown in Figure 4.3 there are some changes seen due to concentrating on one peroxy radical series, such as a more pronounced decrease of ketones and peroxy radicals compared to ozonolysis conditions.

With very low  $[OH]$  (when HOM formation by  $O_3 >$  HOM formation by  $OH$ ) the ketone ( $C_{10}H_{14}O_7$ , red triangles) is the main end product from the peroxy radical ( $C_{10}H_{15}O_8^{\cdot}$ , blue circles). However, increasing  $[OH]$  and  $[HO_2]$  in the system shifts the peroxy radical termination product pathway away from the ketone and towards the hydroperoxide ( $C_{10}H_{16}O_8$ , green squares). Under low  $[HO_2]$  conditions the formation of hydroperoxide is minimal, but with higher  $[OH]$  and  $[HO_2]$  the hydroperoxide pathway (R1.3e) quickly overcomes that of ketone production, and starts to dominate the total HOM formation. The increase of the hydroperoxide concentration shows linear dependence on the oxidation rate. After the initial decrease at reaction rates higher than  $\sim 4 \cdot 10^7 \text{ cm}^{-3}\text{s}^{-1}$  the ketone concentration remains relatively stable with increasing oxidation rate.

To hypothesise, the decrease seen here in peroxy radical concentrations is a result of the increased sink for the radical. With higher reaction rates the production of the peroxy radical increases, while at the same time increasing  $[OH]$  leads to higher  $[HO_2]$  in the system. This in turn means reaction R1.3e becomes more pronounced, which can be seen as an increased hydroperoxide signal. This increase of the sink is at first strong enough to slightly lower the peroxy radical concentration present in the chamber slightly, but the formation/termination rate of peroxy radical evens out at higher  $[OH]$ , and further increase of  $[HO_2]$  does not lead to even lower peroxy radical concentrations. Similar but less pronounced effect can be seen in Figure 4.3 for total peroxy radical concentrations.

Another sink for the peroxy radical that increases in strength with increasing oxidation rates is the formation of dimers. In Figure 4.1 it was shown that dimer formation increases stronger than monomer formation at low  $[OH]$ /low oxidation rate, which is consistent with the results shown here, namely a decrease in peroxy radical concentrations despite of increasing source strengths.

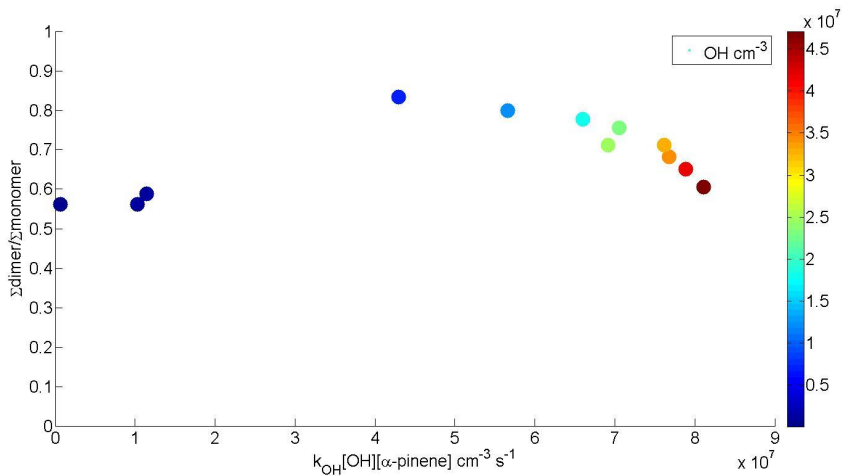


Figure 4.8 Ratio of total dimer to total monomer production as a function of oxidation rate. The Colour indicates the [OH] concentration during measurements. The three points at oxidation rates around  $1 \text{ cm}^3 \text{ s}^{-1}$  or lower were measured at very low [OH], and thus were likely dominated by ozonolysis. It can be seen that in the ozonolysis dominated system monomer production is proportionally higher than dimer production. Quickly after introducing OH into the system, the relative contribution from monomers decreases, and at  $k_{\text{OH}}[\text{OH}][\text{VOC}] 4 \cdot 10^7 \text{ cm}^{-3} \text{ s}^{-1}$  the relation is 0.9. After this the contribution from dimers lessens slightly, but remains higher than during ozonolysis. The comparison of separate monomer and dimer production rates as function of  $k_{\text{OH}}[\text{OH}][\alpha\text{-pinene}]$  (oxidation rate) is shown in Figure 4.1.

To further test the role of  $\text{HO}_2$  in HOM formation, Figure 4.8 shows how the ratio between total dimer and total monomer production changes with changing  $k_{\text{OH}}[\text{OH}][\alpha\text{-pinene}]$ . At low [OH] when ozonolysis is the main oxidant, the ratio of dimer signal intensity over monomer signal intensity is about 0.6. Reaching a state where OH reactions dominate ( $[\text{OH}] \sim 1\text{-}1.5 \cdot 10^7 \text{ cm}^{-3}$ ), the ratio increases to somewhat above 0.8. This means that more dimers are produced when compared to the same monomer concentrations than in case of ozonolysis. With further increasing [OH] the dimer contribution to total HOM formation decreases slightly. This change in ratio is a good indicator that at high  $\text{HO}_2$  concentrations the end product formation shifts from dimer formation towards hydroperoxide formation.

The following sections present estimations of the yields and actual HOM concentrations reached in the experiments.

## 4.2. Yield estimation from photochemical HOM production from $\alpha$ -pinene

To estimate the absolute concentrations measured with the CIMS, Figure 4.9 shows an example plot of measured HOM monomer concentrations which has been calibrated using the calibration factor introduced in Chapter 2.2.2. Due to the high calibration factor determined using the calibration set-up, another estimation of the HOM concentration is presented using the more conservative calibration factor reported by Ehn et al. (2014).

As can be seen, a higher oxidation rate greatly increases the HOM formation where the concentration of HOM is up to five-fold compared to very low OH concentrations. There is also a clear difference in the estimated concentrations. Using the calibration factor from the calibration set-up, the achieved concentrations (green circles) are unrealistically high comparing to the literature (Ehn et al., 2014). Even if assuming an order of magnitude error (see Chapter 2.2.2.) the concentrations are still high.

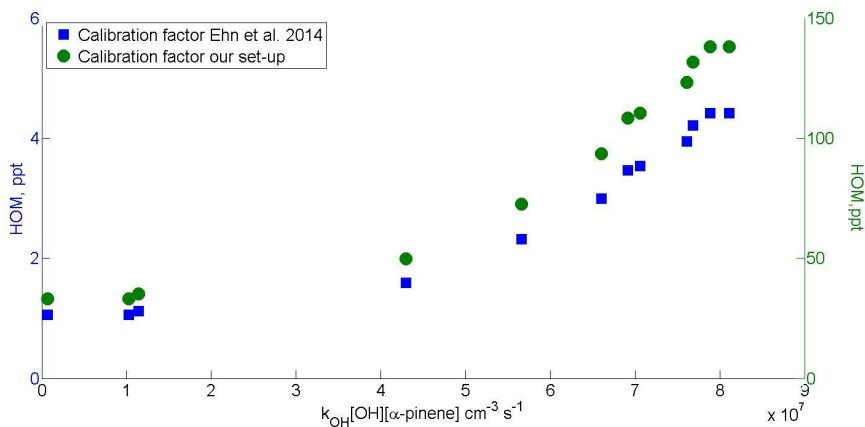


Figure 4.9 Estimation of HOM formation concentrations at different oxidation rates, using two different calibration factors (one from our set-up, the other from the literature (Ehn et al., 2014)).

Another way to estimate the photochemical HOM yield is to use the reported yield from ozonolysis as a baseline and do a relative comparison.

Ehn et al. (2014) estimated the (molecular) yield of HOMs produced by  $\alpha$ -pinene ozonolysis to be  $7 \pm 3.5\%$  and the yield of photochemical HOM production to be  $\sim 1\%$  at low  $[OH]$ . As shown above, the HOMs formed by photooxidation are not linearly related to the  $\alpha$ -pinene oxidation, and although there is a linear subrange at higher  $[OH]$ , the yield will not be a single number.

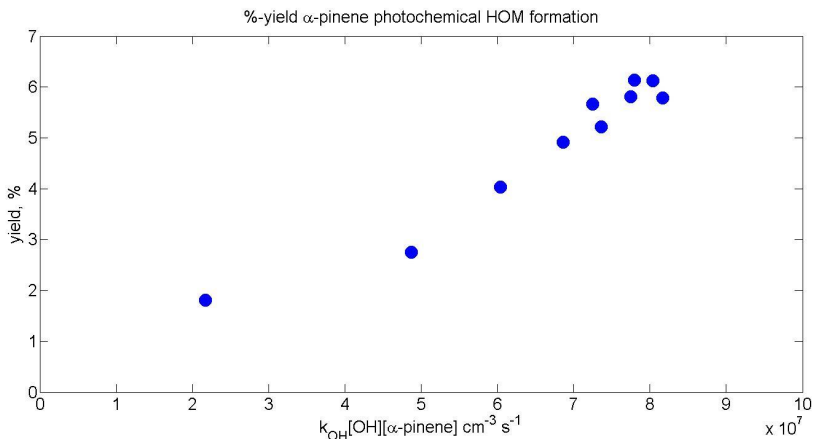


Figure 4.10 Estimated yields of photochemical HOM formation from  $\alpha$ -pinene. As OH dependence of the HOM formation is not linear, several values for the yield are calculated, depending on the oxidation rate.

As it is not proven so far that only HOMs contribute to particle mass formation during the measurements, using mass formation yields as base to determine the yield of HOMs was refrained. The yield of HOM formation from  $\alpha$ -pinene photooxidation was therefore calculated using the 7 % given by Ehn et al. (2014) for ozonolysis as baseline.

For this calculation data from an experiment where  $\alpha$ -pinene addition to the chamber was kept constant and OH concentration was varied by variations of  $J(O^1D)$  was used. During the respective measurement series two measurements were made without photochemical OH production. Assuming that the consumption of  $\alpha$ -pinene was mainly due to ozonolysis (OH formed from ozonolysis was neglected) the signal intensities of all HOMs (monomers and dimers) were added and divided by the consumption of  $\alpha$ -pinene. The resulting number was assumed to be the 7 % given by Ehn et al. (2014) and was used as "calibration" to set the HOM yield during ozonolysis in these results to 7 %.

The sum of signal intensities for all HOMs produced from photooxidation was obtained by subtracting the average of this signal from ozonolysis from the measured data. The resulting number was divided by the consumption of  $\alpha$ -pinene as measured during the experiment again, after subtracting the ozone based consumption. Using the aforementioned calibration factor yields between 1.8 and 7 % were estimated (Figure 4.10).

This approximation neglects the systematic changes of ozone during the periods with different  $J(O^1D)$ . This slightly changes the consumption of  $\alpha$ -pinene by ozone reactions. The estimated yields may therefore be somewhat too high. On the other hand, the signal intensity from ozonolysis born HOMs would be lower, too. As the signal intensity for the highest ozone concentration was subtracted as

background, the yields given here may be somewhat too low. Both systematic errors cancel out, but only if the yield of HOM formation from ozonolysis would be independent of the oxidation rate. As there is no information about the dependence of HOM formation from ozonolysis on the oxidation rate the error can only be estimated.

However, this estimation is based on the assumption of a 7% yield from ozonolysis. The error of this number is quite high ( $\pm 3.5$  percentage points) and is the dominant error source for the estimation.

### 4.3. $\beta$ -pinene: photochemical HOM production from exocyclic double bonds

The main focus so far has been on  $\alpha$ -pinene, as  $\alpha$ -pinene is a major emission from biogenic sources, especially in boreal regions (Guenther et al., 2012). Similar experiments were conducted with  $\beta$ -pinene, another isomer of pinene. Figure 4.11 presents results for  $\beta$ -pinene photochemical HOM formation. When comparing to  $\alpha$ -pinene a few differences were observed. One is the clearly smaller background during ozonolysis reactions ( $< 0.5 \cdot 10^{-3}$  counts/s). This is caused by a lower rate constant for  $\beta$ -pinene ozonolysis compared to that of  $\alpha$ -pinene and in particular by the exocyclic double bond of  $\beta$ -pinene which makes HOM formation from  $\beta$ -pinene ozonolysis inefficient. Also, the [OH] range used for  $\beta$ -pinene experiments is slightly higher ( $0.5\text{-}7.0 \cdot 10^7 \text{ cm}^{-3}$ ) than for  $\alpha$ -pinene experiments ( $0.5\text{-}5.0 \cdot 10^7 \text{ cm}^{-3}$ ). However, the oxidation rate is an order of magnitude higher than in the case of  $\alpha$ -pinene.

$\beta$ -pinene dimers reach saturation at low  $k_{\text{OH}}[\text{OH}][\beta\text{-pinene}]$  values and do not seem to exhibit the same increase as from  $\alpha$ -pinene produced dimers. However, here it is important to compare the [OH] during the experiments. For  $\alpha$ -pinene, until HOM dimers reach saturation, the curve and formation intensity are similar to those of monomers up to the midlevel [OH] limit of the experiment ( $[\text{OH}] \sim 2\text{-}2.5 \cdot 10^7 \text{ cm}^{-3}$ ). When comparing the  $\beta$ -pinene HOM dimer formation, it can be seen that the dimer saturation occurs at similar [OH] levels ( $1.5\text{-}2.5 \cdot 10^7 \text{ cm}^{-3}$ ). The higher [OH] or higher oxidation rate does not lead to increasing dimer formation, similar to the case of  $\alpha$ -pinene but perhaps clearer due to slightly higher upper range of the [OH] used.

At monomer range the HOM increase is nearly 8-fold (from  $0.5 \cdot 10^{-3}$  to  $4.0 \cdot 10^{-3}$  counts/s) higher than the corresponding increase seen with  $\alpha$ -pinene. The shape is also quite different. The non-linearity of the increase of HOM concentrations with increasing [OH] is much more pronounced for  $\beta$ -pinene. One possible reason for this may be the efficient HOM formation from  $\alpha$ -pinene ozonolysis. In both experiments [OH] was varied by varying  $J(\text{O}^1\text{D})$ . At the same ozone inflow into the chamber higher  $J(\text{O}^1\text{D})$  lowers the ozone concentration in the chamber. Hence higher [OH] is paralleled by lower  $[\text{O}_3]$ . While this has no impacts on the shape obtained for  $\beta$ -pinene, this effect lowers the curvature for  $\alpha$ -pinene.

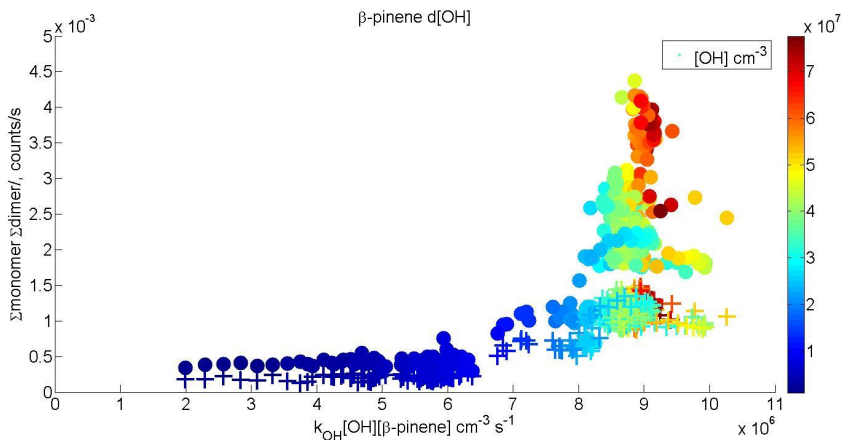


Figure 4.11 Total monomer (circles) and dimer (crosses) concentration from  $\beta$ -pinene photooxidation as a function of  $\beta$ -pinene oxidation rate. Colour code indicates [OH]. As the reaction rate of  $\beta$ -pinene and ozone in the chamber is slow, the background at low [OH] is smaller when compared to  $\alpha$ -pinene ( $0.5 \cdot 10^{-3}$  counts/s vs  $1.5 \cdot 10^{-3}$  counts/s, respectively). The monomer concentration increases nearly exponentially as a function of  $k_{OH}[OH][\beta\text{-pinene}]$ , while the dimer concentration reaches saturation at [OH] of  $1.5 - 2.5 \cdot 10^{-3} \text{ cm}^{-3}$ . The [OH] range used in this experiment was slightly wider than in the  $\alpha$ -pinene experiments. In general the behaviour is similar with  $\alpha$ -pinene and  $\beta$ -pinene; the more reactions of OH and VOC occur the higher the HOM production is, in both monomer and dimer range.

Figure 4.12 presents the change of dimer/ monomer ratio in  $\beta$ -pinene HOM formation at high oxidation rates/[OH] only. As  $\beta$ -pinene HOM formation under ozonolysis is low, signal intensities at low [OH] are also low. As low signal intensities bare the risk of too high error margins, only higher [OH] conditions are considered. In general a very similar behaviour of this ratio can be observed as for  $\alpha$ -pinene. Increasing [OH] lowers the ratio, and also in the case of  $\beta$ -pinene the behaviour is explainable by  $\text{HO}_2$  production during photooxidation and further reactions of dimers with OH.

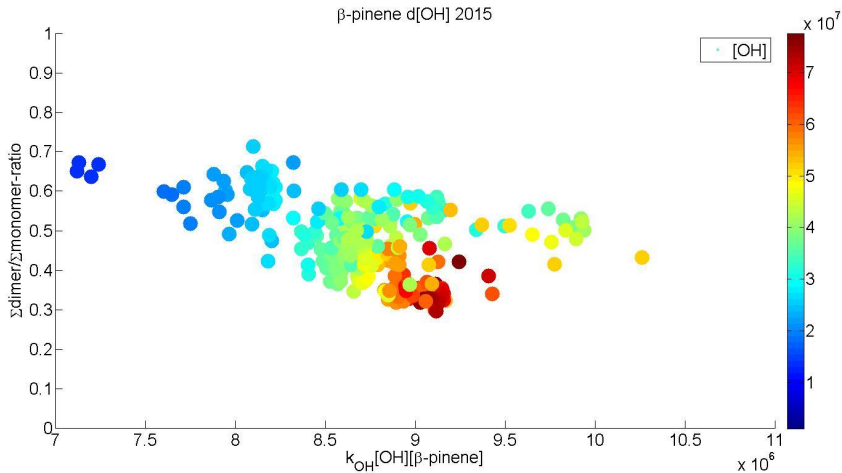


Figure 4.12 Ratio HOM dimer to HOM monomer from  $\beta$ -pinene photooxidation as a function of  $\beta$ -pinene destruction rate under high [OH]. Ozonolysis dominated range has been excluded. The dimer contribution is largest at the same range where the dimer formation reaches saturation, after which the near exponential increase of monomer concentration leads to a rapid decrease in the ratio.

#### 4.4. Concluding remarks on photochemical HOM production

HOM production shows non-linear dependence on OH concentration on both monomer and dimer ranges. It is unclear whether this non-linearity is relevant in practice. However, it is clear that increasing OH concentration increases total HOM formation as well as the yield of HOM formation. The increase of monomer concentration is mainly due to the increase of hydroperoxide (+alcohol) concentrations. But as Figure 4.1 shows, dimer production increases as well. The reduction of the concentration of HOM peroxy radicals due to reactions with  $\text{HO}_2$  was not strong enough to diminish dimer formation absolutely because of the stronger source strengths of peroxy radicals. Only the relative importance of dimer formation compared to monomer formation was affected by hydroperoxide formation. Also no systematic change in peroxy radical concentrations with varying OH concentration was found, in regard to clear systematic increases or decreases of all individual peroxy radicals. Probably the increasing source strength was cancelled out by the increasing sink strengths due to hydroperoxide and dimer formation. However, the effects observed when varying OH concentration could be explained using basics of peroxy radical chemistry. The behaviour observed during these experiments furthermore confirms the assignment of HOMs as hydroperoxides or ketones.

The increase in HOM production with higher OH concentration is an important factor when investigating the effect of  $\text{NO}_x$  in HOM formation in Chapter 5.

## Chapter 5 Chemical transformation of HOMs

### 5.1. Photochemistry of $\alpha$ -pinene in the presence of $\text{NO}_x$

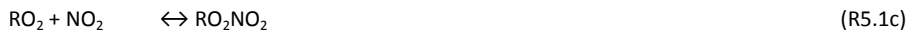
The dominant pathway of OH initiated  $\alpha$ -pinene oxidation (~90 %) is the addition of the OH radical to the double bond. This leads to the opening of the double bond with OH attached to one end. The other end forms the alkyl radical at which  $\text{O}_2$  is added and a primary peroxy radical is formed.

The further fate of this peroxy radical depends on the abundance of  $\text{NO}_x$  ( $\text{NO}_x = \text{NO} + \text{NO}_2$ ).  $\text{NO}_x$  adds complexity to chemical reaction system and product distribution. As reminder, alcohols, carbonyls, hydroperoxides, and alkoxy radicals are formed in absence of  $\text{NO}_x$ . In the presence of  $\text{NO}_x$ , the peroxy radical can react with NO:



Reaction R5.1a leads to the formation of an organic nitrate, reaction R5.1b to the formation of an alkoxy radical and  $\text{NO}_2$ .

It is important to realize that if the peroxy radical contains an acyl group ( $-\text{C}(=\text{O})\text{OO}\cdot$ ) it reacts fast with  $\text{NO}_2$  forming PAN like organic nitrates.



As side remark, in particular at higher temperatures these organic nitrates are not stable and decompose thermally, which in the atmosphere affect secondary radical formation. Note, in JPAC the experiments were performed at 15 °C and PANs will be relatively stable.

A special case of Reaction R5.1b is the reaction of NO with  $\text{HO}_2$ .



Reaction R5.1d is the basis of OH recycling in a photochemical system. However, increasing  $[\text{NO}_x]$  to high amounts can also decrease  $[\text{OH}]$  because the reaction R5.1e is a strong sink for OH:



According to reaction R5.1d and R5.1e,  $\text{NO}_x$  addition to JPAC will regulate also here the OH concentration. In the following these basic reaction pathways will be used to explain the changes observed when  $\text{NO}_x$  is added to  $\alpha$ -pinene photooxidation system. As NO can lead to increase of OH recycling in the system, depending on the  $\text{NO}_x$  concentration and NO/ $\text{NO}_2$  ratio, it is important to distinguish between the effect of  $\text{NO}_x$  addition and increased OH concentration. The previous chapter covered how increasing  $[\text{OH}]$  increases total HOM formation, and this will be used here to explain the behaviour of HOM formation at the presence of  $\text{NO}_x$ .

Concentrating on few example peaks, the effect of NO<sub>x</sub> on individual compound formation is endeavoured to be explained. These findings are discussed using the example of the peaks at 247 Th (peroxy radical C<sub>10</sub>H<sub>15</sub>O<sub>7</sub><sup>·</sup>), 277 Th (C<sub>10</sub>H<sub>15</sub>NO<sub>8</sub>, organic nitrate from C<sub>10</sub>H<sub>15</sub>O<sub>7</sub><sup>·</sup>), 248 Th (C<sub>10</sub>H<sub>16</sub>O<sub>7</sub>, hydroperoxide from C<sub>10</sub>H<sub>15</sub>O<sub>7</sub><sup>·</sup>), 263 Th (C<sub>10</sub>H<sub>15</sub>O<sub>8</sub><sup>·</sup>, peroxy radical), 264 Th (C<sub>10</sub>H<sub>16</sub>O<sub>8</sub>, hydroperoxide from C<sub>10</sub>H<sub>15</sub>O<sub>8</sub><sup>·</sup>), 293 Th (C<sub>10</sub>H<sub>15</sub>NO<sub>9</sub>, organic nitrate from C<sub>10</sub>H<sub>15</sub>O<sub>8</sub><sup>·</sup>) and 246 Th (C<sub>10</sub>H<sub>14</sub>O<sub>8</sub>, ketone from C<sub>10</sub>H<sub>15</sub>O<sub>8</sub><sup>·</sup>). Ketone formed from C<sub>10</sub>H<sub>15</sub>O<sub>7</sub><sup>·</sup> is weakly detected by the CIMS, and will be left outside of this analysis.

Table 5.1. Molecular composition and detection mass in unit mass for two different peroxy radical series C<sub>10</sub>H<sub>15</sub>O<sub>7</sub><sup>·</sup> and C<sub>10</sub>H<sub>15</sub>O<sub>8</sub><sup>·</sup> with termination products. Nitrate peaks *m+30* and *m+46* are not possible to distinguish with the CIMS due to same molecular mass, but as the formation pathway is different they are shown separated here.

Peroxy radical <i>m</i>	Mass [Th]	Hydroperoxide <i>m+1</i>	Mass [Th]	Organic nitrate <i>m+30</i>	Mass [Th]	PAN-like nitrate <i>m+46</i>	Mass [Th]	Ketone <i>m-17</i>	Mass [Th]
C <sub>10</sub> H <sub>15</sub> O <sub>7</sub> <sup>·</sup>	247	C <sub>10</sub> H <sub>16</sub> O <sub>7</sub>	248	C <sub>10</sub> H <sub>15</sub> NO <sub>8</sub>	277	C <sub>10</sub> H <sub>15</sub> NO <sub>9</sub>	293	C <sub>10</sub> H <sub>14</sub> O <sub>6</sub>	230
C <sub>10</sub> H <sub>15</sub> O <sub>8</sub> <sup>·</sup>	263	C <sub>10</sub> H <sub>16</sub> O <sub>8</sub>	264	C <sub>10</sub> H <sub>15</sub> NO <sub>9</sub>	293	C <sub>10</sub> H <sub>15</sub> NO <sub>10</sub>	309	C <sub>10</sub> H <sub>14</sub> O <sub>7</sub>	246

In Chapter 3 was given an example of a detailed  $\alpha$ -pinene photooxidation HOM spectrum (Figure 3.1). Figure 5.1 shows how NO<sub>x</sub> addition changes the end product formation pattern compared to  $\alpha$ -pinene photooxidation. An example of a peroxy radical end product series can be seen at 247 Th (peroxy radical C<sub>10</sub>H<sub>15</sub>O<sub>7</sub><sup>·</sup>, *m*), the hydroperoxide at 248 Th (C<sub>10</sub>H<sub>16</sub>O<sub>7</sub>, *m+1*, includes alcohol from C<sub>10</sub>H<sub>15</sub>O<sub>8</sub><sup>·</sup>) and organic nitrate at 277 Th (C<sub>10</sub>H<sub>15</sub>NO<sub>8</sub>, *m+30*, Table 5.1.). The ketone (*m-17*, at 230 Th C<sub>10</sub>H<sub>14</sub>O<sub>6</sub>) for this series is not well detected with this instrument. When NO<sub>x</sub> is added to the system, the hydroperoxide peak at 248 Th decreases by 30 % (0.004 to 0.003 counts/s), while corresponding peroxy radical at 247 Th remains almost same (+4%). Ratio 247/248 changes from 0.11 to 0.17. The nitrate C<sub>10</sub>H<sub>15</sub>NO<sub>8</sub> from peroxy radical C<sub>10</sub>H<sub>15</sub>O<sub>7</sub><sup>·</sup> increases more than 20 fold (from 1.1 · 10<sup>-4</sup> to 2.4 · 10<sup>-3</sup> counts/s).

The next peroxy radical produced, C<sub>10</sub>H<sub>15</sub>O<sub>8</sub><sup>·</sup> (at 263 Th) does not decrease, but instead almost triples in intensity (2.4 · 10<sup>-4</sup> to 6.9 · 10<sup>-4</sup> counts/s), while the corresponding hydroperoxide (C<sub>10</sub>H<sub>16</sub>O<sub>8</sub>, at 264 Th) remains steady (+1%). The corresponding nitrate C<sub>10</sub>H<sub>15</sub>NO<sub>9</sub> (at 293 Th) shows similar high increase than C<sub>10</sub>H<sub>15</sub>NO<sub>8</sub><sup>·</sup> (by an order of magnitude, from 5.0 · 10<sup>-5</sup> to 6.7 · 10<sup>-4</sup> counts/s). C<sub>10</sub>H<sub>15</sub>NO<sub>9</sub> is also an end product of peroxy radical C<sub>10</sub>H<sub>15</sub>O<sub>7</sub><sup>·</sup> +NO<sub>2</sub> (R5.1c; *m+46*). Later a hypothesis is offered to explain this difference in peroxy radical behaviour.

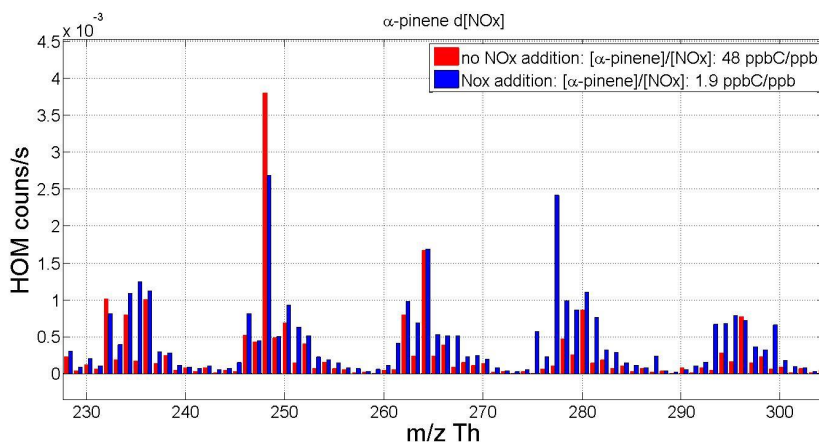


Figure 5.1 Comparison spectra of  $\alpha$ -pinene HOM formation pattern under very low  $\text{NO}_x$  (red) and high  $\text{NO}_x$  conditions (blue). Experimental conditions were  $[\alpha\text{-pinene}] = 1.45$  ppb in the low  $\text{NO}_x$  experiment and 1.7 ppb in the high  $\text{NO}_x$  experiment, respectively. Measured  $[\text{NO}_x]$  during low  $\text{NO}_x$  experiment was 0.3 ppb, which gives a ratio  $[\alpha\text{-pinene}]/[\text{NO}_x] = 48$  ppbC/ppb, and at high  $\text{NO}_x$   $[\text{NO}_x] = 8.7$  ppb and 1.9 ppbC/ppb, respectively.

As described in Chapter 1, photooxidation of  $\alpha$ -pinene leads to many peroxy radicals that differ by one O atom. In principle, all these peroxy radicals can form organic nitrates. Knowing the mass of the peroxy radical, it is straightforward to calculate the masses of the organic nitrates from these peroxy radicals. In all cases increases were found when adding  $\text{NO}_x$  resulting in quite strong peaks at the masses where they were expected from the masses of corresponding peroxy radicals. Based on this, and on the mass defect of these compounds, it is possible to conclude that these strong peaks are organic nitrates. The behaviour of organic nitrates also confirms the identification of peroxy radicals.

As an example, the increase of the organic nitrate  $\text{C}_{10}\text{H}_{15}\text{NO}_8$  (277 Th) will be discussed in more detail. As expected,  $\text{NO}_x$  addition induced the formation of organic nitrates. Accordingly, the signal intensity of the peak at 277 Th increased strongly. As organic nitrates can also be formed from reaction R5.1c it is also possible that the increase of peak intensity is due to organic nitrate formation from  $\text{NO}_2$  and the peroxy radical  $\text{C}_{10}\text{H}_{15}\text{O}_6^{\cdot}$  (at 231 Th) as precursor peroxy radical. Correspondingly, the organic nitrate  $\text{C}_{10}\text{H}_{15}\text{NO}_9$  (at 293 Th) can also be formed from  $\text{C}_{10}\text{H}_{15}\text{O}_7^{\cdot}$  (peak at 247 Th) in reaction R5.1c.

However, the effects of the two pathways shown in Reactions R5.1a and R5.1c are indistinguishable. As the CIMS only acquires molecular formulas of the HOMs and no structural information, it is not possible to separate  $\text{C}_{10}\text{H}_{15}\text{NO}_8$  formed from  $\text{C}_{10}\text{H}_{15}\text{O}_7^{\cdot} + \text{NO}$  (organic nitrate, R5.1a), or from  $\text{C}_{10}\text{H}_{15}\text{O}_6^{\cdot} + \text{NO}_2$  (PAN-like nitrate, R5.1c) as long as  $\text{C}_{10}\text{H}_{15}\text{O}_6^{\cdot}$  is an acyl radical. The relative contribution from these two pathways in the chamber will be discussed next in more detail.

### 5.1.1. Formation of organic nitrates and PAN-like nitrates

So far a distinction between the two organic nitrate pathways covered in this chapter has not made. As mentioned earlier it is not possible to distinguish between organic HOM nitrates ( $m+30$ ) and PAN-like nitrates ( $m+46$ ; R5.1a or R5.1c, respectively) from the direct data gathered by the instrument. There is however a method that can be used to derive more information about the formation pathway of these two nitrate compounds with same molecular formula:

In the chamber NO is produced by photolysing NO<sub>2</sub>. So, in order to remove the  $m+30$  organic nitrate formation pathway, the NO<sub>2</sub> to NO conversion in the chamber was stopped by switching off the UV-A light. Remaining NO reacted within minutes with O<sub>3</sub>, and the system became NO<sub>2</sub> dominated. Lack of NO in the system would inhibit R5.1a.

Due to the low  $J(\text{NO}_2)$  the ratio of  $[\text{NO}]/[\text{NO}_2]$  is quite low in the chamber. R5.1c is not as much affected as less than 20% of the NO<sub>2</sub> is photolysed. Figure 5.2 shows a time series from this experiment, with termination product groups separated to observe the general behaviour. As can be seen, when NO<sub>2</sub> to NO conversion was ended, HOM nitrate concentration decreased by less than 40% compared to NO+NO<sub>2</sub> system. During that stage the dominant nitrate production must go via NO<sub>2</sub> as there is very little NO left to react. This would suggest that at the temperature of 16 °C and at a  $J(\text{NO}_2)$  of  $4 \cdot 10^{-3} \text{ s}^{-1}$  about 60% of the nitrate-HOM production in the chamber goes via NO<sub>2</sub>, i.e. PAN-like nitrates. Hydroperoxide formation increases slightly because  $[\text{HO}_2]$  increases due to the absence of NO, although  $[\text{OH}]$  is somewhat lower due to the absence of NO and the slightly higher NO<sub>2</sub> concentration.

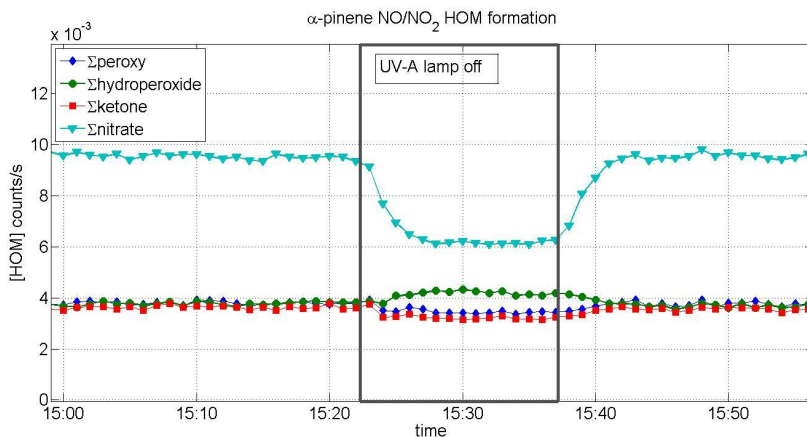


Figure 5.2 Time series showing total peroxy radical, hydroperoxide, ketone, and nitrate concentrations during NO<sub>x</sub> addition experiment. During first part of the experiment, UV-A lamps were on, to photolyse part of the NO<sub>2</sub> into NO. When these lamps were turned off, NO<sub>2</sub> to NO conversion was disrupted and  $[\text{NO}]/[\text{NO}_2]$  ratio decreased. As can be seen, total HOM nitrate production decreases about 40% and then reaches a new steady state. This would suggest that over 60% of formed nitrate is due NO<sub>2</sub> reactions (PAN-like nitrate).

However, as this method of separation is not practical to use in all experiments, in the analysis the two different pathways are not separated.

### 5.1.2. The effect of $\text{NO}_x$ on peroxy radical chemistry

As was shown in Chapter 4, hydroperoxide formation is the main monomer end product pathway. In order to better compare the effect  $\text{NO}_x$  addition has on the end product pattern, the overlap of hydroperoxide and alcohol peaks should be addressed.

As the peak at 248 Th is the sum of a hydroperoxide and an alcohol from a different progression, it cannot be directly concluded which of them is suppressed in concentration by the  $\text{NO}_x$  addition. In Chapter 4 it was shown how a ketone can be used as proxy for an alcohol, and the same method will be used here. Figure 5.3 shows the ratio of total hydroperoxides to total ketones, which is high at low  $[\text{NO}_x]$  ( $\sim 0.3$  ppb) and decreases non-linearly until at  $\sim 20$  ppb  $[\text{NO}_x]$  the ratio is 1. It can be assumed that at high  $[\text{NO}_x]$ , the signal dominantly consist of alcohol. From this can be concluded that changes at  $[\text{NO}_x] < 20$  ppb come from changes in hydroperoxide concentrations.

The relative abundance of hydroperoxides can be diminished by reactions of  $\text{NO}$  with  $\text{HO}_2$ . Removing one of the reactants forming the hydroperoxides their formation rate should be lowered. This was observed.

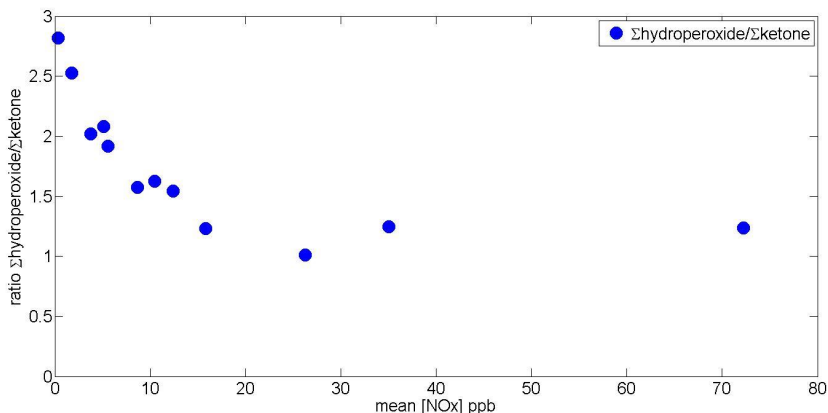


Figure 5.3 Ratio of total hydroperoxide signal to total ketone signal as a function of  $[\text{NO}_x]$ . Ketone is here used as a proxy for alcohol, to decouple the changes occurring in overlapping hydroperoxide and alcohol peaks. With increasing  $[\text{NO}_x]$  the hydroperoxide pathway becomes less prominent, and at  $[\text{NO}_x] \sim 20$  ppb the ratio reaches 1. This is similar as determined under ozonolysis with low  $\text{HO}_2$ , and it can be assumed that most of the remaining signal is now due to alcohols formed in reaction R1.3e.

A contrast to the clear change in the relative abundance of hydroperoxides compared to ketones (Figure 5.3) is the only moderate decrease of the signal intensity of all ketones, alcohols, and hydroperoxides. Addition of  $\text{NO}_x$  should diminish the formation of all  $\text{HOM-RO}_2 + \text{RO}_2/\text{HO}_2$  reaction products. This was not observed. In connection with this is the behaviour of peroxy radicals with increasing  $\text{NO}_x$ . As can be seen in Figure 5.1, the behaviour of peroxy radicals (example peaks 247 and 263 Th) is different. As mentioned, the signal intensity of  $\text{C}_{10}\text{H}_{15}\text{O}_7^-$  (247 Th) increases slightly and that of  $\text{C}_{10}\text{H}_{15}\text{O}_8^-$  (263 Th) increases 3-fold. While the slight increase in the concentration of peroxy radical  $\text{C}_{10}\text{H}_{15}\text{O}_7^-$  (247 Th) might be explainable by a  $\text{NO}_x$  induced increase of  $[\text{OH}]$  (from  $4.6 \cdot 10^7$  to  $6.4 \cdot 10^7$  molecules/ $\text{cm}^3$ ), the strong increase in the concentration of  $\text{C}_{10}\text{H}_{15}\text{O}_8^-$  cannot (see Chapter 3, sequential OH reactions are not an important source for HOMs). A possible explanation for this increase is the formation of alkoxy radicals following reactions R5.1a and R5.1b.

When concentrating on an individual  $\text{HOM-RO}_2$  with concentration  $[\text{RO}_2]$ , the production rate for  $\text{RONO}_2$  can be expressed by

$$P(\text{RONO}_2) = k^N \cdot [\text{NO}_x] \cdot \gamma(\text{RONO}_2) \cdot [\text{RO}_2]$$

with  $k^N$  being an average rate constant for organic nitrate formation and  $\gamma(\text{RONO}_2)$  the yield of organic nitrate formation. The production rate for other termination products T:

$$P(\text{T}) = [\text{RO}_2] \cdot \sum [\text{R}'\text{O}_2]^i \cdot k^{\text{R},i} \cdot \gamma(\text{T})^i$$

with  $\sum [\text{R}'\text{O}_2]^i$  being the sum of all peroxy radicals,  $k^{\text{R},i}$  the rate constant for the respective reaction, and  $\gamma(\text{T})^i$  the yield of termination products in these reactions. The ratio of the production rates is thus

$$\frac{P(\text{RONO}_2)}{P(\text{T})} = \frac{k^N \cdot [\text{NO}_x] \cdot \gamma(\text{RONO}_2)}{\sum [\text{R}'\text{O}_2]^i \cdot k^{\text{R},i} \cdot \gamma(\text{T})^i}$$

From the experiments described in Chapter 6 it is known that HOMs are very efficiently lost to chamber walls and particles regardless whether the HOM is an organic nitrate or other termination product. These losses are the dominant loss terms, and they are a good approximation independent of the production rates of HOM. From this it can be deduced that the concentration of a given HOM is proportional to its production rate. The production rates therefore reflect concentrations and the signal intensities for the individual HOMs and the  $\text{NO}_x$  dependency of HOM concentrations can be deduced from:

$$\frac{\partial \left( \frac{P(\text{RONO}_2)}{P(\text{T})} \right)}{\partial \text{NO}_x}$$

For this there is no analytical solution as  $\frac{\partial(P(\text{T}))}{\partial(\text{NO}_x)}$  is unknown.

For first approximation can be set:

$$\frac{\partial(P(\text{T}))}{\partial(\text{NO}_x)} = 0$$

Which can be solved for

$$\frac{\partial\left(\frac{P(\text{RONO}_2)}{P(T)}\right)}{\partial \text{NO}_x} = k^N \cdot \gamma(\text{RONO}_2)$$

This would indicate linear increase as a function of  $[\text{NO}_x]$ .

However, the most probable scenario is that  $\frac{\partial(P(T))}{\partial \text{NO}_x} < 0$

At constant  $\text{RO}_2$  production rate increasing  $[\text{NO}_x]$  should lead to lower  $[\text{RO}_2]$  and lower  $\Sigma[\text{R}'\text{O}_2]$ , which in turn means that the increase is stronger than linear.

Independent of  $\frac{\partial(P(\text{RONO}_2))}{\partial \text{NO}_x}$  being linear or stronger than linear, it follows that at  $[\text{NO}_x] \gg \Sigma[\text{RO}_2]$ ,  $\Sigma[\text{T}] \ll [\text{RONO}_2]$ .

However, if plotting the ratio of organic nitrates to other termination products (sum of hydroperoxides and ketones) as a function of  $[\text{NO}_x]$ , the result gives saturation at  $[\text{NO}_x]$  above 30 ppb (Figure 5.4).

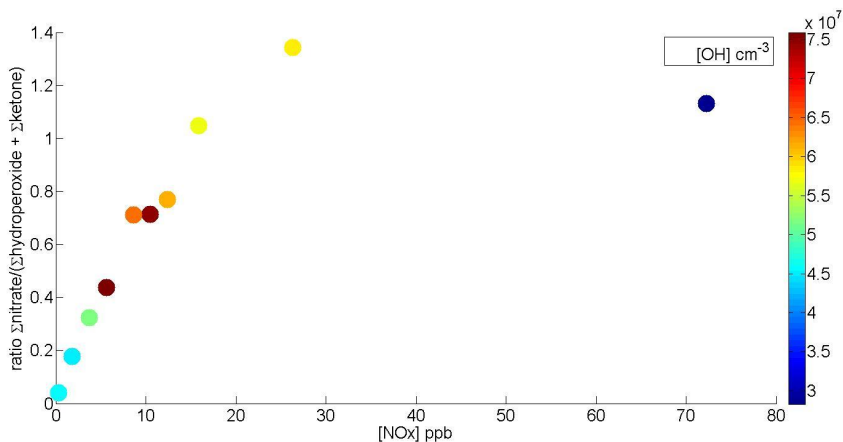


Figure 5.4 Ratio of the sum of all nitrate HOM to the sum of the other termination products (excluding peroxy radicals) as a function of  $[\text{NO}_x]$ .  $[\text{OH}]$  included in colour coding. Introducing  $\text{NO}_x$  into the system offers additional termination pathway to  $\text{RO}_2$ -radical leading to nitrate formation. Near-linear increase of ratio at  $[\text{NO}_x] < 30$  ppb is observable as is the saturation at  $[\text{NO}_x] > 30$  ppb ( $[\text{NO}] > 1$  ppb, data not shown). Saturation implies that above a certain  $\text{NO}_x$  concentration the ratio of organic nitrate formation over that of  $\text{RO}_2$ - $\text{RO}_2$  termination products stays constant. This contrasts the idea of reactions R5.1a and R5.1c being competitive to reactions R1.3e-R1.3h (see Introduction 1.3.). Using classical laws of photochemistry this saturation can only be explained if it is assumed that the alkoxy radicals formed in reaction R5.1b do not decompose but undergo H-shift with subsequent addition of  $\text{O}_2$  to form a new peroxy radical.

From the measurements it is evident that with increasing  $[NO_x]$ , the organic nitrate production rate ( $k^N \cdot [NO_x] \cdot \gamma(RONO_2) \cdot [RO_2]$ ) increases. If, as indicated by Figure 5.3, the ratio

$\frac{P(RONO_2)}{P(T)} = \frac{k^N \cdot [NO_x] \cdot \gamma(RONO_2)}{\sum [R^i O_2] \cdot k^{R,i} \cdot \gamma(T)^i}$  saturates, this must mean that both the nominator and the denominator of the equation change similarly i.e.  $\sum [R^i O_2] \cdot k^{R,i} \cdot \gamma(T)^i$  or  $[RO_2]$  increase with increasing  $[NO_x]$ . In other words, the production of  $RO_2$  increases with increasing  $[NO_x]$ . This is consistent to the finding that also the peroxy radical concentrations increase with increasing  $NO_x$  (see below Figure 5.7).

A possible explanation is the alkoxy-peroxy pathway (R5.1b). Peroxy radical formation from alkoxy radical undergoing internal H-shift and subsequent  $O_2$  addition is a known hypothesis (Vereecken & Peeters, 2010; Vereecken & Francisco 2012). This newly formed peroxy radical would then have one oxygen atom more than the “parent” peroxy radical.

This pathway fits with the data observed during  $NO_x$  addition and offers an additional oxidation mechanism that forms another peroxy radical. Peroxy radicals forming via alkoxy-peroxy pathway would also fit the observation that the high end of HOM monomer range expands towards higher masses (Figure 5.4).

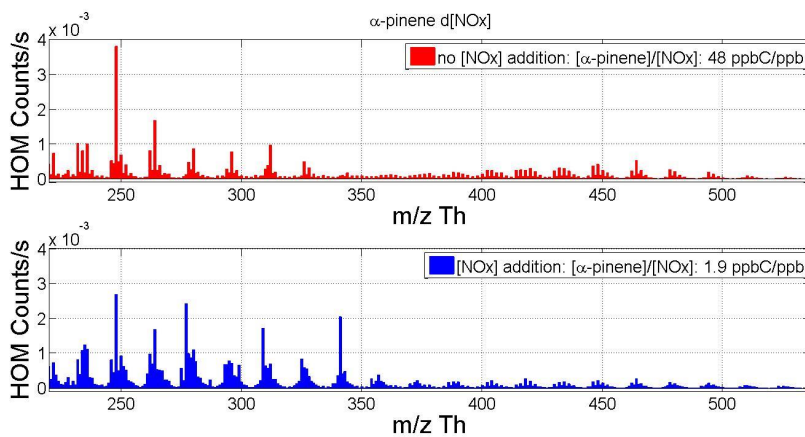


Figure 5.5 Comparison of HOM pattern for low  $NO_x$  (upper) and high  $NO_x$  ( $\sim 36$  ppb) conditions. Due to addition of  $NO_x$  and the subsequent OH recycling, the  $[OH]$  in the low  $NO_x$  case is  $4.6 \cdot 10^7 \text{ cm}^{-3}$ , and during  $NO_x$  addition  $4.9 \cdot 10^7 \text{ cm}^{-3}$ , similar enough to be unlikely to have major effect on the formation rates. The total [monomer] without  $NO_x$  is 0.02 counts/s, and total [dimer] 0.012 counts/s. With  $NO_x$  addition the total [monomer] increased to 0.04 counts/s, while the [dimers] decreased slightly, to 0.011 counts/s.

An overview on the general changes in HOM spectrum in the experiments shown in Figure 5.1 can be seen in Figure 5.5. The upper panel portraits a HOM spectrum from  $\alpha$ -pinene photooxidation without  $\text{NO}_x$  addition (red in Figure 5.1), and lower panel shows a HOM spectrum at the same mass range at high  $[\text{NO}_x]$  levels (blue in Figure 5.1). Without  $\text{NO}_x$  addition, the most prominent peaks seen in the monomer range are hydroperoxides, and a strong dimer production is evident (total monomer concentration when there is no  $\text{NO}_x$  addition is 0.02 counts/s and total dimer concentration 0.012 counts/s, which leads to apparent dimer/monomer ratio of approximately 0.6).

Some clear differences can be seen:

1. With  $\text{NO}_x$  the sum of signal intensities for all monomer range HOMs is higher than without  $\text{NO}_x$ . A fraction of this increase can be attributed to the higher  $[\text{OH}]$  in presence of  $\text{NO}_x$ . As the difference in  $[\text{OH}]$  is not that substantial the two-fold increase of HOM concentrations also hints to a more effective HOM formation via the alkoxy-peroxy pathway. Possibly the yield of alkoxy radical formation via reaction R5.1b is higher than that in R1.3e - R1.3h and in addition the H-shift in alkoxy radicals is extremely effective.
2. With  $\text{NO}_x$  the sum of signal intensities for the HOM dimers is lower than without  $\text{NO}_x$ . This can be attributed to the competition of dimer formation with organic nitrate formation. However, even at this high  $\text{NO}_x$  level, there are still dimers.
3. There is a general shift of monomer HOM to higher oxidation states (between  $\sim 240$  and  $\sim 370$  Th), i.e. to higher masses, with emphasis on nitrate production. This is due to organic nitrates having higher mass than corresponding hydroperoxides, as the organic nitrate or PAN-like nitrate formed is nearly 30/46 Th heavier than the corresponding hydroperoxide. But also the signal intensity for some highly oxidated HOM peroxy radicals increase with increasing  $\text{NO}_x$  and  $\text{RO}_2\text{-RO}_2$  termination products are still visible. But on top of that, there is a general shift towards higher oxidation states throughout the monomer range. In Chapter 3.5. it was shown that, when changing  $[\text{OH}]$  via increasing  $J(\text{O}^1\text{D})$ , there was no notiable shift towards higher masses in the formation products (Figures 3.5 and 3.6). It can therefore be concluded that the overall shift of the mass balance due to  $\text{NO}_x$  addition is in fact a result of adding  $\text{NO}_x$  into the system, not an effect of increased  $[\text{OH}]$ . As this systematic shift of oxidation status was not observed when varying  $[\text{OH}]$  this is attributed to the aforementioned peroxy-alkoxy pathway.

As long as  $J(\text{NO}_2) > 0$ , the two pathways of organic nitrate formation (R5.1a and R5.1c) are indistinguishable. This hinders obtaining quantitative information regarding rate constants for organic nitrate formation from HOM-peroxy radicals. The focus will therefore be on  $\text{NO}_x$  impacts on the total HOM formation. HOMs are separated in monomers and dimers because of the expected different behaviour. As in previous chapters, monomers are determined to be molecules between 240-370 Th and dimers 370-540 Th. As will be shown later, at high  $[\text{NO}_x]$  this will lead to small underestimation of monomers and small overestimation of dimers, but this has no large impact on general results.

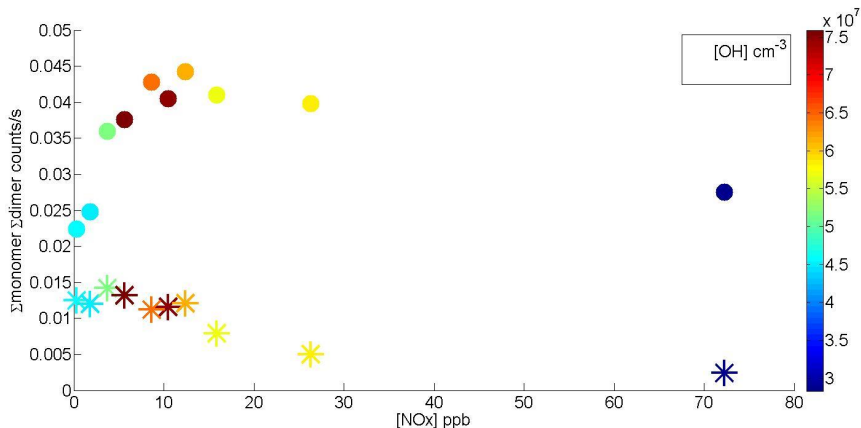


Figure 5.6 Total HOM monomer (240-370 Th, closed circles) and dimer (370-540 Th, stars) signal intensities as a function of  $[\text{NO}_x]$ . Colour code indicates  $[\text{OH}]$ . Monomer concentration increases linearly at  $[\text{NO}_x] < 10 - 15$  ppb, reaching maximum at  $[\text{NO}_x] \sim 15 - 20$  ppb, and decreases slowly at  $[\text{NO}_x] > 30$  ppb. Dimer production is less affected at low  $[\text{NO}_x]$ , remaining steady at  $[\text{NO}_x] < 15$  ppb, and then showing decreasing trend.

Sarrafzadeh et al. (2016) describe an increase in OH concentration when increasing  $[\text{NO}_x]$  during  $\beta$ -pinene and  $\alpha$ -pinene photooxidation. They furthermore claim that at moderate  $[\text{NO}_x]$  the changes in SOA yields were in general related to  $[\text{NO}_x]$  dependent OH recycling. As shown in Chapter 4, HOM formation has non-linear dependence on  $[\text{OH}]$ . The  $\text{NO}_x$  induced increase of  $[\text{OH}]$  can be expected to cause an increase of total HOM formation when  $\text{NO}_x$  is added to system, suggesting a possible connection between HOM formation and particle mass formation.

Figure 5.6 depicts total monomer and dimer formation from  $\alpha$ -pinene photooxidation as a function of  $[\text{NO}_x]$ . As can be seen monomer concentration nearly doubles at  $[\text{NO}_x]$  15 ppb. As  $[\text{OH}]$  increases from  $\sim 4.5 \cdot 10^7$  to  $7 \cdot 10^7$  molecules/ $\text{cm}^3$ , it is conceivable that the increase is due to increased  $[\text{OH}]$  following  $\text{NO}_x$  addition.

Dimer production decreases with increasing  $[\text{NO}_x]$ , excluding a small range at low  $\text{NO}_x$  ( $>10$  ppb) when the concentration remains steady. It is possible that increased peroxy radical formation caused by higher  $[\text{OH}]$  allows dimer concentration to remain constant, despite increased sink from NO and  $\text{NO}_2$  in monomer region. However the decrease in dimer region seen in Figure 5.5 is very pronounced and it is clear that at higher  $[\text{NO}_x]$  dimer concentration decreases strongly as a function of  $[\text{NO}_x]$ .

To get more detailed information on where the changes in HOM formation occur, results from separate compound classes are shown next.

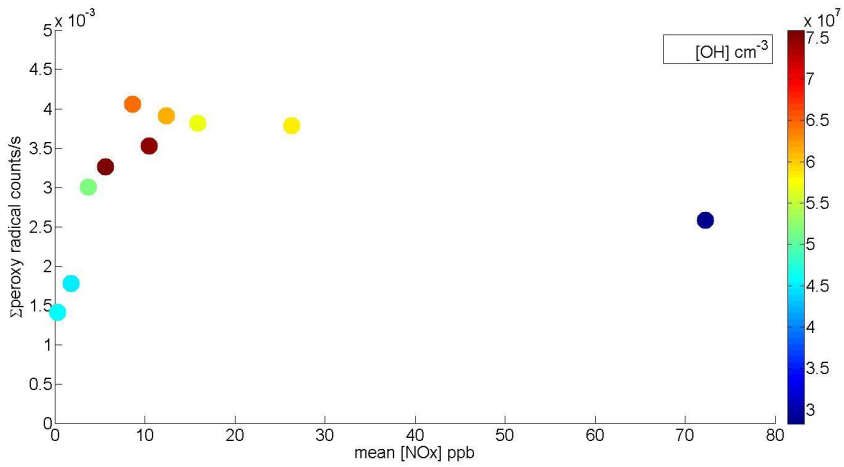


Figure 5.7 Total peroxy radical concentration as a function of [NO<sub>x</sub>]. At low [NO<sub>x</sub>] (< 10 ppb) peroxy radical concentration increases, reaches maximum at [NO<sub>x</sub>] 10 -30 ppb, and then slowly decreases. High peroxy radical concentration at high [NO<sub>x</sub>] (> 70 ppb) can be explained by an effective peroxy radical formation via the alkoxy-peroxy pathway.

Figure 5.7 shows the peroxy radical concentration as a function of [NO<sub>x</sub>]. Increase in [OH] leads to strong increase in peroxy radical concentration, with RO<sub>2</sub> concentration tripling from low [NO<sub>x</sub>] to [NO<sub>x</sub>] ~ 10 ppb. RO<sub>2</sub> concentration remains stable between [NO<sub>x</sub>] 10-30 ppb, and decreases slowly from there on. The general trend is increased peroxy radical concentration past increase in [OH], which can be explained by a combination of increased [OH] leading to higher peroxy radical formation, and increased [NO<sub>x</sub>] leading to peroxy radical formation via alkoxy-peroxy pathway.

Figure 5.8 shows the total HOM-organic nitrate production as a function of [NO<sub>x</sub>]. As can be seen, small increase of [NO<sub>x</sub>] in the system has large impact on the nitrate formation, and at NO<sub>x</sub> concentrations below 10 ppb the increase of organic nitrate production is close to linear, increasing by over an order of magnitude ( $4.0 \cdot 10^{-4}$  to  $8.0 \cdot 10^{-3}$  counts/s) . After this rapid increase in concentration, organic nitrate production begins to even out, and reaches saturation between 10-30 ppb NO<sub>x</sub>. At higher concentrations the production of organic nitrates decreases slowly.

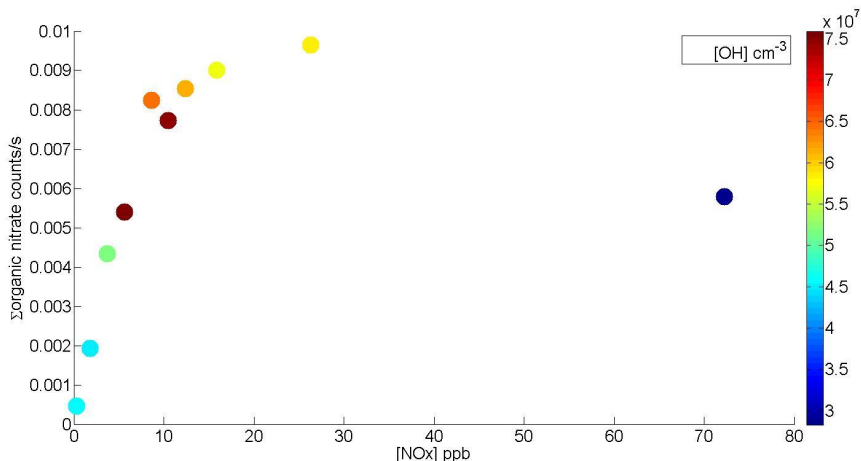


Figure 5.8 Total nitrate HOM production as a function of  $[\text{NO}_x]$ . Colour code indicates  $[\text{OH}]$ . Organic nitrate concentration increases rapidly in near-linear way until reaching 80-90% of maximum value at 10-15 ppb  $[\text{NO}_x]$ , after which the formation slows down significantly, but continues to increase until  $\sim 30$  ppb  $[\text{NO}_x]$ , and then slowly decreases, most likely due to decreasing peroxy radical formation caused by decreased  $[\text{OH}]$ .

As shown in Chapter 4, and as expected from classical peroxy radical chemistry in the presence of  $\text{HO}_2$ , hydroperoxides are the main monomer range termination product at low  $[\text{NO}_x]$  conditions. As addition of  $\text{NO}_x$  into a system leads to increase in  $\text{OH}$  concentration and destruction of  $\text{HO}_2$  (R5.1d), it was expected that decreasing  $[\text{HO}_2]$  would lead to lessening the role of hydroperoxide channel (R1.3e). Figure 5.9 shows the total hydroperoxide and ketone concentration dependence on  $[\text{NO}_x]$ . As can be seen, at very low  $[\text{NO}_x]$  ( $\sim 5$  ppb) there is nearly no effect on hydroperoxide production, possibly due to increased  $\text{OH}$  recycling increasing peroxy radical- and  $\text{HO}_2$  formation and balancing the  $\text{NO}_x$  induced  $\text{HO}_2$  loss, but the general trend of hydroperoxide production is a strong decrease with  $[\text{NO}_x] > 5$  ppb. At 10 - 20 ppb  $\text{NO}_x$  hydroperoxide concentrations are lower than at 5 ppb  $\text{NO}_x$  despite of higher  $\text{OH}$  concentrations showing that the  $\text{NO}_x$  effect superimposes the increase of  $[\text{OH}]$ .

Ketone concentrations show only a small increase at  $[\text{NO}_x] < 5$  ppb, and then remain constant until  $[\text{NO}_x] \sim 20$  ppb. Compared to the hydroperoxides, the maximum of ketone concentrations is shifted to higher  $\text{NO}_x$  which is in agreement to the assumption that  $\text{NO} + \text{HO}_2$  reactions have a higher rate constant than  $\text{NO} + \text{RO}_2$  reactions. From 30 ppb  $< [\text{NO}_x] < 70$  ppb, there is about 50% decrease in ketone that is explainable by the decrease in  $\text{OH}$  concentration. However, the total decrease from low  $\text{NO}_x$  to high  $\text{NO}_x$  conditions is small when compared to the decrease of hydroperoxide concentrations.

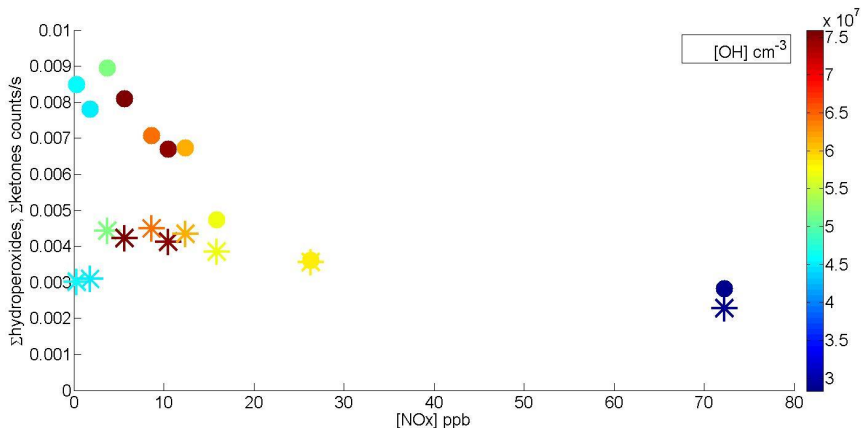


Figure 5.9 Total hydroperoxide (filled circles) and ketone (stars) signal intensities as a function of  $[\text{NO}_x]$ .  $[\text{OH}]$  included in colour code. Adding  $\text{NO}_x$  in the system offers additional termination pathway for peroxy radical, and immediate decrease of hydroperoxide at low  $[\text{NO}_x]$  suggests that  $\text{RO}_2 + \text{NO}$  pathway is highly efficient competing  $\text{RO}_2 + \text{HO}_2$ . Additionally,  $\text{NO}_x$  reacts with  $\text{HO}_2$ , leading to decrease in  $\text{HO}_2$  concentration, which together with organic nitrate pathways are enough to overcompensate the increased peroxy radical formation due to increased OH concentration and activation of the alkoxy-peroxy pathway.

From the examples given here, it can be stated that adding  $\text{NO}_x$  into the reaction system clearly changes the fate of the peroxy radical, and thus the formation of  $\text{HOM-RO}_2 + \text{RO}_2/\text{HO}_2$  reaction products.

All considered it is clear that pathways R5.1a and R5.1c are important termination pathways to  $\text{HOM-RO}_2$  in high  $\text{NO}_x$  regimes. If considering monomer range end products alone, remember from Chapter 4 that hydroperoxides are the main monomer termination pathway to peroxy radicals at low  $\text{NO}_x$  conditions, and keep in mind the sharp decrease of hydroperoxides and clear increase of organic nitrates with increasing  $[\text{NO}_x]$  it is justifiable to consider these two compound classes as the main end products at HOM monomer range, and in total HOM range at high  $[\text{NO}_x]$  cases when dimer production is inhibited.

Monomer HOM formation is determined by hydroperoxide and nitrate formation, and the relative contribution from the two pathways. Concentrations of organic nitrates higher than those of hydroperoxides can be explained by higher  $[\text{NO}]$  and  $[\text{NO}_2]$ , respectively, than  $[\text{HO}_2]$ . The higher  $[\text{NO}_x]$  then also causes suppression of other pathways including dimer formation. Figure 5.10 shows the ratio of dimer to monomer signal intensities as a function of  $[\text{NO}_x]$ . As expected this ratio strongly decreases. However, even at 70 ppb  $\text{NO}_x$  (i.e. at 3.2 ppb  $\text{NO}$ ) dimer concentrations are not zero. This requires peroxy radicals in the system and also here the alkoxy-peroxy pathway that forms peroxy radicals back is a possible and consistent explanation.

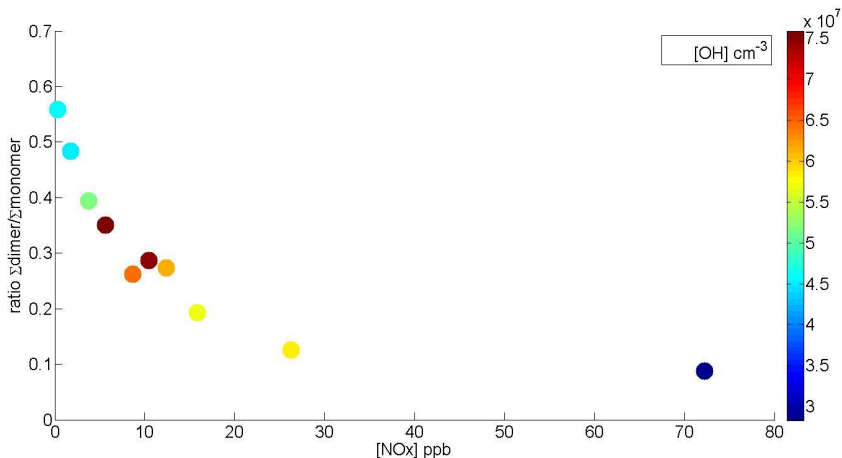


Figure 5.10 Ratio of total dimer concentration to total monomer concentration as a function of [NO<sub>x</sub>]. Colour code indicates [OH].

To summarize, adding NO<sub>x</sub> into the system increases HOM formation due to increased [OH] and due to activation of alkoxy-peroxy pathway. Peroxy radical termination is shifted from hydroperoxide and dimer formation towards organic nitrate and PAN-like nitrate formation. To offer further support for the analysis given here with α-pinene, the next chapter will give a short summary on the effects of NO<sub>x</sub> addition on photochemical HOM formation from β-pinene.

## 5.2. Photochemistry of β-pinene in the presence of NO<sub>x</sub>

The effect of NO<sub>x</sub> on HOM formation from α-pinene can be compared to the effect NO<sub>x</sub> has on HOM formation from β-pinene. Compared to α-pinene, β-pinene HOM formation includes strong fragmentation, which complicates peak analysis and the identification of single peak. Here only general behaviour of β-pinene HOM formation is considered, and individual compounds are not analysed. Figure 5.11 shows the effect of NO<sub>x</sub> on HOM formation from β-pinene photooxidation.

When there is no NO<sub>x</sub> addition into the system, the total HOM monomer concentration is 0.004 counts/s, and dimer concentration 0.001 counts/s. Adding NO<sub>x</sub> leads to four times higher HOM formation, with monomer 0.02 counts/s and dimer concentration 0.006 counts/s. However, the used β-pinene concentration was higher during NO<sub>x</sub> experiment.

As can be seen, dimer production has in fact increased (compared to small decrease in α-pinene). However, these values have been calculated using rigid monomer and dimer limits. Considering the monomer and dimer patterns in β-pinene HOM formation during NO<sub>x</sub> addition, there seems to be a

clear shift towards higher oxidation state molecules, and the “valley” between monomer and dimer masses almost has disappeared. It looks very likely that the mass range that would under very low  $\text{NO}_x$  conditions consist dominantly of dimers, might now be including many higher oxidation state monomer compounds. Or the fractioning during  $\beta$ -pinene oxidation and the following variety of compounds with different C-number could lead to production of HOM dimers with much lower masses than under pure photooxidation case. If considering monomer and dimer HOM formation together (and avoiding the need to specify which group an individual peak belongs to) it becomes clear that adding  $\text{NO}_x$  has greatly increased  $\beta$ -pinene HOM production under this  $\text{NO}_x$  concentration (0.005 counts/s without  $[\text{NO}_x]$  addition and 0.02 counts/s with  $[\text{NO}_x]$ ).

The OH concentration is slightly lower in the case without  $\text{NO}_x$  addition ( $4.6 \cdot 10^7 \text{ cm}^{-3}$ ) compared to  $5.75 \cdot 10^7 \text{ cm}^{-3}$  with  $\text{NO}_x$ , which is not enough to explain the observed increase. However, when comparing the  $\beta$ -pinene concentrations in both cases (0.06 ppb without  $\text{NO}_x$  and 1.0 ppb with  $\text{NO}_x$ ), it can be seen that the oxidation rate is much higher in the case with added  $\text{NO}_x$  ( $1.2 \cdot 10^8 \text{ cm}^{-3} \text{ s}^{-1}$ , compared to  $5.9 \cdot 10^6 \text{ cm}^{-3} \text{ s}^{-1}$  without  $\text{NO}_x$ ), and thus HOM production can be expected to be much higher as well.

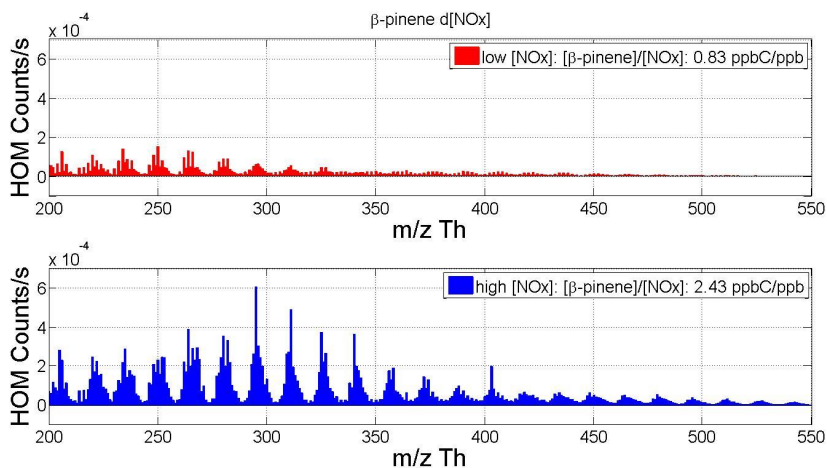


Figure 5.11 Overview of  $\beta$ -pinene HOM formation pattern. Upper panel shows  $\beta$ -pinene photochemical HOM formation without  $\text{NO}_x$  addition ( $[\text{NO}_x] \sim 0.75 \text{ ppb}$ ), lower panel portraits an example of  $\beta$ -pinene HOM formation pattern under moderate  $\text{NO}_x$  addition (4.1 ppb). OH concentrations in both cases are comparable ( $4.60 \cdot 10^7$  at low  $\text{NO}_x$  case, and  $5.80 \cdot 10^7$  with  $\text{NO}_x$ ), while  $\beta$ -pinene concentrations are 0.06 ppb and 1.0 ppb, respectively. Introducing  $\text{NO}_x$  into the system increases HOM formation in monomer range, and causes a shift towards higher oxidation state end products. Compared to  $\alpha$ -pinene the higher fragmentation of  $\beta$ -pinene is also evident under  $\text{NO}_x$  conditions, and can be seen as more “crowded” mass spectra. The monomer range is also seemingly extended towards dimer masses. Total monomer concentration without  $\text{NO}_x$  addition is 0.004 counts/s and dimer concentration 0.001 counts/s. With  $[\text{NO}_x]$  monomers are 0.02 counts/s and dimers 0.006 counts/s.

Another possible explanation for having much higher HOM concentrations during NO<sub>x</sub> addition (and at only slightly higher [OH]) would be if the alkoxy-peroxy pathway is also important for β-pinene photooxidation.

Furthermore the systematic shift of the monomers to higher oxidation state is obvious. This also fits with the figure of the alkoxy-peroxy pathway being important. Consistently, there is higher signal intensity for peroxy radicals with [NO<sub>x</sub>] ~ 4 ppb than for [NO<sub>x</sub>] ~ 0.74 ppb (Figure 5.12), despite oxidation rate four hours after NO<sub>x</sub> addition was stopped being  $1.05 \cdot 10^8 \text{ cm}^{-3} \text{ s}^{-1}$ , similar to during NO<sub>x</sub> addition ([OH] 2.56e8, [bpin] 2ppb).

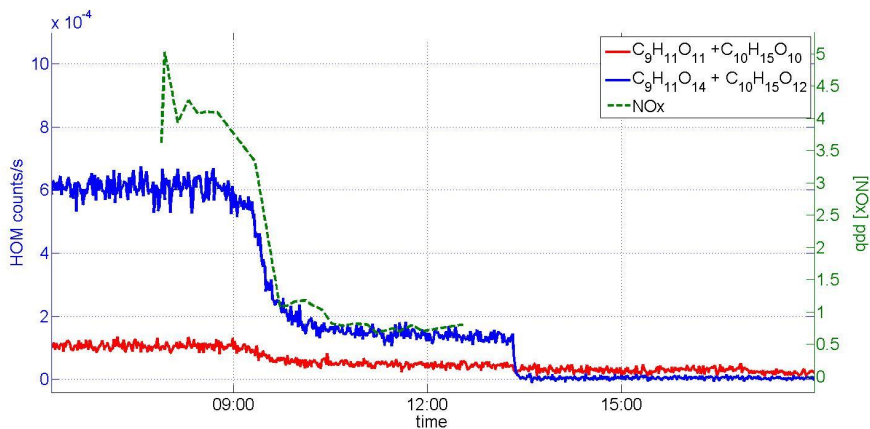
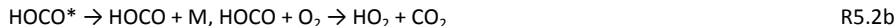


Figure 5.12 Temporal shape of signal intensities for peroxy radicals produced during β-pinene photooxidation. At the beginning of the experiment (before 9:00) NO<sub>x</sub> concentration in the chamber was 4.1 ppb. Then NO<sub>x</sub> addition was stopped and NO<sub>x</sub> was flushed out. For all identified peroxy radicals signal intensities decreased when NO<sub>x</sub> concentrations decrease, despite oxidation rate remaining similar ( $1.05 \cdot 10^8 \text{ cm}^{-3} \text{ s}^{-1}$ ).

### 5.3. CO + HOM

As discussed NO converts HO<sub>2</sub> into OH radicals thus increasing [OH] and accelerating the oxidation chemistry. CO will convert OH in HO<sub>2</sub> thus decreasing [OH] and increasing one of the major termination agent.

To test the effect of different [OH]/[HO<sub>2</sub>] ratios on overall HOM formation, CO was added to the α-pinene photooxidation system. CO reacts with OH and forms HO<sub>2</sub> (Wayne, 2006).



Adding CO therefore decreases OH concentration, and increases HO<sub>2</sub> concentration (R5.2a and R5.2b). Expectation was that increasing HO<sub>2</sub> concentration in the system would lead to higher hydroperoxide production, and lower dimer formation. Figure 5.13 shows how HOM formation from α-pinene photooxidation changed when CO was added to the system. Notice that the values on the Y-axis in the lower panel are lower by a factor of ten.

Adding high CO concentration led to strong reduction of [OH], and thus peroxy radical formation was reduced (example shown in Figure 5.13: ~ 57 ppm CO, [OH] during CO addition  $2.1 \cdot 10^6 \text{ cm}^{-3}$ , compared to  $3.8 \cdot 10^7 \text{ cm}^{-3}$  without CO). The signal intensities of all measured HOMs decreased, showing an about fourfold reduction of monomer intensities ( $8.5 \cdot 10^{-3}$  to  $2.2 \cdot 10^{-3}$  counts/s; -75 %) and tenfold reduction for the dimers ( $9.6 \cdot 10^{-3}$  to  $6.0 \cdot 10^{-4}$  counts/s; -93 %). The reduction of the ratio of dimers to monomers was higher, from dimer/monomer ratio of about 1 without CO to 0.27 with CO.

As can be seen, the patterns are quite different, with most of the peaks visible during high [CO] being either chamber/instrument background, or CO addition set-up contamination. High peak at 296 Th, a strong contamination from the CO set-up, has been allowed to go off scale. It can be clearly seen that the HOM formation has been strongly inhibited, and the remaining peaks are very low and mainly not HOMs.

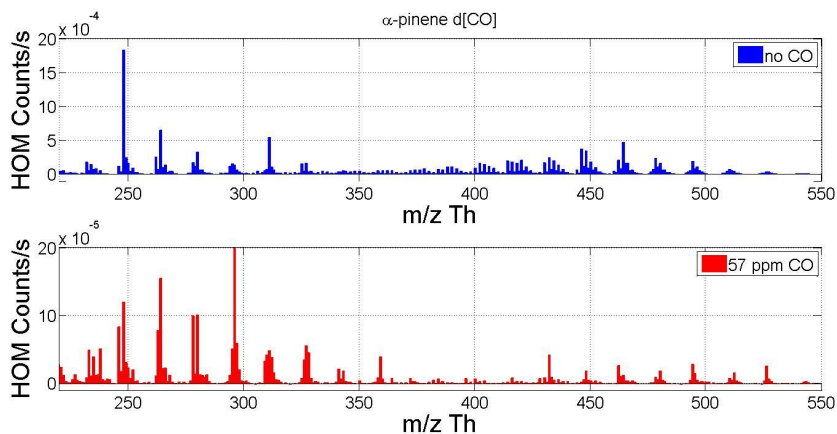


Figure 5.13 Comparing HOM pattern without CO addition (upper) and with CO (lower). HOM formation is clearly diminished.  $[OH]$  without CO addition  $3.8 \cdot 10^7 \text{ cm}^{-3}$ , and during CO addition  $2.1 \cdot 10^6 \text{ cm}^{-3}$ , more than an order of magnitude lower. Total monomer concentration without CO addition was  $8.50 \cdot 10^{-3} \text{ counts/s}$  and dimer  $9.60 \cdot 10^{-3} \text{ counts/s}$ . During CO addition monomer concentration dropped to  $2.20 \cdot 10^{-3} \text{ counts/s}$  and dimer to  $6.0 \cdot 10^{-3} \text{ counts/s}$ . Notice the different Y-axes. High peak at 296 Th was a strong contamination from the CO addition set up and was allowed to go off scale. Peaks left under high  $[CO]$  are either background contamination from the chamber and instrument, or contaminations from the CO set up.

After the high amount of CO was added to chamber, CO addition was stopped and CO was removed from the chamber by flush out, shown in Figure 5.14. As  $[CO]$  is decreasing,  $[OH]$  increases (and  $[HO_2]$  should decrease). Under CO it can clearly be seen how dimer concentration is much lower compared to monomer concentration. Removing CO from the chamber increases both monomer and dimer concentrations until concentrations reach maximum at  $\sim 9.0 \cdot 10^{-3} \text{ counts/s}$ . During the HOM maximum  $[\alpha\text{-pinene}]$  was 2.1 ppb,  $[CO]$  was estimated to be  $\sim 500 \text{ ppb}$  and  $OH$  concentration was  $2.2 \cdot 10^7 \text{ cm}^{-3}$ . After the maximum the behaviour of monomers and dimers differs slightly. While monomer concentrations decrease by about 10 %, dimer concentrations decrease less (3 %).

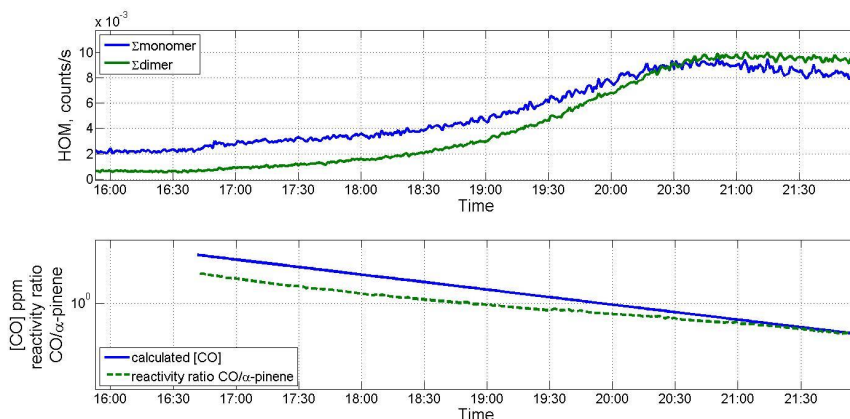


Figure 5.14 Temporal shape of total monomer and dimer concentrations during removal of CO from the chamber (upper panel) and [CO] and the ratio of CO and  $\alpha$ -pinene reactivities (lower panel). [CO] is decreasing mainly due to outflow from the chamber as reactions with OH are too slow to have a strong impact on [CO]. With decreasing [CO], [OH] in the chamber increases, and peroxy radical formation begins leading to increasing HOM concentration. Decreasing HOM concentration after maximum is explainable by particle formation, and increased particle surface in the chamber (see Figure 5.18).

Before discussing the decrease of the HOMs as shown in Figure 5.13, the behaviour of monomers, dimers, and hydroperoxides is discussed. Figure 5.15 shows the dimer to monomer ratio and the OH concentration as a function of the [CO] during this experiment. During high [CO] (and presumably high [HO<sub>2</sub>]) the dimer/monomer ratio is low ( $> 0.4$ ) due to stronger suppression of dimers than monomers during CO addition. The ratio increases slowly, until at [CO]  $< 10$  ppm the increase becomes faster, and finally at very low CO concentrations ( $< 1$  ppm) dimer concentration is higher than monomer. As mentioned, CO addition increases HO<sub>2</sub> concentration in the system, and the behaviour of dimer to monomer ratio under CO addition would suggest that the ratio [OH]/[HO<sub>2</sub>] is important in determining HOM formation.

As direct measurements of HO<sub>2</sub> concentration were not possible with the setup in the chamber, the dimer/monomer ratio under CO addition is compared to the dimer/monomer ratio when the [OH] in the chamber was regulated by changing  $J(O^1D)$ . The [OH]/[HO<sub>2</sub>] ratio under those conditions should be much higher. Figure 5.16 shows the oxidation rate dependence of dimer/monomer ratio during CO flush out in comparison to the experiment where [OH] was changed via regulating  $J(O^1D)$ .

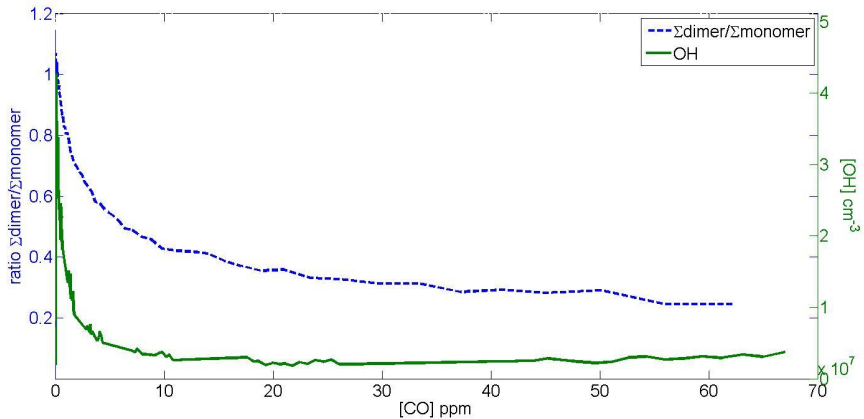


Figure 5.15 Ratio of dimer to monomer signal intensities as function of [CO]. With decreasing [CO] this ratio strongly increases demonstrating the effect of  $\text{HO}_2$  in dimer and monomer formation. When flushing out CO, OH concentration increases in the chamber, and  $[\text{HO}_2]$  decreases. Increasing [OH] leads to increase in peroxy radical production, and thus increased termination product formation. Decreasing  $\text{HO}_2$  concentration leads to higher dimer production compared to monomer production (hydroperoxides from  $\text{HO}_2 + \text{RO}_2$  are the main monomer range end product), and thus dimer concentration exceeds monomer concentration at low [CO].

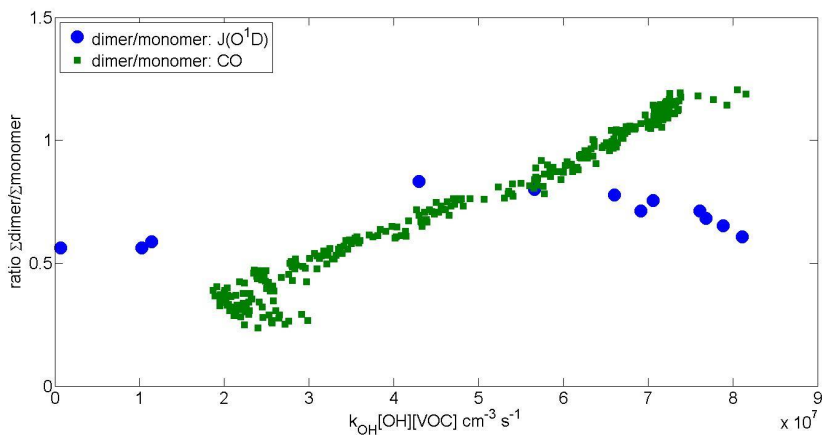


Figure 5.16 The ratio of [dimer] to [monomer] as function of  $k[\text{OH}][\alpha\text{-pinene}]$  (Variations of [OH] achieved by changing the  $J(\text{O}^1\text{D})$  in the chamber (blue circles) or by  $d[\text{CO}]$  (green squares). When [OH] is changed by changing  $J(\text{O}^1\text{D})$ , the ratio ranges from  $\sim 0.6$  to  $\sim 1$ . During CO addition, the change in ratio is much larger, ranging from  $\sim 0.3$  to 1.2. The oxidation rates are comparable, so the difference is likely to be in the  $[\text{OH}]/[\text{HO}_2]$  ratio, with more  $\text{HO}_2$  present in the system with CO.

When [OH] was changed by changing  $J(O^1D)$  (blue circles), during the ozonolysis dominated system the dimer concentration compared to monomer concentration is low (ratio 0.6), but after [OH] increases dimer concentration quickly matches monomer concentration, yielding a ratio  $\sim 0.9$ , which then slowly decreases until at high [OH] ( $> 4.0 \cdot 10^7 \text{ cm}^{-3}$ ) the ratio is again close to that under ozonolysis. When comparing to the data from the CO experiment, it can be clearly seen that the ratio of dimer to monomer is much wider, yielding vastly lower ratios at low oxidation rate ( $\sim 0.3$ ), and higher ( $> 1$ ) at oxidation rates at which during the  $J(O^1D)$  experiment the ratio already shows decrease. The difference between the behaviour of the dimer/monomer ratio between the  $J(O^1D)$  experiment and CO experiment comes from changed  $[OH]/[HO_2]$  related to CO addition, and this further offers support for the role of  $HO_2$  in explaining the apparent different behaviour of monomer and dimer concentrations shown in Figure 5.14.

With high CO concentration in the chamber, OH is reacting with CO to create  $HO_2$ . Low [OH] reduces peroxy radical formation, which is the reason the total HOM formation is inhibited by CO addition. When CO is being flushed out of the chamber, OH concentration recovers, and peroxy radical formation resumes. With high concentration of  $HO_2$  present in the chamber due to  $(CO + OH \rightarrow HO_2)$  reaction; R5.2b), the main termination pathway goes via hydroperoxide formation, and leads to a faster increase of HOM monomer concentration compared to dimers, which recover slower (as seen in Figure 5.14). As more CO leaving the system leads to  $HO_2$  concentration decreasing as well, termination pathway to dimers becomes stronger, and dimer concentration increases faster (compared to monomer).

Figure 5.17 shows the difference in temporal behaviour between hydroperoxide and corresponding ketone. Due to low intensities seen with the CIMS combined with contamination from the CO set-up, the peroxy radical data was excluded from this figure. CO concentration decrease leads to the hydroperoxides immediately increasing (increase in [OH] starting peroxy radical formation). Due to high  $[HO_2]$  in the system, the reactions of peroxy radical with  $HO_2$  lead to strong hydroperoxide formation. Total ketone formation is less affected. With increased peroxy radical formation also total ketone formation increases. The decrease seen in monomers Figure 5.14 can also be seen here in the total hydroperoxide signal.

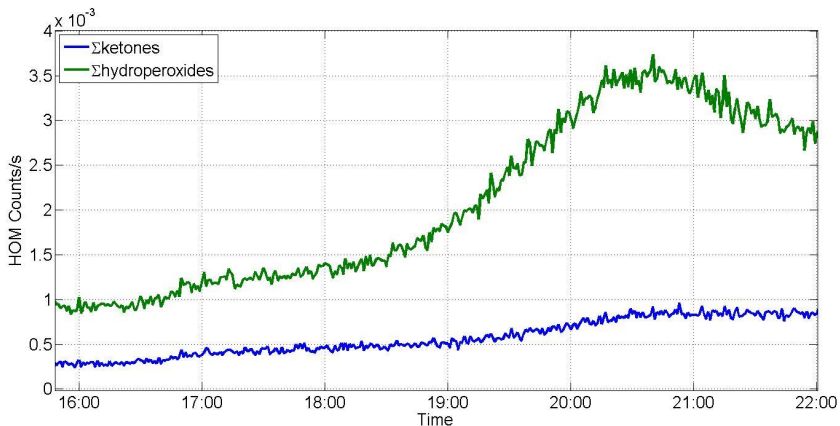


Figure 5.17 Total ketone and hydroperoxide signal during CO removal experiment. [CO] is not included in the figure, but follows the same behaviour as in Figure 5.14 Hydroperoxide and ketone signals increase when CO is being flushed out. Decrease in hydroperoxide signal is a combination of increased condensational sink from particles, and decrease of  $[\text{HO}_2]$  following CO being flushed out. Decrease in ketone signal is not that pronounced as the lower  $[\text{HO}_2]$  favours ketone formation.

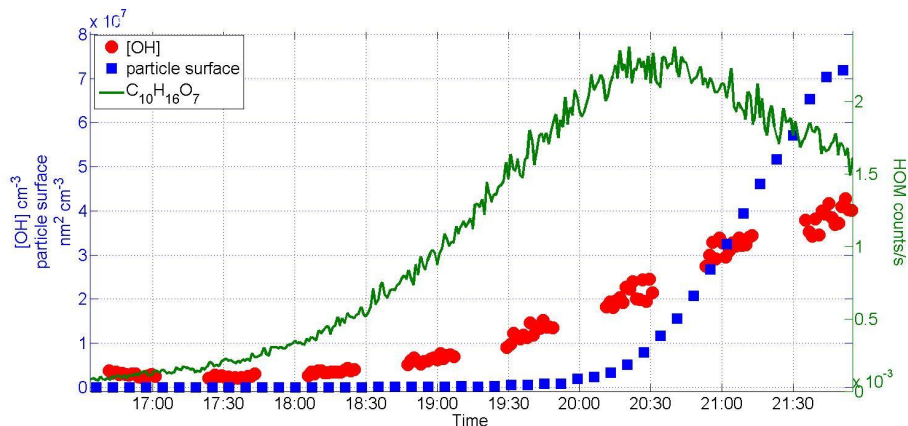


Figure 5.18  $\alpha$ -pinene HOM during gradual [CO] showing hydroperoxide  $\text{C}_{10}\text{H}_{16}\text{O}_7$ , [OH], and total surface (in units of  $\text{nm}^2 \text{ cm}^{-3}$ ). [OH] increase follows the decrease of [CO]. HOM monomer formation begins soon after [CO] is below 60 ppm (reactivity ratio  $\sim 11$ , see Figure 5.14), getting faster the lower [CO] is. After sufficient HOM formation has taken place, and particle surface begins increasing, HOM begins to condense on particles, and HOM concentration decreases with increasing particle surface.

Overall, from the changes seen in the dimer/monomer concentration ratio it seems that overall production of HOM is reduced during CO addition and that the pathway has been shifted more towards hydroperoxides, away from dimers. This is due to  $[\text{HO}_2]$  increase which leads to increased role of hydroperoxide channel.

Now the decreasing signal intensities observed for all HOMs (except of peroxy radicals) can be addressed, and Figure 5.18 shows a HOM monomer trace plotted together with  $[\text{OH}]$  and particle surface. As obvious from Figure 5.14, monomer and dimer concentrations decrease after their respective maxima. As will be described in the Chapter 6, the decrease is due to the formation of particles that offer an additional condensational sink. Obviously the increase in sink strengths is stronger than the increase in  $[\text{OH}]$  or the oxidation rate, respectively. However, dimers seem to be less affected than monomers as the decrease in dimer concentrations appears later than that of monomers and the decrease is less pronounced. On a first view this might indicate that the condensational sink for dimers is lower than that for monomers. This is not the case. Reason for the delayed and less pronounced response of the dimers compared to the monomers is the suppression of dimer formation by  $\text{HO}_2$ .

The maximum in monomer concentrations is reached when there is  $\sim 460$  ppb CO in the system, meaning that the reactivity versus OH reactions is still about  $3 \text{ s}^{-1}$ . This is similar to the reactivity of  $\alpha$ -pinene (2.1 ppb at that point in time, reactivity =  $2.8 \text{ s}^{-1}$ ) and hence there is still a strong  $\text{HO}_2$  source from CO oxidation in the system. Due to restrained dimer formation the ratio of dimers over monomers has not yet reached the same level as during pure photooxidation. But together with the flush out of CO,  $\text{HO}_2$  formation is diminished and the restriction of dimer formation becomes less. This highlights the role of  $\text{HO}_2$  in HOM formation.

#### 5.4. Concluding remarks on chemical transformation HOMs

By adding  $\text{NO}_x$  into the system it was possible to further validate the hypothesis of peroxy radical as a starting point for HOM formation.  $\text{NO}_x$  addition led to organic nitrate formation at masses where organic nitrates were predicted assuming the radical seen in the mass spectrum was a peroxy radical. This confirmed the assignment of HOMs with odd masses being peroxy radicals. Increased  $[\text{NO}_x]$  led to decrease in hydroperoxide concentration, due to both increased reaction of  $\text{HO}_2$  with NO (R5.1d), as well as higher  $[\text{NO}_x]$  leading to increased reactions of peroxy radicals with NO or  $\text{NO}_2$  (R5.1a-c). Also dimer formation was impeded by  $\text{NO}_x$  addition. In summary all HOMs followed the known pathways of peroxy radical chemistry and most of the chemical behaviour observed was compatible to peroxy radical chemistry.

One important pathway had to be considered in addition, the alkoxy-peroxy pathway. Shifts in the oxidation state, and the finding that even at very high  $\text{NO}_x$  levels the formation of termination products of  $\text{RO}_2 + \text{RO}_2$  was not completely inhibited suggested an important role of the alkoxy-peroxy pathway.

Similarly, the experiment with CO also confirmed the assignment of peroxy radicals and termination products. The experiment furthermore revealed that HO<sub>2</sub> plays a key role in determining the fate of HOMs including oppression of dimer formation.

## Chapter 6 Sinks of HOMs: condensation on particles and wall loss

HOMs have been suggested to have extremely low vapour pressures (Ehn et al., 2014). However, there are some studies that suggest based on chemical models that despite high O:C ratios, HOMs produced by  $\alpha$ -pinene ozonolysis might not have sufficiently low vapour pressures ( $< 10^{-14}$  bar) to be considered as ELVOC (Kurtén et al., 2016). This would have implications on the importance of HOMs on atmospheric new particle formation, and particle growth.

This chapter will focus on studies on the importance of HOMs on particle growth. This is shown by estimating the effective uptake coefficients for the  $\alpha$ -pinene HOMs. Determinations of effective uptake coefficients were complicated by  $\text{RO}_2$  chemistry that was influenced by the particles formed in the system. However, these findings also implicated a role of particles in atmospheric radical chemistry.

The role of photochemically produced  $\alpha$ -pinene HOMs for particle growth was already implied from following their concentrations after inducing primary OH production. Figure 6.1 shows the temporal shape of HOM monomers and HOM dimers in the chamber under high  $\alpha$ -pinene and high OH concentrations. After OH production is initiated, HOM concentrations rapidly increase and reach a maximum within minutes ( $< 10$  minutes). Thereafter HOM concentrations decrease and within  $\sim 40$  minutes local minima are reached. Slowly the concentrations increase again, until steady state is reached in at approximately halfway between the minimum and maximum of respective compound (slightly lower at dimers).

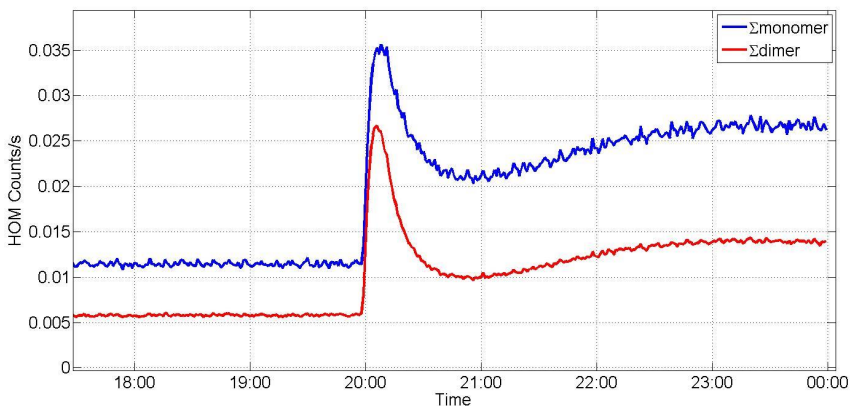


Figure 6.1 Time series showing temporal shape of HOM signal intensities (proportional to concentrations), here as total monomer and dimer concentrations, after initiating OH production. The respective experiment was performed under relatively high OH ( $4.4 \cdot 10^7 \text{ cm}^{-3}$ ) and  $\alpha$ -pinene concentrations (6.0 ppb before OH production; 1.5 ppb in presence of OH). After inducing primary OH production, HOM formation is fast and reaches maximum values in minutes. After reaching maximum, HOM concentrations in the chamber decrease fast, and a local minimum is reached in 30-40 minutes. Concentration then increases again, and reaches a steady state in few hours.

The decreases of HOM concentrations after the maxima were too fast to be explained by flush out from the chamber, and the subsequent increase is inconsistent with the idea as well. The only option to explain this behaviour is losses of HOMs on the particles produced during  $\alpha$ -pinene photooxidation. Note that the behaviour is different for monomers and dimers. When comparing the ratio of minimum to maximum, the minimum is lower for the dimers (ratios 0.6 for monomers and 0.4 for dimers).

Figure 6.2 shows the temporal behaviour of total HOM concentration (monomer + dimer), with forming particle surface and particle mass. The particle surface begins to increase approximately when HOM concentration reaches maximum, reaching high enough values to add significant surface area for HOM to condense on. The maximum in particle surface coincides with the minimum in HOM concentration, after which due to coagulation of the particles the total available particle surface begins to decrease. While the total surface onto which the HOM could condense on decreases, the HOM concentration increases, until a steady state in both HOM concentration and particle surface has been reached.

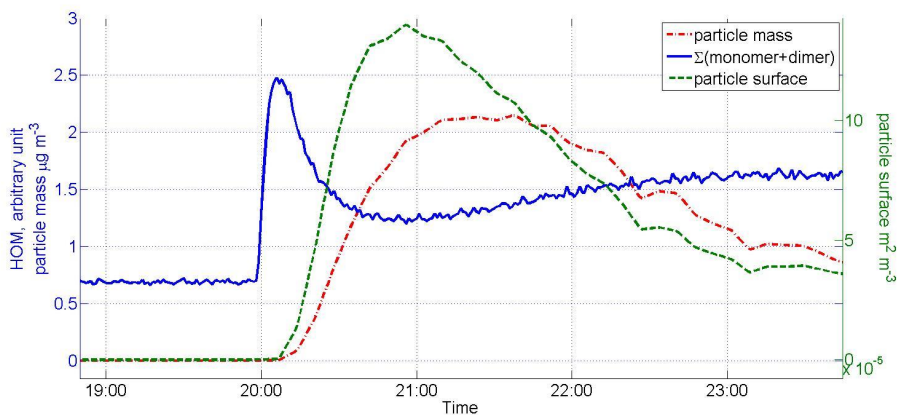


Figure 6.2 Temporal shape of HOM concentrations and particle mass and surface. HOM signal intensities typically show a rapid increase as OH is produced leading to a burst of HOM formation. Green tracer shows the slower increase of particle surface in the chamber. After enough particle surface has been produced to add significantly to sink strength, the HOM concentrations decrease until a maximum in particle surface and a minimum in gas phase concentrations of HOMs is reached. Thereafter, particle surface decreases again, probably due to coagulation which offers the HOMs less particle surface to condense on. Eventually a steady state is reached. For clarity the HOM signal was scaled up.

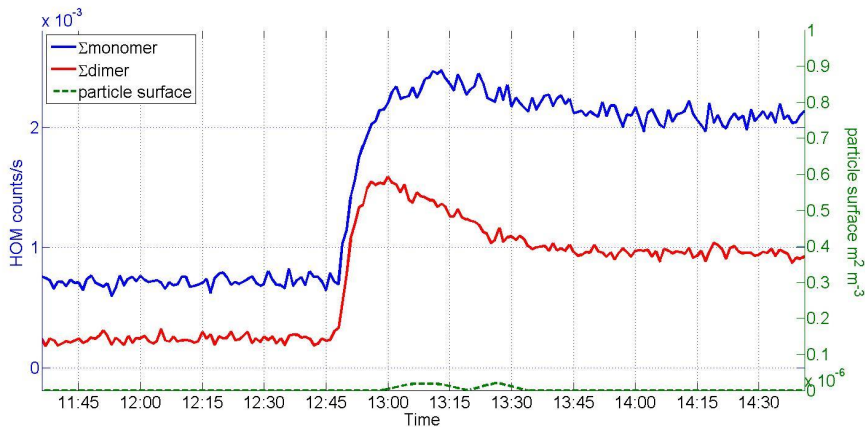


Figure 6.3 Time series of monomer formation under low [OH] conditions, when particle formation is negligible. HOM formation still shows a maximum after OH production is initiated, but the steady state is reached without a minimum in concentration. When there is no particle formation taking place, the only surface available is in the chamber walls, which remains constant. The slight decrease in HOM concentration can be attributed to flush out from the chamber, before production and flushing out reach equilibrium.

The idea of condensation of HOMs on particles being responsible for the strong decrease after the maxima was confirmed by measurements, where due to lower OH concentrations there was no substantial particle formation (Figure 6.3).

The increase of HOM concentration in the chamber is still very rapid after OH production is initiated. But, instead of reaching very high peak values and subsequent decrease to a temporary minimum, the HOM concentration reaches maximum at the same time as in the high OH case and thereafter is almost immediately in steady state. There is small decrease that is however much less pronounced than in the presence of higher particle surface. The decrease of HOM dimer concentration from maximum to steady state is larger than the equivalent in monomer concentration (similar as was seen in Figure 6.1).

From the behaviour shown in figures 6.2 and 6.3 it can be deduced that additional to losses to the walls, condensation to particle surface is the main sink for HOM in the chamber.

In the next chapter results on how lifetimes of HOMs were influenced by the abundance of particles will be shown. This requires showing also data on wall losses.

## 6.1. Condensation on particles

There are two major loss pathways to closed shell HOM molecules in the chamber. They are either lost by condensation to walls, or to particle surface.

To determine the loss rate of HOM onto chamber walls, the system was run until steady state under photooxidation regime. Then OH production was stopped which led to a fast decay of HOM signal intensities. As the lifetime of OH in the chamber with [VOC] higher than 1ppb is below 1s, the decay in signal following the stop of OH production can be used to determine HOM loss to the chamber wall. Figure 6.4 shows logarithmic signal intensities from two different HOMs plotted versus time in seconds after OH production ended. The lifetime of the two HOMs due to wall losses was  $\sim 95$ s. Depending on the compound lifetimes may be different, with larger molecules having longer lifetimes (slower diffusion through the boundary layer at the chamber walls). At these time scales the [VOC] and  $[O_3]$  did not change despite loss of OH.

Portion of the produced HOM is also flushed out of the chamber continuously, but as the average residence time in the chamber is 45 minutes, and the average life time of a HOM is in the order of 100-200 seconds, the relevance of flush out is small compared to losses on walls and particles. Loss by flush out is therefore neglected here.

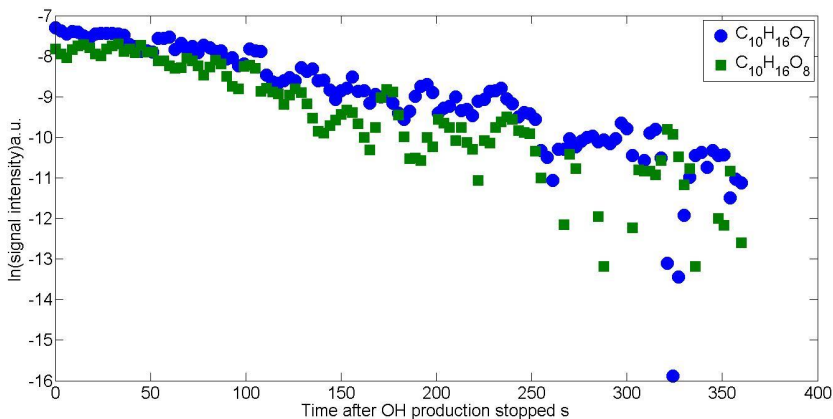


Figure 6.4 Plotting HOM concentration versus time gives idea about the loss of HOM onto the chamber walls. With loss rate  $0.0105 \text{ s}^{-1}$  the lifetime of the HOM molecule is  $\sim 95$ s.

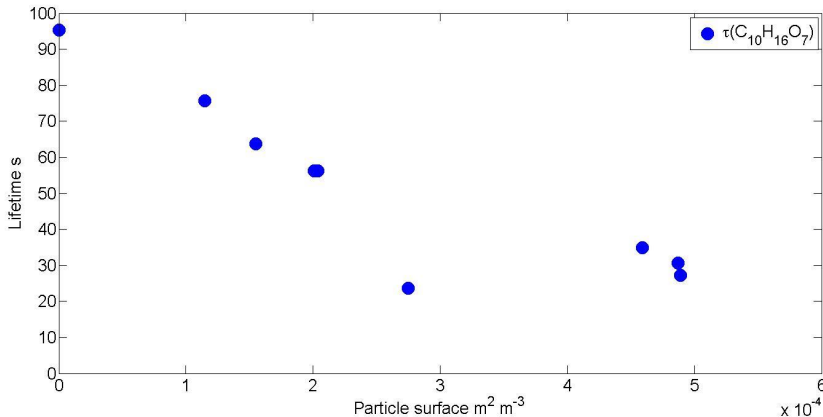


Figure 6.5 Lifetime of HOM determined using regression analysis of HOM signal intensities (as shown in Figure 6.4) plotted here against particle surface.

In presence of particles the total surface for the HOM to condense on is higher than without particles. Measuring the lifetime of HOMs at different amounts of particles in the chamber showed that the higher the particle surface, the lower was the lifetime (Figure 6.5). Measurements were made with particles formed by homogeneous nucleation in the chamber during experiments with different  $J(O^1D)$  (e.g. OH concentration), without additional seeding. For reliable results only peaks with high intensity were used and example shown here is for the hydroperoxide  $C_{10}H_{16}O_7$ .

For lower signals, which are too noisy when using time resolution below 10s, the lifetimes of HOM were determined by using steady state data from seeded experiments. When having the HOM production rates constant (constant [VOC], [OH], and  $[O_3]$ ), and seed is either added or removed, it should be possible to use the following formula to derive the lifetime:

$$c(H) = \frac{P(H)}{L(H)} = P(H) \cdot \tau(H) \quad (\text{Eq. 6.1})$$

Where  $c(H)$  is the concentration of a given HOM,  $P(H)$  is HOM production rate,  $L(H)$  is HOM first order loss rate, and  $\tau(H)$  is HOM lifetime. Assuming that the HOM concentration is proportional to the measured signal intensity, it can be said that  $c(H) = S(H) \cdot \alpha$ , where  $S(H)$  is the signal intensity, and  $\alpha$  is an unknown calibration constant. Due to wall losses and losses to particles being very efficient, outflow from the chamber was neglected. For a closed shell HOM this leaves wall losses ( $L_w(H)$ ) and losses to particles ( $L_p(H)$ ) as main loss processes. Introducing this to Eq. 6.1 results in Eq. 6.2.

$$S(H) \cdot \alpha = \frac{P(H)}{L_w(H) + L_p(H)} = P(H) \cdot \tau(H) \quad (\text{Eq. 6.2})$$

When using the signal intensity at negligible particle surface (index “0”) and the signal intensity with different particle surface, the ratio reflects directly the ratio of the lifetimes of HOM. The calibration constant cancels out, as does production rate as long as it is constant. This leaves following equation:

$$\frac{S(H)^0}{S(H)} = \frac{\tau(H)^0}{\tau(H)} = \frac{L_w(H) + L_p(H)}{L_w(H)} \quad (\text{Eq. 6.3})$$

From there  $L_p(H)$  can be determined

$$L_p(H) = \frac{S(H)^0}{S(H)} \cdot L_w(H) - L_w(H) \quad (\text{Eq. 6.4})$$

Using equation Eq. 6.4 the loss rate on particles can be calculated using measured data. Figure 6.6 shows losses of HOM on particles as a function of particle surface, and it's determined from measurement when [OH], [ $\alpha$ -pinene] and [ $O_3$ ] were kept constant in order to keep P(H) constant. In this experiment addition of seed particle into the chamber was stopped and existing particles were flushed out.

From kinetic gas theory  $L_p(H)$  can be determined to be

$$L_p(H) = \gamma_{eff} \cdot \frac{v}{4} \cdot S_p \quad (\text{Eq. 6.5})$$

Where  $v$  is HOM mean velocity,  $S_p$  is particle surface, and  $\gamma_{eff}$  is the effective uptake coefficient of the HOM.  $L_p(H)$  should linearly depend on the existing particle surface and dividing the slope of plots of  $L_p(H)/S_p(H)$  by  $v/4$  should give the effective uptake coefficient (see also supplement to Sarrafzadeh et al., 2016).

$$\gamma_{eff} = \frac{L_p(H) \cdot \frac{4}{v}}{S_p} \quad (\text{Eq. 6.6})$$

However, plotting  $L_p(H)$  versus the particle surface  $S_p$  measured simultaneously, for several HOMs a curvature was observed (Figure 6.6) This does not comply with the kinetic gas theory.

The procedure was already used to determine effective uptake coefficients for  $\beta$ -pinene (Sarrafzadeh et al., 2016). In this case it worked quite well and on a first view this seems to contradict results obtained for  $\alpha$ -pinene. However, there were two major differences in the experimental procedure:

1. The dynamic range of surface variation was lower in the case of  $\beta$ -pinene, making a curvature not that obvious than in Figure 6.6; and
2. The experiments with  $\beta$ -pinene in (Sarrafzadeh et al., 2016) were made in the presence of  $NO_x$  ( $[NO_x] \sim 4$  ppb,  $[\beta\text{-pinene}]/[NO_x] \sim 1.8$  ppbC/ppb) whereas the experiments with  $\alpha$ -pinene were made without  $NO_x$  addition. Hence the product pattern of termination products was very different in these two cases. In the case of  $\beta$ -pinene less  $HO_2$  and thus less hydroperoxides (and due to  $NO_x$  less dimers, see Chapter 5) were in the chemical system. Instead more organic nitrates were formed.

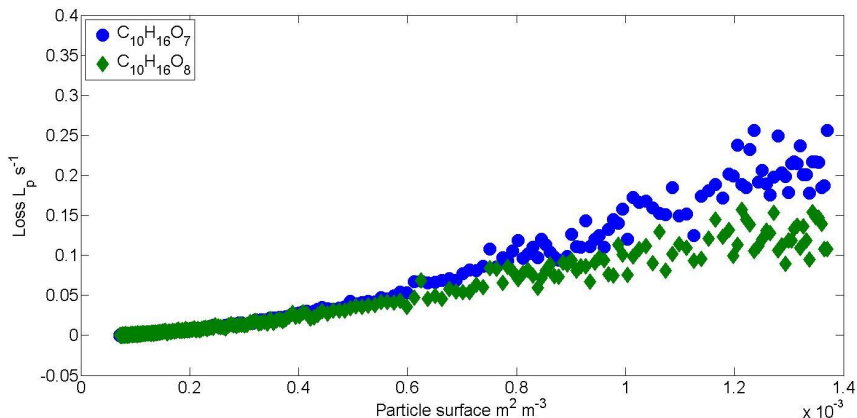


Figure 6.6 Loss rates of HOM from  $\alpha$ -pinene as a function of particle surface. [ $\alpha$ -pinene], [OH] and [ $O_3$ ] were kept constant and particle surface was varied by changing concentration of ammonium sulphate seed (concentration up to  $60 \mu\text{g m}^{-3}$ ). Using all data for the two hydroperoxides shown to determine their effective uptake coefficients would lead to unrealistic high numbers of around 2 to 3 per collision.

A self-consistent hypothesis that might explain the differences in the results of  $\alpha$ -pinene and  $\beta$ -pinene, as well as the curvature shown in Figure 6.6 would be a strong impact of particles on peroxy radical chemistry in case of  $\alpha$ -pinene compared with much less impact in the case of  $\beta$ -pinene.

Hydroperoxides are the dominant monomer HOM class in photooxidation of  $\alpha$ -pinene in the absence of  $\text{NO}_x$ , and formation of hydroperoxides requires  $\text{HO}_2$  to be abundant in the system. In contrast to OH which has lifetime far below a second, the lifetime of  $\text{HO}_2$  can be up to several seconds, and losses of  $\text{HO}_2$  on particles cannot be excluded (Brune et al., 1999; Carslaw et al., 2002; Haggerstone et al., 2005; Lakey et al., 2015). If  $\text{HO}_2$  losses on particles diminish  $\text{HO}_2$  concentrations in the chemical system, the formation rate of hydroperoxides would also be lower. Lower formation rates with decreasing  $\text{HO}_2$  concentrations lead to lower concentrations for the hydroperoxides. Thus, in addition to condensation on particles and wall losses there is another process leading to lower HOM concentrations. Losses of  $\text{HO}_2$  on the particles in the chamber can explain lower than expected signal intensities from pure condensation of the hydroperoxides on particles. A hint to this is the different functional dependence of a hydroperoxide and a ketone on particle surface (Figure 6.7).

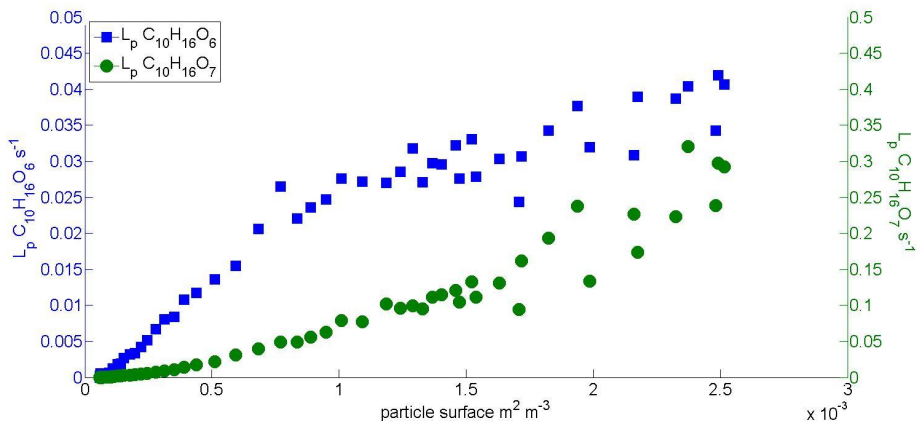


Figure 6.7 Loss rates of the hydroperoxide  $C_{10}H_{16}O_7$  (green circles, right y-scale), and the ketone  $C_{10}H_{14}O_6$  (blue squares, left y-scale), as a function of particle surface. Both HOMs are termination product of the same peroxy radical ( $C_{10}H_{15}O_7^{\cdot}$ ) and as can be seen, the curvature of the shapes is opposite.

While the curvature of the hydroperoxide implies increasing loss rates with increasing particle surface, the curvature of the ketone implies decreasing loss rates with increasing particle surface. According to the hypothesis of  $HO_2$  losses on particles, the apparent increase of the loss rate of the hydroperoxide is in reality a decrease of its formation rate. Correspondingly, the apparent decrease of the loss rate of the ketone is an increase of source strengths. Due to a lower abundance of  $HO_2$ ,  $RO_2 + RO_2$  reactions gain importance, leading to a higher production rate of the respective ketone.

In addition to the possible losses of  $HO_2$  on particles, the formation of termination products can be suppressed due to a shorter lifetime of the HOM-peroxy radical ( $C_{10}H_{15}O_7^{\cdot}$  in the case shown in Figure 6.7) in the presence of particle surface. If the formation of termination products would appear on a time scale of some 10 seconds, a loss of the parent peroxy radical by condensation on particles also would cause less production of its termination products. In addition to losses of  $HO_2$  on particles, the losses of HOM- $RO_2$  complicate the determination of effective uptake coefficients.

To diminish at least the impacts of  $HO_2$  chemistry, the signal intensities for the peroxy radical and its monomer termination products (hydroperoxide and ketone) were added up. The alcohol was not included because the signal is superimposed by the hydroperoxide formed from the peroxy radical with one O atom less than the considered one (see Chapter 4 for details). Figure 6.8 shows the result.

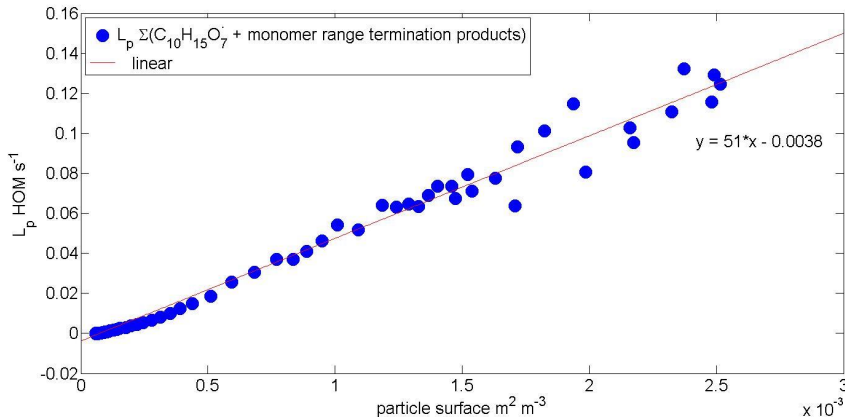


Figure 6.8 Loss rates of the sum of  $C_{10}H_{14}O_6$  (ketone),  $C_{10}H_{15}O_7^{\cdot}$  (peroxy radical) and  $C_{10}H_{16}O_7$  (hydroperoxide) as a function of particle surface.

From Figure 6.8 it is obvious that curvatures as observed in Figure 6.7 are much less pronounced. Using the slope of the plot to determine the effective uptake coefficient leads to 1.3, which is still above 1, the upper limit from kinetic gas theory. This implies another loss channel for the peroxy radical. This other loss channel is dimer formation. As dimers can be formed in different combinations of  $C_{10}-RO_2 - C_{10}-RO_2$  reactions, the exact dimers formed from (in this case)  $C_{10}H_{15}O_7^{\cdot}$  cannot be clearly identified. Therefore a more precise value for the effective uptake coefficient cannot be obtained here.

Depending on the peroxy radical under investigation the curvatures of individual plots are more or less pronounced. This hints to different effectivities of  $HOM-RO_2 + HO_2 / RO_2$  reactions. However, after summing up the signal intensities as in Figure 6.8, quite good linear relationships were obtained and curvatures were much less pronounced than for individual termination products.

At high particle surface the signal intensities for all HOMs were substantially suppressed. Signals were prone to be superimposed by noise and the impacts of reduced  $HO_2$  were strongest. To control if this might have an impact on the results a reactive uptake coefficient was derived by either using data for the entire available range of surface area, or using only data at particle surface below  $8 \cdot 10^{-4} m^2 m^{-3}$ . Depending on the effective uptake coefficient this surface is equivalent to a suppression of the signal intensity by a factor of 5 to 10, i.e. data with signal intensities below 10-20% of the maxima were rejected.

Table 6.1. The effective uptake coefficients as determined from plots of  $L_p(H)$  versus particle surface.

Parent Peroxy radical	$\gamma_{\text{eff}}$ all data <sup>a</sup>	$\gamma_{\text{eff}}$ only high signal intensities <sup>b</sup>	$\gamma_{\text{eff}}$ all data only termination products <sup>c</sup>	$\gamma_{\text{eff}}$ only high signal intensities only termination products <sup>c</sup>
$C_{10}H_{15}O_7^{\cdot}$	1.3	1.0	1.9	1.1
$C_{10}H_{15}O_8^{\cdot}$	0.45	0.67	0.71	0.82
$C_{10}H_{15}O_9^{\cdot}$	0.52	0.65	0.99	0.88
$C_{10}H_{15}O_{10}^{\cdot}$	0.51	0.73	0.86	0.87
$C_{10}H_{15}O_{11}^{\cdot}$	1.88	1.2	1.0	0.78
$C_{10}H_{15}O_{12}^{\cdot}$	0.76	0.75	0.60	0.56
$C_{10}H_{15}O_{13}^{\cdot}$	0.54	0.72	0.53	0.70
$C_{10}H_{15}O_{14}^{\cdot}$	1.0	0.85	1.0	0.85

<sup>a</sup>: To diminish impacts of chemistry the signal intensities of a peroxy radical and the respective ketone and hydroperoxide formed from this peroxy radical were summed up .

<sup>b</sup>: To further diminish residual impact of  $HO_2$  losses,  $\gamma_{\text{eff}}$  was also obtained using only data at particle surface below  $8 \cdot 10^{-4} \text{ m}^2/\text{m}^3$  .

<sup>c</sup>: To remove impacts of superpositions of peroxy radical signals the same calculations were also made by using only the signals from the termination products .

Another source of problem might be the signals of peroxy radicals themselves. As they are typically quite low they are also prone to be superimposed by other signals, in particular by N containing HOMs. To control if this might influence the results the effective uptake coefficients was calculated also by using the data for the termination products only (hydroperoxide and ketone). Also this was made twice, once using all data, and once using only the data at high signal intensities and low impacts of reduced  $HO_2$  (Table 6.1.).

Depending on the data set used for the calculations quite different results were obtained. For two series of HOMs the calculated values were still unrealistically high ( $C_{10}H_{15}O_7^{\cdot}$  and  $C_{10}H_{15}O_{11}^{\cdot}$ ). Rejecting the data with low signal intensities and the highest changes of HOM source strengths by impacts of particles on peroxy radical chemistry gave more realistic numbers. However, as the variation of the result was quite strong when changing the data set, realistic error margins are quite high ( $\pm 30\%$ ). These error margins are much higher than those from uncertainties from plots. Therefore, no data for the uncertainties of the plots itself are given here.

Another channel for individual peroxy radicals is the formation of an alkoxy radical that may also form a new peroxy radical with one O atom more than the parent peroxy radical (see Chapter 5). As also this pathway is initiated by a  $HOM-RO_2 + RO_2$  reaction, it will proceed on a similar time scale as the formation of termination products. For an individual peroxy radical this channel may be an additional source or sink.

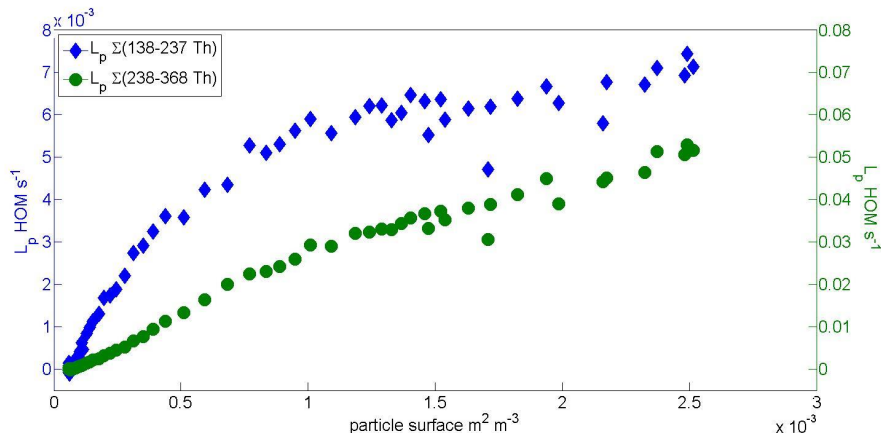


Figure 6.9 Average loss rates of HOMs as a function of particle surface. Green circles show the data for HOMs with higher number of O atoms (238-368 Th), rights y-axis. Blue diamonds show the data for HOMs with masses between 138 and 237 Th i.e. for HOMs with lower numbers of O atoms, left y-axis.

Considering all these uncertainties, the uncertainty of the values given in Table 6.1. are estimated to be  $\pm 30\%$ . Furthermore, the numbers obtained after rejecting the data with lowest signal intensities and highest residual impact of changed source strengths are suggested to be more reliable than those obtained using all data.

Despite of the uncertainties, the numbers determined for effective uptake coefficients were quite high. They implied near to collision limited condensation on particles, leading to the conclusion that HOMs are indeed very important precursors of SOA. As effective uptake coefficients depend on the vapour pressure of the respective compound and differences in the effective uptake coefficients may help finding more insight into processes of SOA formation, the possible effect of the alkoxy-peroxy pathway was also attempted to be minimized by summing up signal intensities.

To give an at least qualitative idea on the importance of the numbers of O atoms incorporated in the HOMs, the HOM monomers were arbitrarily separated into two groups: one group with molecular masses between 138 and 237 Th, i.e HOMs having typically less than six oxygen atoms. In the other group are HOMs with masses from 238 Th up to the limit of 368 Th where signals of monomers may overlap with signals of dimers. Figure 6.9 shows the result.

The difference in loss rates between HOMs with lower and higher masses is obvious. But there is also a curvature observable that might indicate residual impacts of chemistry. Again, to diminish the impacts of chemistry on the results, average effective uptake coefficients were estimated from the data with the lowest particle surface and thus lowest impacts of chemistry. For HOMs with  $O < 6$  an average  $\gamma_{\text{eff}}$  would be 0.17, for the group of HOMs with higher number of O atoms  $\gamma_{\text{eff}}$  would be 0.86.

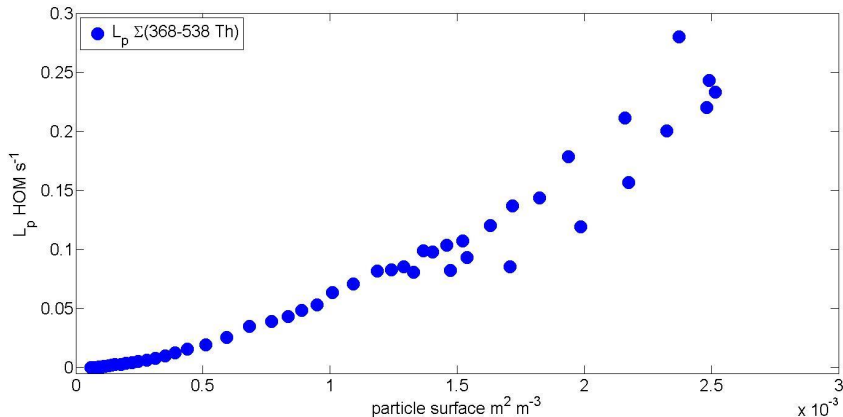


Figure 6.10 loss rates of HOM dimers in dependence of particle surface. Using data for all particle surfaces would lead to unrealistic high  $\gamma_{\text{eff}}$  of about 3. Restricting the data to low particle surfaces ( $< 8 \cdot 10^{-4} \text{ m}^2 \text{ m}^{-3}$ ) would lead to  $\gamma_{\text{eff}} \sim 1.0$

Following the argumentation line mentioned above with respect to the curvature in hydroperoxide and ketone signals, the curvature of the sums imply increasing source strength with increasing surface (loss rates seem to decrease with increasing surface). This effect cannot be assigned to  $\text{HO}_2$  losses at the surface of particles.

$\text{HO}_2$  concentrations are highest at low particle surfaces. Hence, at low particle surface  $\text{HO}_2$  prevents dimer formation. With increasing particle surface  $\text{HO}_2$  is lost and therefore dimer formation should be preferred. This alone would lead to an additional loss channel of monomers and the curvature should be the other way around. Similarly, decreasing  $\text{HO}_2$  with increasing particle surface should lead to increasing source strengths for dimers, and  $L_p$  as a function of particle surface should show similar shapes as found for the ketones. However, also for the HOM dimers the curvature of  $L_p$  is opposite than expected (Figure 6.10) implying an increasing sink with increasing surface.

Again, as for the loss rates of hydroperoxides, the unrealistic high  $\gamma_{\text{eff}}$  for the dimers implies a process in the gas phase that leads to lower source strengths with increasing particle surface. In addition to impacts of varied  $\text{HO}_2$ , the formation of termination products can be suppressed due to lower abundance of  $\text{RO}_2$ , in this case  $\text{HOM-RO}_2$ . Effective losses of  $\text{HOM-RO}_2$  on particles can explain the curvature as shown in Figure 6.10 as well as the unrealistic high effective uptake coefficients when using all data for their determination. Particularly in the absence of  $\text{NO}_x$  also HOM peroxy radicals can have lifetimes in the range of several seconds. If their chemical lifetime is in the range of their lifetime with respect to condensation on particles, increasing particle surface lead to losses of these radicals from the gas phase. Again, a similar time scale of chemical and condensational processes can explain the effects shown in Figure 6.9 and 6.10: The predominant fraction of dimers are  $\text{C}_{20}$  compounds, their formation

therefore requires collisions of two C<sub>10</sub> peroxy radicals. Diminishing monomer concentrations by their condensation on particles therefore also decreases the source strengths of dimers. This causes the curvature and leads to the unrealistic high  $\gamma_{\text{eff}}$ . Lowered dimer formation also lowers a loss process for monomers. Thus the curvatures shown in Figure 6.9 are understandable. However, this process must be efficient enough to superimpose the effects of lowered HO<sub>2</sub>. Dimer formation therefore must be a highly efficient process.

To summarize, quantitative determination of effective uptake coefficients for the HOMs produced from  $\alpha$ -pinene photooxidation is complicated because gas phase chemistry and condensational loss superimposed each other. This problem might be overcome when diminishing the effects of chemistry on the system. As mentioned above, addition of NO<sub>x</sub> substantially decreases HO<sub>2</sub> formation and accelerates the chemistry of HOM peroxy radicals. Hydroperoxide concentrations are low already at low particle surface and effects of HO<sub>2</sub> losses on particles are not observable.

As NO<sub>x</sub> is not efficiently lost by condensation on particles, variations of particle surface therefore do not directly affect NO<sub>x</sub> chemistry. NO<sub>x</sub> addition substantially reduces the chemical lifetime of peroxy radicals, and thus impacts of their losses on particles will be observable only at much higher particle surface. This also concerns dimer formation. Because of the shortened lifetime of HOM-RO<sub>2</sub>, dimer formation is already reduced and the impacts of condensational HOM-RO<sub>2</sub> losses on particles are substantially reduced. From this point of view it is also comprehensible that comparable plots for the  $\beta$ -pinene experiment in the presence of NO<sub>x</sub> show much less effects and no unrealistically high numbers for  $\gamma_{\text{eff}}$ .

### 6.3 Concluding remarks

The main loss processes for closed shell HOM in the chamber were condensational losses to chamber walls and existing particle surface. But, before HOMs condensate on particles, they undergo fast chemical processes hindering quantitative determination of the uptake coefficients. However, some general statements can be made. Reducing the impact of chemistry by using data sets with low impact of chemistry (i.e. lower particle surface) leads to realistic results for uptake coefficients. For HOMs with low numbers of O atoms condensational losses are less effective than for HOM monomers with higher numbers of O atoms. But even for monomers containing more than seven O atoms the uptake coefficients are not unity. For dimers the uptake coefficients are  $\sim 1$ , i.e. their condensation on particles is kinetically limited.

For a better quantification of condensational losses it is advantageous to reduce the impacts of chemistry. Nevertheless, the strong reduction in the lifetime of HOM peroxy radicals with increasing condensational sink also allows more insight into foregoing chemical processes.

Losses of peroxy radicals on SOA as found here may have implications for atmospheric chemistry. Such losses were significant already at particle surface densities around  $10^{-3} \text{ m}^2 \text{ m}^{-3}$ . This is equivalent to a mass loading of  $3 \mu\text{g m}^{-3}$  (density  $\sim 1.2$ ), a mass loading also observable in the Troposphere.

Due to the quite high OH and VOC concentrations used in these laboratory experiments, peroxy radical concentrations including those of HO<sub>2</sub> and HOM RO<sub>2</sub> were quite high. Hence, the chemical lifetimes of all these peroxy radicals might have been much shorter than in the real atmosphere. Accordingly, impacts of their losses on particle surface and therewith impacts of particles on the photochemistry in air masses with low NO<sub>x</sub> levels might be significant already at mass loadings far below those used here. However, to what extent particles impact photochemistry is unknown so far and assessment of the importance of this process requires more information also from laboratory experiments as conducted here.

## Chapter 7 Summary and Conclusions

In this work, a comprehensive overview on photochemical formation of highly oxidized multifunctional organic molecules (HOMs) was given. The focus was on the formation mechanism, end product distribution and loss mechanisms. To obtain more insight in the mechanisms, the OH dependency of HOM concentrations, effects of photochemistry on total production and end product distribution, and chemical and condensational loss processes of HOMs were studied. By these measurements it was also shown that particles can influence photochemistry of peroxy radicals.

With respect to photochemical HOM formation several experiments were conducted in order to distinguish between autoxidation and sequential OH oxidation. HOM formation was shown to be inhibited for a fully deuterated volatile organic compound compared to the hydrogenated version which showed clear HOM formation (cyclohexene-d10 and cyclohexene). As tunnelling has been reported to be an important factor enabling autoxidation, and to be repressed in deuterated compounds, this inhibition of HOM formation can be seen to give a strong implication towards autoxidation being important mechanism in photochemical HOM formation.

Furthermore the formation rates of HOM molecules with different oxidation states, i.e. different number of oxygen were studied for  $\alpha$ -pinene. If the addition of oxygen to the oxidation products of  $\alpha$ -pinene would occur in sequential OH oxidation, the formation of the product that would require higher number of OH attacks would be slower. There was no observable difference in formation rates of HOMs with lower numbers of O atoms and higher numbers of O atoms, respectively, again indicating that autoxidation is more likely to be the main oxidation mechanism in photochemical HOM formation.

Consistently there were also no substantial changes of the HOM pattern for  $\alpha$ -pinene when producing HOMs at different OH concentrations. If sequential OH oxidation would be an important HOM formation mechanism, at higher OH concentrations more HOM molecules with high number of oxygen should be formed. The finding of similar oxidation states despite of different OH concentrations was seen as additional support to the autoxidation hypothesis.

However, it was also shown that first generation oxidation products are able to form HOMs under photooxidation. HOM formation from pinonaldehyde, an important oxidation product of  $\alpha$ -pinene photooxidation, demonstrated clear HOM formation with OH, and the end product pattern was shown to be similar to that of  $\alpha$ -pinene. It was concluded that primary oxidation products (pinonaldehyde; or nopinon in case of  $\beta$ -pinene) are likely to contribute to photochemical HOM formation, however the relative importance is yet unknown.

In light of the results shown here, autoxidation seems to be more plausible formation mechanism for photochemical HOM formation. This does not exclude that each closed shell HOM can be attacked by OH and start a new autoxidation sequence.

Additional experiments were conducted to investigate how general photochemical HOM formation is. HOM formation was also found during photooxidation of  $\beta$ -pinene, benzene and methyl salicylate, compounds that react only slowly with ozone, or not at all. Consistent to the hypothesis that significant

HOM formation from ozonolysis requires an endocyclic double bond no strong HOM formation was found for  $\beta$ -pinene ozonolysis. In contrast, photooxidation led to substantial HOM formation. Similarly photooxidation of the important biogenic and anthropogenic benzenoids methyl salicylate and benzene led to strong HOM formation. As these benzenoids do not react with ozone, their HOM formation from OH induced reactions offered further evidence that a reaction with ozone is not required as a first step on photochemical HOM formation.

In an experiment where oxygen in the chamber was reduced to very low concentration ( $< 1\%$ ) without noticeable effect on photochemical HOM formation it was suggested that the autoxidation must be highly efficient. The structural differences in primary peroxy radicals formed from ozonolysis and photooxidation were hypothesized as a possible reason for the different autoxidation rates, as low oxygen concentration was shown to inhibit HOM formation during ozonolysis. As a consequence, the entrance channel in autoxidation would be affected differently comparing ozonolysis and OH reactions.

From the results of the mechanistic studies it is clear that HOM formation from photooxidation is a widely occurring phenomenon, and not as limited to specific precursors as it is in the case of ozonolysis. This is understandable as OH is less specific oxidant than ozone, and can lead to a wide variety of oxidation products.

The dependency of photochemical HOM formation on OH concentrations was shown to be non-linear, but with a linear subrange at higher oxidation rates (OH concentrations). The main end product class of monomers was shown to be hydroperoxides. Dimer formation was also an efficient termination for peroxy radical chemistry. As  $\text{HO}_2$  concentration increased with higher OH production, dimer concentration in relation to monomer concentration began to decrease. Stronger hydroperoxide formation in reactions of peroxy radicals with  $\text{HO}_2$  competed with dimer formation. However, as increased OH concentration also led to higher formation of peroxy radicals, the absolute dimer concentration was not inhibited, but instead reached a plateau. Thus only the relative importance of dimer HOMs decreased. Individual peroxy radicals showed no increase at higher OH concentrations, which was due to the higher sink strength and faster formation of termination products such as hydroperoxides and dimers.

The effects observed when varying OH concentration could be explained using basics of peroxy radical chemistry, and the behaviour observed during these experiments furthermore confirmed the assignment of HOMs as peroxy radicals, hydroperoxides, or ketones.

A photochemical yield was estimated based on the reported HOM yield from ozonolysis, and concluded to be 1.8 % - 7 %, depending of the OH concentration.

In real atmospheric systems, OH concentration is regulated by the source strength, loss reactions (e.g. reactions with  $\text{NO}_2$  or CO), and OH/ $\text{HO}_2$  recycling regulated by  $\text{NO}_x$ . Hence also effects of  $\text{NO}_x$  and CO on photochemical HOM formation were studied. When adding  $\text{NO}_x$  into the system, organic nitrates could be observed in expected masses, further validating the hypothesis of peroxy radical as a starting point for HOM formation. Increasing  $\text{NO}_x$  concentration led to an increase of organic nitrate concentration, and a decrease in hydroperoxide formation, due to both increased reactions of  $\text{HO}_2$  with NO, and higher

$\text{NO}_x$  concentration leading to increased reactions of peroxy radicals with NO or  $\text{NO}_2$ . Increased  $\text{NO}_x$  concentration also led to lower dimer concentrations, for the same reasons. In summary all HOMs followed the known pathways of peroxy radical chemistry and the chemical behaviour observed was compatible to peroxy radical chemistry. The decrease in hydroperoxides following  $\text{NO}_x$  addition suggested  $\text{HO}_2$  concentration to be important in determining peroxy radical termination.

Additional to organic nitrate formed by reactions of peroxy radicals with NO, PAN-like nitrates, following reactions of peroxy radicals with  $\text{NO}_2$ , were also detected. It was estimated that in the chamber study reported here ~60% of observed organic nitrates were in fact PAN-like nitrates. However, due to instrument limitation during main experiments the two compound classes (organic nitrates from  $\text{RO}_2\cdot + \text{NO}$  reaction and PAN-like nitrates from  $\text{RO}_2\cdot + \text{NO}_2$  reactions) could not be separated, and they were combined as “organic nitrates” and analysed together.

There were observable shifts in the HOM mass spectra in the HOM end product pattern towards higher oxidations states during  $\text{NO}_x$  addition. Part of this could be explained by the shifting of the termination pathway from hydroperoxide formation to nitrate formation, as organic nitrates and PAN-like nitrates have higher mass than the respective hydroperoxide (+30 Th or +46 Th added to the peroxy radical, compared to +1 Th with hydroperoxide). This could however not explain the entire observed shift.

Another observation that required explanation was that even at very high  $\text{NO}_x$  levels the formation of termination products of  $\text{RO}_2\cdot + \text{RO}_2\cdot$  reactions was not completely inhibited, and dimer formation could still be observed. A hypothesis to explain both these observations was that adding  $\text{NO}_x$  into the reaction system led to an activation of an alkoxy-peroxy pathway, another pathway to peroxy radical formation under  $\text{NO}_x$  regimes. It was suggested, that the  $\text{RO}\cdot$  formed from  $\text{RO}_2\cdot + \text{NO}$  reaction, instead of decomposing, undergoes internal H-shift and a subsequent  $\text{O}_2$  addition, and forms a new peroxy radical, with one oxygen atom more than the parent peroxy radical. This pathway was concluded to become more important with increasing  $\text{NO}_x$  concentrations.

The activation of alkoxy-peroxy pathway together with increased OH recycling following the increasing  $\text{NO}_x$  concentration were concluded to sufficiently explain the observed increase in HOM concentrations observed at higher  $\text{NO}_x$  concentrations.

Similarly, experiments with CO also further confirmed the assignment of peroxy radicals and termination products. The results from such experiments further suggested that  $\text{HO}_2$  has an important role in determining the fate of HOMs, including the oppression of dimer formation.

The two main loss processes for the closed shell HOMs in the reaction chamber were condensational losses to chamber walls, and condensational losses to existing particle surface. For monomer HOMs with lower oxidation state (less than six oxygen atoms) the condensational losses in general were shown to be less effective, likely due to higher vapour pressures. However, even for monomer range closed shell molecules with more than seven oxygen atoms, effective uptake coefficients were not unity. For dimers the condensation on particles was shown to be kinetically limited, with uptake coefficients close to 1.

Analysing quantitative uptake coefficients was hindered by gas phase chemical processes appearing on a similar time scale as condensation on the particles. The effects of chemistry could be reduced by limiting the analysis on data sets with lower particle surface i.e. smaller effect of chemistry, which led to realistic values. For quantification purposes it was recommended to limit the impact of chemistry by accelerating gas phase chemistry. However, the strong reduction in HOM peroxy radical lifetimes following the increase in condensational sink also offers more insight into the chemical processes. The condensational losses of peroxy radicals on SOA that were shown in this work may also have atmospheric relevance. These losses were significant already at mass loadings of approximately  $3 \mu\text{g m}^{-3}$  and higher, a realistic mass loading in Troposphere. Furthermore, as the OH and VOC concentrations used in the experiments reported here were high, peroxy radical concentrations were also higher. Their lifetimes in the reaction chamber might have been shorter than under in real atmospheric conditions in air masses with low NO<sub>x</sub> levels. Losses of peroxy radicals on particles might therefore be more important in the real atmosphere than in the reaction chamber. More detailed studies in the effect of particles on photochemistry are needed in order to further investigate the extent and importance of this finding in real atmospheric conditions.

## References

- Atkinson, R.: Gas-Phase Tropospheric Chemistry of Volatile Organic Compounds: 1. Alkanes and Alkenes, *Journal of Physical and Chemical Reference Data*, 26, 215-290, 1997.
- Berndt, T., Richters, S., Kaethner, R., Voigtlander, J., Stratmann, F., Sipila, M., Kulmala, M., and Herrmann, H.: Gas-Phase Ozonolysis of Cycloalkenes: Formation of Highly Oxidized RO<sub>2</sub> Radicals and Their Reactions with NO, NO<sub>2</sub>, SO<sub>2</sub>, and Other RO<sub>2</sub> Radicals, *J Phys Chem A*, 119, 10336-10348, 2015.
- Bianchi, F., Tröstl, J., Junninen, H., Frege, C., Henne, S., Hoyle, C. R., Molteni, U., Herrmann, H., Adamov, A., Bukowiecki, N., Chen, X., Duplissy, J., Gysel, M., Hutterli, M., Kangasluoma, J., Kontkanen, J., Kürten, A., Manninen, H. E., Münch, S., Peräkylä, O., Petäjä, T., Rondo, L., Williamson, C., Weingartner, E., Curtius, J., Worsnop, D., Kulmala, M., Dommen, J., and Baltensperger, U.: New particle formation in the free troposphere: A question of chemistry and timing, *Science*, 352, 1109-1112, 2016.
- Brune, W. H., Tan, D., Faloon, I. F., Jaeglé, I., Jacob, D. J., Heikes, B. G., Snow, J., Kondo, Y., Shetter, R., Sachse, G. W., Anderson, B., Gregory, G. L., Vay, S., Singh, H. B., Davis, D. D., Crawford, J. H., and Blake, D. R.: OH and HO<sub>2</sub> chemistry in the North Atlantic free troposphere, *Geophysical Research Letters*, 26, 3077-3080, 1999.
- Capouet, M., Peeters, J., Nozière, B., and Müller, J. F.: Alpha-pinene oxidation by OH: simulations of laboratory experiments, *Atmos. Chem. Phys.*, 4, 2285-2311, 2004.
- Carslaw, N., Creasey, D. J., Heard, D. E., Jacobs, P. J., Lee, J. D., Lewis, A. C., McQuaid, J. B., Pilling, M. J., Bauguitte, S., Penkett, S. A., Monks, P. S., and Salisbury, G.: Eastern Atlantic Spring Experiment 1997 (EASE97) 2. Comparisons of model concentrations of OH, HO<sub>2</sub>, and RO<sub>2</sub> with measurements, *Journal of Geophysical Research*, 107, ACH 5-16, 2002.
- Clement, A. C., Burgman, R., and Norris, J. R.: Observational and Model Evidence for Positive Low-Level Cloud Feedback, *Science*, 325, 460-464, 2009.
- Cox, R. A., and Cole, J. A.: Chemical aspects of the autoignition of hydrocarbon • air mixtures, *Combustion and Flame*, 60, 109-123, 1985.
- Crouse, J. D., Knap, H. C., Ørnsø, K. B., Jørgensen, S., Paulot, F., Kjaergaard, H. G., and Wennberg, P. O.: Atmospheric Fate of Methacrolein. 1. Peroxy Radical Isomerization Following Addition of OH and O<sub>2</sub>, *The Journal of Physical Chemistry A*, 116, 5756-5762, 2012.
- Crouse, J. D., Nielsen, L. B., Jørgensen, S., Kjaergaard, H. G., and Wennberg, P. O.: Autoxidation of Organic Compounds in the Atmosphere, *The Journal of Physical Chemistry Letters*, 4, 3513-3520, 2013.
- Crouse, J. D., Paulot, F., Kjaergaard, H. G., and Wennberg, P. O.: Peroxy radical isomerization in the oxidation of isoprene, *Physical Chemistry Chemical Physics : Pccp*, 13, 13607-13613, 2011.
- Davidson J.A., C. C. A., McDaniel A.H., Shetter R.E., Madronich S., Calvert J.G.: Visible ultraviolet absorption cross sections for NO<sub>2</sub> as a function of temperature, *Journal of Geophysical Research*, 93, 7105-7112, 1988.

Donahue, N. M., Epstein, S. A., Pandis, S. N., and Robinson, A. L.: A two-dimensional volatility basis set: 1. organic-aerosol mixing thermodynamics, *Atmos. Chem. Phys.*, **11**, 3303-3318, 2011.

Ehn, M., Junninen, H., Petäjä, T., Kurtén, T., Kerminen, V. M., Schobesberger, S., Manninen, H. E., Ortega, I. K., Vehkamäki, H., Kulmala, M., and Worsnop, D. R.: Composition and temporal behavior of ambient ions in the boreal forest, *Atmospheric Chemistry and Physics*, **10**, 2010.

Ehn, M., Kleist, E., Junninen, H., Petäjä, T., Lönn, G., Schobesberger, S., Dal Maso, M., Trimborn, A., Kulmala, M., Worsnop, D. R., Wahner, A., Wildt, J., and Mentel, T. F.: Gas phase formation of extremely oxidized pinene reaction products in chamber and ambient air, *Atmospheric Chemistry and Physics*, **12**, 5113-5127, 2012.

Ehn, M., Thornton, J. A., Kleist, E., Sipila, M., Junninen, H., Pullinen, I., Springer, M., Rubach, F., Tillmann, R., Lee, B., Lopez-Hilfiker, F., Andres, S., Acir, I. H., Rissanen, M., Jokinen, T., Schobesberger, S., Kangasluoma, J., Kontkanen, J., Nieminen, T., Kurten, T., Nielsen, L. B., Jorgensen, S., Kjaergaard, H. G., Canagaratna, M., Maso, M. D., Berndt, T., Petaja, T., Wahner, A., Kerminen, V. M., Kulmala, M., Worsnop, D. R., Wildt, J., and Mentel, T. F.: A large source of low-volatility secondary organic aerosol, *Nature*, **506**, 476-479, 2014.

Eisele, F. L., and Tanner, D. J.: Measurement of the gas phase concentration of H<sub>2</sub>SO<sub>4</sub> and methane sulfonic acid and estimates of H<sub>2</sub>SO<sub>4</sub> production and loss in the atmosphere, *Journal of Geophysical Research*, **98**, 9001-9010, 1993.

Finlayson-Pitts, B. J., and James N. Pitts: *Chemistry of the upper and lower atmosphere: theory, experiments, and applications*, Academic Press, San Diego, 2000.

Geyer, A.: *The role of the nitrate radical in the boundary layer - Observations and modeling studies*, Doctor of Natural Science, Combined Faculties for the Natural Science and for Mathematics, Ruperto Carola University of Heidelberg, Heidelberg, Germany, 210 pp., 2000.

Glowacki, D. R., and Pilling, M. J.: Unimolecular reactions of peroxy radicals in atmospheric chemistry and combustion, *Chemphyschem*, **11**, 3836-3843, 2010.

Guenther, A. B., Jiang, X., Heald, C. L., Sakulyanontvittaya, T., Duhl, T., Emmons, L. K., and Wang, X.: The Model of Emissions of Gases and Aerosols from Nature version 2.1 (MEGAN2.1): an extended and updated framework for modeling biogenic emissions, *Geosci. Model Dev.*, **5**, 1471-1492, 2012.

Haggerstone, A.-I., Carpenter, L. J., Carslaw, N., and McFiggans, G.: Improved model predictions of HO<sub>2</sub> with gas to particle mass transfer rates calculated using aerosol number size distributions, *Journal of Geophysical Research*, **110**, 2005.

Hallquist, M., Wenger, J. C., Baltensperger, U., Rudich, Y., Simpson, D., Claeys, M., Dommen, J., Donahue, N. M., George, C., Goldstein, A. H., Hamilton, J. F., Herrmann, H., Hoffmann, T., Iinuma, Y., Jang, M., Jenkin, M. E., Jimenez, J. L., Kiendler-Scharr, A., Maenhaut, W., McFiggans, G., Mentel, T. F., Monod, A., Prévôt, A. S. H., Seinfeld, J. H., Surratt, J. D., Szmigielski, R., and Wildt, J.: The formation, properties and impact of secondary organic aerosol: current and emerging issues, *Atmos. Chem. Phys.*, **9**, 5155-5236, 2009.

Heinritzi, M., Simon, M., Steiner, G., Wagner, A. C., Kürten, A., Hansel, A., and Curtius, J.: Characterization of the mass-dependent transmission efficiency of a CIMS, *Atmospheric Measurement Techniques*, 9, 1449-1460, 2016.

Hoffmann, T., Bandur, R., Marggraf, U., and Linscheid, M.: Molecular composition of organic aerosols formed in the  $\alpha$ -pinene/O<sub>3</sub> reaction: Implications for new particle formation processes, *Journal of Geophysical Research: Atmospheres*, 103, 25569-25578, 1998.

Hyttinen, N., Kupiainen-Maatta, O., Rissanen, M. P., Muuronen, M., Ehn, M., and Kurten, T.: Modeling the Charging of Highly Oxidized Cyclohexene Ozonolysis Products Using Nitrate-Based Chemical Ionization, *J Phys Chem A*, 119, 6339-6345, 2015.

Jimenez, J. L., Canagaratna, M. R., Donahue, N. M., Prevot, A. S., Zhang, Q., Kroll, J. H., DeCarlo, P. F., Allan, J. D., Coe, H., Ng, N. L., Aiken, A. C., Docherty, K. S., Ulbrich, I. M., Grieshop, A. P., Robinson, A. L., Duplissy, J., Smith, J. D., Wilson, K. R., Lanz, V. A., Hueglin, C., Sun, Y. L., Tian, J., Laaksonen, A., Raatikainen, T., Rautiainen, J., Vaattovaara, P., Ehn, M., Kulmala, M., Tomlinson, J. M., Collins, D. R., Cubison, M. J., Dunlea, E. J., Huffman, J. A., Onasch, T. B., Alfarra, M. R., Williams, P. I., Bower, K., Kondo, Y., Schneider, J., Drewnick, F., Borrmann, S., Weimer, S., Demerjian, K., Salcedo, D., Cottrell, L., Griffin, R., Takami, A., Miyoshi, T., Hatakeyama, S., Shimojo, A., Sun, J. Y., Zhang, Y. M., Dzepina, K., Kimmel, J. R., Sueper, D., Jayne, J. T., Herndon, S. C., Trimborn, A. M., Williams, L. R., Wood, E. C., Middlebrook, A. M., Kolb, C. E., Baltensperger, U., and Worsnop, D. R.: Evolution of organic aerosols in the atmosphere, *Science*, 326, 1525-1529, 2009.

Jokinen, T., Sipilä, M., Junninen, H., Ehn, M., Lönn, G., Hakala, J., Petäjä, T., Mauldin, R. L., Kulmala, M., and Worsnop, D. R.: Atmospheric sulphuric acid and neutral cluster measurements using CI-API-TOF, *Atmospheric Chemistry and Physics*, 12, 4117-4125, 2012.

Jokinen, T., Sipilä, M., Richters, S., Kerminen, V. M., Paasonen, P., Stratmann, F., Worsnop, D., Kulmala, M., Ehn, M., Herrmann, H., and Berndt, T.: Rapid autoxidation forms highly oxidized RO<sub>2</sub> radicals in the atmosphere, *Angew Chem Int Ed Engl*, 53, 14596-14600, 2014.

Jokinen, T.: Formation of low-volatility aerosol precursor molecules and clusters in the atmosphere, PhD thesis, Department of Physics, University of Helsinki, Helsinki, Finland, 51 pp., 2015.

Jorand, F. o., Heiss, A., Perrin, O., Sahetchian, K., Kerhoas, L., and Einhorn, J.: Isomeric hexyl-ketohydroperoxides formed by reactions of hexoxy and hexylperoxy radicals in oxygen, *International Journal of Chemical Kinetics*, 35, 354-366, 2003.

Jørgensen, S., Knap, H. C., Otkjær, R. V., Jensen, A. M., Kjeldsen, M. L. H., Wennberg, P. O., and Kjaergaard, H. G.: Rapid Hydrogen Shift Scrambling in Hydroperoxy-Substituted Organic Peroxy Radicals, *The Journal of Physical Chemistry A*, 120, 266-275, 2016.

Junninen, H., Ehn, M., Petäjä, T., Luosujärvi, L., Kotiaho, T., Kostianen, R., Rohner, U., Gonin, M., Fuhrer, K., Kulmala, M., and Worsnop, D. R.: A high-resolution mass spectrometer to measure atmospheric ion composition, *Atmospheric Measurement Techniques*, 3, 1039-1053, 2010.

Kerminen, V. M., Petäjä, T., Manninen, H. E., Paasonen, P., Nieminen, T., Sipilä, M., Junninen, H., Ehn, M., Gagné, S., Laakso, L., Riipinen, I., Vehkamäki, H., Kurten, T., Ortega, I. K., Dal Maso, M., Brus, D., Hyvärinen, A., Lihavainen, H., Leppä, J., Lehtinen, K. E. J., Mirme, A., Mirme, S., Hörrak, U., Berndt, T., Stratmann, F., Birmili, W., Wiedensohler, A., Metzger, A., Dommen, J., Baltensperger, U., Kiendler-Scharr, A., Mentel, T. F., Wildt, J., Winkler, P. M., Wagner, P. E., Petzold, A., Minikin, A., Plass-Dülmer, C., Pöschl, U., Laaksonen, A., and Kulmala, M.: Atmospheric nucleation: highlights of the EUCAARI project and future directions, *Atmos. Chem. Phys.*, 10, 10829-10848, 2010.

Kulmala, M., Vehkamäki, H., Petäjä, T., Dal Maso, M., Lauri, A., Kerminen, V. M., Birmili, W., and McMurry, P. H.: Formation and growth rates of ultrafine atmospheric particles: a review of observations, *Journal of Aerosol Science*, 35, 143-176, 2004.

Kulmala, M., Kontkanen, J., Junninen, H., Lehtipalo, K., Manninen, H. E., Nieminen, T., Petäjä, T., Sipilä, M., Schobesberger, S., Rantala, P., Franchin, A., Jokinen, T., Järvinen, E., Äijälä, M., Kangasluoma, J., Hakala, J., Aalto, P. P., Paasonen, P., Mikkilä, J., Vanhanen, J., Aalto, J., Hakola, H., Makkonen, U., Ruuskanen, T., Mauldin, R. L., Duplissy, J., Vehkamäki, H., Bäck, J., Kortelainen, A., Riipinen, I., Kurtén, T., Johnston, M. V., Smith, J. N., Ehn, M., Mentel, T. F., Lehtinen, K. E. J., Laaksonen, A., Kerminen, V.-M., and Worsnop, D. R.: Direct Observations of Atmospheric Aerosol Nucleation, *Science*, 339, 943-946, 2013.

Kurtén, T., Rissanen, M. P., Mackeprang, K., Thornton, J. A., Hyttinen, N., Jorgensen, S., Ehn, M., and Kjaergaard, H. G.: Computational Study of Hydrogen Shifts and Ring-Opening Mechanisms in alpha-Pinene Ozonolysis Products, *J Phys Chem A*, 119, 11366-11375, 2015.

Kurtén, T., Loukonen, V., Vehkamäki, H., and Kulmala, M.: Amines are likely to enhance neutral and ion-induced sulfuric acid-water nucleation in the atmosphere more effectively than ammonia, *Atmos. Chem. Phys.*, 8, 4095-4103, 2008.

Kurtén, T., Petäjä, T., Smith, J., Ortega, I. K., Sipilä, M., Junninen, H., Ehn, M., Vehkamäki, H., Mauldin, L., Worsnop, D. R., and Kulmala, M.: The effect of H<sub>2</sub>SO<sub>4</sub> - amine clustering on chemical ionization mass spectrometry (CIMS) measurements of gas-phase sulfuric acid, *Atmos. Chem. Phys.*, 11, 3007-3019, 10.5194/acp-11-3007-2011, 2011. Hallquist, M., Wenger, J. C., Baltensperger, U., Rudich, Y., Simpson, D., Claeys, M., Dommen, J., Donahue, N. M., George, C., Goldstein, A. H., Hamilton, J. F., Herrmann, H., Hoffmann, T., Iinuma, Y., Jang, M., Jenkin, M. E., Jimenez, J. L., Kiendler-Scharr, A., Maenhaut, W., McFiggans, G., Mentel, T. F., Monod, A., Prévôt, A. S. H., Seinfeld, J. H., Surratt, J. D., Szmigielski, R., and Wildt, J.: The formation, properties and impact of secondary organic aerosol: current and emerging issues, *Atmos. Chem. Phys.*, 9, 5155-5236, 2009.

Li, X., Rohrer, F., Hofzumahaus, A., Brauers, T., Häseler, R., Bohn, B., Broch, S., Fuchs, H., Gomm, S., Holland, F., Jäger, J., Kaiser, J., Keutsch, F. N., Lohse, I., Lu, K., Tillmann, R., Wegener, R., Wolfe, G. M., Mentel, T. F., Kiendler-Scharr, A., and Wahner, A.: Missing Gas-Phase Source of HONO Inferred from Zeppelin Measurements in the Troposphere, *Science*, 344, 292-296, 2014.

Loukonen, V., Kurtén, T., Ortega, I. K., Vehkamäki, H., Pádua, A. A. H., Sellegri, K., and Kulmala, M.: Enhancing effect of dimethylamine in sulfuric acid nucleation in the presence of water – a computational study, *Atmos. Chem. Phys.*, 10, 4961-4974, 2010.

Mentel, T. F., Wildt, J., Kiendler-Scharr, A., Kleist, E., Tillmann, R., Dal Maso, M., Fisseha, R., Hohaus, T., Spahn, H., Uerlings, R., Wegener, R., Griffiths, P. T., Dinar, E., Rudich, Y., and Wahner, A.: Photochemical production of aerosols from real plant emissions, *Atmos. Chem. Phys.*, 9, 4387-4406, 2009.

Mentel, T. F., Springer, M., Ehn, M., Kleist, E., Pullinen, I., Kurtén, T., Rissanen, M., Wahner, A., and Wildt, J.: Formation of highly oxidized multifunctional compounds: autoxidation of peroxy radicals formed in the ozonolysis of alkenes – deduced from structure–product relationships, *Atmos. Chem. Phys.*, 15, 6745-6765, 2015.

Metzger, A., Verheggen, B., Dommen, J., Duplissy, J., Prevot, A. S., Weingartner, E., Riipinen, I., Kulmala, M., Spracklen, D. V., Carslaw, K. S., and Baltensperger, U.: Evidence for the role of organics in aerosol particle formation under atmospheric conditions, *Proc Natl Acad Sci U S A*, 107, 6646-6651, 2010.

Nel, A.: Air pollution related illness effects of particles, *Science*, 308, 804-806, 2005.

Orlando, J. J., and Tyndall, G. S.: Laboratory studies of organic peroxy radical chemistry: an overview with emphasis on recent issues of atmospheric significance, *Chem Soc Rev*, 41, 6294-6317.

Ortega, I. K., Donahue, N. M., Kurten, T., Kulmala, M., Focsa, C., and Vehkamäki, H.: Can Highly Oxidized Organics Contribute to Atmospheric New Particle Formation?, *J Phys Chem A*, 120, 1452-1458, 2016.

Paasonen, P., Nieminen, T., Asmi, E., Manninen, H. E., Petäjä, T., Plass-Dülmer, C., Flentje, H., Birmili, W., Wiedensohler, A., Hörrak, U., Metzger, A., Hamed, A., Laaksonen, A., Facchini, M. C., Kerminen, V. M., and Kulmala, M.: On the roles of sulphuric acid and low-volatility organic vapours in the initial steps of atmospheric new particle formation, *Atmospheric Chemistry and Physics*, 10, 11223-11242, 2010.

Paasonen, P., Olenius, T., Kupiainen, O., Kurtén, T., Petäjä, T., Birmili, W., Hamed, A., Hu, M., Huey, L. G., Plass-Duelmer, C., Smith, J. N., Wiedensohler, A., Loukonen, V., McGrath, M. J., Ortega, I. K., Laaksonen, A., Vehkamäki, H., Kerminen, V. M., and Kulmala, M.: On the formation of sulphuric acid & amine clusters in varying atmospheric conditions and its influence on atmospheric new particle formation, *Atmos. Chem. Phys.*, 12, 9113-9133, 2012.

Peeters, J., Vereecken, L., and Fantechi, G.: The detailed mechanism of the OH-initiated atmospheric oxidation of [small alpha]-pinene: a theoretical study, *Physical Chemistry Chemical Physics*, 3, 5489-5504, 2001.

Perrin, O., Heiss, A., Sahetchian, K., Kerhoas, L., and Einhorn, J.: Determination of the isomerization rate constant  $\text{HOCH}_2\text{CH}_2\text{CH}_2\text{CH}(\text{OO}\cdot)\text{CH}_3 \rightarrow \text{HOC-HCH}_2\text{CH}_2\text{CH}(\text{OOH})\text{CH}_3$ . Importance of intramolecular hydroperoxy isomerization in tropospheric chemistry, *International Journal of Chemical Kinetics*, 30, 875-887, 1998.

Riccobono, F., Schobesberger, S., Scott, C. E., Dommen, J., Ortega, I. K., Rondo, L., Almeida, J., Amorim, A., Bianchi, F., Breitenlechner, M., David, A., Downard, A., Dunne, E. M., Duplissy, J., Ehrhart, S., Flagan, R. C., Franchin, A., Hansel, A., Junninen, H., Kajos, M., Keskinen, H., Kupc, A., Kürten, A., Kvashin, A. N., Laaksonen, A., Lehtipalo, K., Makhmutov, V., Mathot, S., Nieminen, T., Onnela, A., Petäjä, T., Praplan, A. P., Santos, F. D., Schallhart, S., Seinfeld, J. H., Sipilä, M., Spracklen, D. V., Stozhkov, Y., Stratmann, F., Tomé, A., Tsigogeorgas, G., Vaattovaara, P., Viisanen, Y., Vrtala, A., Wagner, P. E., Weingartner, E.,

Wex, H., Wimmer, D., Carslaw, K. S., Curtius, J., Donahue, N. M., Kirkby, J., Kulmala, M., Worsnop, D. R., and Baltensperger, U.: Oxidation Products of Biogenic Emissions Contribute to Nucleation of Atmospheric Particles, *Science*, 344, 717-721, 2014.

Riipinen, I., Pierce, J. R., Yli-Juuti, T., Nieminen, T., Häkkinen, S., Ehn, M., Junninen, H., Lehtipalo, K., Petäjä, T., Slowik, J., Shantz, N. C., Abbatt, J., Leaitch, W. R., Kerminen, V. M., Worsnop, D., Pandis, S. N., Donahue, N. M., and Kulmala, M.: organic condensation: a vital link connecting aerosol formation to cloud condensation nuclei (CCN) concentrations, *Atmos. Chem. Phys.*, 11, 3865-3878, 2011.

Riipinen, I., Yli-Juuti, T., Pierce, J. R., Petäjä, T., Worsnop, D. R., Kulmala, M., and Donahue, N. M.: The contribution of organics to atmospheric nanoparticle growth, *Nature Geoscience*, 5, 453-458, 2012.

Rissanen, M. P., Kurten, T., Sipilä, M., Thornton, J. A., Kausiala, O., Garmash, O., Kjaergaard, H. G., Petaja, T., Worsnop, D. R., Ehn, M., and Kulmala, M.: Effects of chemical complexity on the autoxidation mechanisms of endocyclic alkene ozonolysis products: from methylcyclohexenes toward understanding alpha-pinene, *J Phys Chem A*, 119, 4633-4650, 2015.

Rosenfeld, D., Lohmann, U., Raga, G. B., O'Dowd, C. D., Kulmala, M., Fuzzi, S., Reissell, A., and Andreae, M. O.: Flood or Drought: How Do Aerosols Affect Precipitation?, *Science*, 321, 1309-1313, 2008.

Sarrafzadeh, M., Wildt, J., Pullinen, I., Springer, M., Kleist, E., Tillmann, R., Schmitt, S. H., Wu, C., Mentel, T. F., Hastie, D. R., and Kiendler-Scharr, A.: Impact of NO<sub>x</sub> and OH on secondary organic aerosol (SOA) formation from β-pinene photooxidation, *Atmos. Chem. Phys. Discuss.*, 2016, 1-30, 2016.

Schobesberger, S., Junninen, H., Bianchi, F., Lonn, G., Ehn, M., Lehtipalo, K., Dommen, J., Ehrhart, S., Ortega, I. K., Franchin, A., Nieminen, T., Riccobono, F., Hutterli, M., Duplissy, J., Almeida, J., Amorim, A., Breitenlechner, M., Downard, A. J., Dunne, E. M., Flagan, R. C., Kajos, M., Keskinen, H., Kirkby, J., Kupc, A., Kurten, A., Kurten, T., Laaksonen, A., Mathot, S., Onnela, A., Praplan, A. P., Rondo, L., Santos, F. D., Schallhart, S., Schnitzhofer, R., Sipilä, M., Tome, A., Tsagkogeorgas, G., Vehkamäki, H., Wimmer, D., Baltensperger, U., Carslaw, K. S., Curtius, J., Hansel, A., Petaja, T., Kulmala, M., Donahue, N. M., and Worsnop, D. R.: Molecular understanding of atmospheric particle formation from sulfuric acid and large oxidized organic molecules, *Proc Natl Acad Sci U S A*, 110, 17223-17228, 2013.

Seinfeld, J. H., and Pankow, J. F.: Organic atmospheric particulate material, *Annual Review of Physical Chemistry*, 54, 121-140, 2003.

Sipilä, M., Berndt, T., Petäjä, T., Brus, D., Vanhanen, J., Stratmann, F., Patokoski, J., Mauldin, R. L., Hyvärinen, A.-P., Lihavainen, H., and Kulmala, M.: The Role of Sulfuric Acid in Atmospheric Nucleation, *Science*, 327, 1243-1246, 2010.

Tröstl, J., Chuang, W. K., Gordon, H., Heinritzi, M., Yan, C., Molteni, U., Ahlm, L., Frege, C., Bianchi, F., Wagner, R., Simon, M., Lehtipalo, K., Williamson, C., Craven, J. S., Duplissy, J., Adamov, A., Almeida, J., Bernhammer, A. K., Breitenlechner, M., Brilke, S., Dias, A., Ehrhart, S., Flagan, R. C., Franchin, A., Fuchs, C., Guida, R., Gysel, M., Hansel, A., Hoyle, C. R., Jokinen, T., Junninen, H., Kangasluoma, J., Keskinen, H., Kim, J., Krapf, M., Kurten, A., Laaksonen, A., Lawler, M., Leiminger, M., Mathot, S., Mohler, O., Nieminen, T., Onnela, A., Petaja, T., Piel, F. M., Miettinen, P., Rissanen, M. P., Rondo, L., Sarnela, N., Schobesberger, S., Sengupta, K., Sipilä, M., Smith, J. N., Steiner, G., Tome, A., Virtanen, A., Wagner, A. C., Weingartner,

E., Wimmer, D., Winkler, P. M., Ye, P., Carslaw, K. S., Curtius, J., Dommen, J., Kirkby, J., Kulmala, M., Riipinen, I., Worsnop, D. R., Donahue, N. M., and Baltensperger, U.: The role of low-volatility organic compounds in initial particle growth in the atmosphere, *Nature*, 533, 527-531, 2016.

Vereecken, L., and Peeters, J.: A structure-activity relationship for the rate coefficient of H-migration in substituted alkoxy radicals, *Phys Chem Chem Phys*, 12, 12608-12620, 2010.

Vereecken, L., and Francisco, J. S.: Theoretical studies of atmospheric reaction mechanisms in the troposphere, *Chem Soc Rev*, 41, 6259-6293, 2012.

Wang, L., Khalizov, A. F., Zheng, J., Xu, W., Ma, Y., Lal, V., and Zhang, R.: Atmospheric nanoparticles formed from heterogeneous reactions of organics, *Nature Geoscience*, 3, 238-242, 2010.

Wayne, R. P.: *Chemistry of Atmospheres: An Introduction to the Chemistry of the Atmospheres of Earth, the Planets, and their Satellites*, 3rd Edition, Oxford University Press, New York, 697 pp., 2006.

Weber, R. J., Marti, J. J., McMurry, P. H., Eisele, F. L., Tanner, D. J., and Jefferson, A.: Measured atmospheric new particle formation rates: implications for nucleation mechanisms, *Chemical Engineering Communications*, 151, 53-64, 1996.

Wildt, J., Mentel, T. F., Kiendler-Scharr, A., Hoffmann, T., Andres, S., Ehn, M., Kleist, E., M $\ddot{u}$ sgen, P., Rohrer, F., Rudich, Y., Springer, M., Tillmann, R., and Wahner, A.: Suppression of new particle formation from monoterpene oxidation by NO $_x$ , *Atmospheric Chemistry and Physics Discussions*, 13, 25827-25870, 2013.

Yu, F., Turco, R. P., and K $\ddot{a}$ rcher, B.: The possible role of organics in the formation and evolution of ultrafine aircraft particles, *Journal of Geophysical Research: Atmospheres*, 104, 4079-4087, 1999.

Zhang, R., Suh, I., Zhao, J., Zhang, D., Fortner, E. C., Tie, X., Molina, L. T., and Molina, M. J.: Atmospheric New Particle Formation Enhanced by Organic Acids, *Science*, 304, 1487-1490, 2004.

## Appendix

Table A1 List of identified monomer range compounds from  $\alpha$ -pinene photochemical HOM formation

Unit mass [Th]	Detection mass (with NO <sub>3</sub> <sup>-</sup> ) [Th]	Absolute mass (Th)	Chemical formula	Compound group
246	308.05362		C <sub>10</sub> H <sub>14</sub> O <sub>7</sub>	ketone
247	309.2272		C <sub>10</sub> H <sub>15</sub> O <sub>7</sub> <sup>·</sup>	peroxy radical
248	310.07261		C <sub>10</sub> H <sub>16</sub> O <sub>7</sub>	hydroperoxide
250	312.09568		C <sub>10</sub> H <sub>18</sub> O <sub>7</sub>	
262	324.05278		C <sub>10</sub> H <sub>14</sub> O <sub>8</sub>	ketone
263	325.2267		C <sub>10</sub> H <sub>15</sub> O <sub>8</sub> <sup>·</sup>	peroxy radical
264	326.07055		C <sub>10</sub> H <sub>16</sub> O <sub>8</sub>	hydroperoxide
266	328.08808		C <sub>10</sub> H <sub>18</sub> O <sub>8</sub>	
277	339.23		C <sub>10</sub> H <sub>15</sub> O <sub>7</sub> NO	organic nitrate
278	340.04751		C <sub>10</sub> H <sub>14</sub> O <sub>9</sub>	ketone
279	341.2260		C <sub>10</sub> H <sub>15</sub> O <sub>9</sub> <sup>·</sup>	peroxy radical
280	342.0672		C <sub>10</sub> H <sub>16</sub> O <sub>9</sub>	hydroperoxide
282	344.0829		C <sub>10</sub> H <sub>18</sub> O <sub>9</sub>	
293	355.23		C <sub>10</sub> H <sub>15</sub> O <sub>8</sub> NO	organic nitrate
294	356.04374		C <sub>10</sub> H <sub>14</sub> O <sub>10</sub>	ketone
295	357.2254		C <sub>10</sub> H <sub>15</sub> O <sub>10</sub> <sup>·</sup>	peroxy radical
296	358.05391		C <sub>10</sub> H <sub>16</sub> O <sub>10</sub>	hydroperoxide
298	360.08408		C <sub>10</sub> H <sub>18</sub> O <sub>10</sub>	
309	371.23		C <sub>10</sub> H <sub>15</sub> O <sub>9</sub> NO	organic nitrate
310	372.03955		C <sub>10</sub> H <sub>14</sub> O <sub>11</sub>	ketone
311	373.2249		C <sub>10</sub> H <sub>15</sub> O <sub>11</sub> <sup>·</sup>	peroxy radical
312	374.0476		C <sub>10</sub> H <sub>16</sub> O <sub>11</sub>	hydroperoxide
314	376.07256		C <sub>10</sub> H <sub>18</sub> O <sub>11</sub>	
325	387.23		C <sub>10</sub> H <sub>15</sub> O <sub>10</sub> NO	organic nitrate
326	388.0363		C <sub>10</sub> H <sub>14</sub> O <sub>12</sub>	ketone
327	389.2242		C <sub>10</sub> H <sub>15</sub> O <sub>12</sub> <sup>·</sup>	peroxy radical

328	390.04709		$C_{10}H_{16}O_{12}$	hydroperoxide
330	392.07722		$C_{10}H_{18}O_{12}$	
341	403.23		$C_{10}H_{15}O_{11}NO$	organic nitrate

Table A2 List of identified monomer range compounds from  $\beta$ -pinene photochemical HOM formation. Organic nitrates are not included. Only two radical progressions are included, one from  $\beta$ -pinene photooxidation ( $C_{10}H_{17}O_x$ ) and one from nopinone photooxidation ( $C_9H_{13}O_y$ ).

Unit mass [Th]	Detection mass (with $NO_3^-$ ) [Th]	Absolute mass [Th]	Chemical formula	Compound group
308	308.05362		$C_{10}H_{14}O_7$	
310	310.03726		$C_9H_{12}O_8$	
310	310.07261		$C_{10}H_{16}O_7$	
311	311.2000		$C_9H_{13}O_8$	
311	311.2431		$C_{10}H_{17}O_7$	
312	311.98534		$C_7H_6O_{10}$	
312	312.0527		$C_9H_{14}O_8$	
312	312.09568		$C_{10}H_{18}O_7$	
314	314.02934		$C_8H_{12}O_9$	
314	314.07317		$C_9H_{16}O_8$	
322	322.04554		$C_{10}H_{12}O_8$	
324	324.05278		$C_{10}H_{14}O_8$	
326	325.96555		$C_8H_8O_{10}$	
326	326.03234		$C_9H_{12}O_9$	
326	326.07055		$C_{10}H_{16}O_8$	
327	327.1994		$C_9H_{13}O_9$	
327	327.2425		$C_{10}H_{17}O_8$	
328	327.99805		$C_8H_{10}O_{10}$	
328	328.0486		$C_9H_{14}O_9$	
328	328.08808		$C_{10}H_{18}O_8$	
330	330.03443		$C_8H_{12}O_{10}$	
330	330.08141		$C_9H_{16}O_9$	
340	340.04751		$C_{10}H_{14}O_9$	
343	343.1988		$C_9H_{14}O_{10}$	
344	344.05327		$C_9H_{14}O_{10}$	

346	346.01974		$C_8H_{12}O_{11}$	
346	346.07375		$C_9H_{16}O_{10}$	
355	355.2095		$C_{10}H_{13}O_{10}$	
356	356.04374		$C_{10}H_{14}O_{10}$	
358	358.00496		$C_9H_{12}O_{11}$	
358	358.05391		$C_{10}H_{16}O_{10}$	
359	359.1983		$C_9H_{13}O_{11}$	
359	359.2413		$C_{10}H_{17}O_{10}$	
360	360.02861		$C_9H_{14}O_{11}$	
360	360.08408		$C_{10}H_{18}O_{10}$	
362	362.00413		$C_8H_{12}O_{12}$	
362	362.07572		$C_9H_{16}O_{11}$	
371			$C_{10}H_{13}O_{11}$	
371	375.2407		$C_{10}H_{17}O_{11}$	
372	372.03955		$C_{10}H_{14}O_{11}$	
374	374.0476		$C_{10}H_{16}O_{11}$	
376	376.07256		$C_{10}H_{18}O_{11}$	
378	377.99716		$C_8H_{12}O_{13}$	
378	378.08761		$C_9H_{16}O_{12}$	
389	391.2401		$C_{10}H_{17}O_{12}$	
390	390.04709		$C_{10}H_{16}O_{12}$	
392	392.07722		$C_{10}H_{18}O_{12}$	

Table A3 List of identified monomer range compounds from cyclohexene photochemical HOM formation

Unit mass [Th]	Detection mass (with NO <sub>3</sub> ) [Th]	Absolute mass (Th)	Chemical formula	Compound group
191	253.0075	191.0191	C <sub>6</sub> H <sub>7</sub> O <sub>7</sub>	Peroxy radical
192	254.0154	192.0270	C <sub>6</sub> H <sub>8</sub> O <sub>7</sub>	Hydroperoxide
207	269.0025	207.0141	C <sub>6</sub> H <sub>7</sub> O <sub>8</sub>	Peroxy radical
208	270.0103	208.0219	C <sub>6</sub> H <sub>8</sub> O <sub>8</sub>	Hydroperoxide
223	284.9974	223.0090	C <sub>6</sub> H <sub>7</sub> O <sub>9</sub>	Peroxy radical
224	286.0052	224.0168	C <sub>6</sub> H <sub>8</sub> O <sub>9</sub>	Hydroperoxide

Table A4 Rate coefficients for VOC used in this study. Cyclohexene-d10 not included.

VOC	k <sub>OH</sub>	k <sub>O<sub>3</sub></sub>
α-pinene	5.37 · 10 <sup>-11</sup>	8.66 · 10 <sup>-17</sup>
β-pinene	8.19 · 10 <sup>-11</sup>	1.50 · 10 <sup>-17</sup>
cyclohexene	6.10 · 10 <sup>-11</sup>	8.40 · 10 <sup>-17</sup>
benzene	1.23 · 10 <sup>-12</sup>	-
MeSA	3.12 · 10 <sup>-12</sup>	-

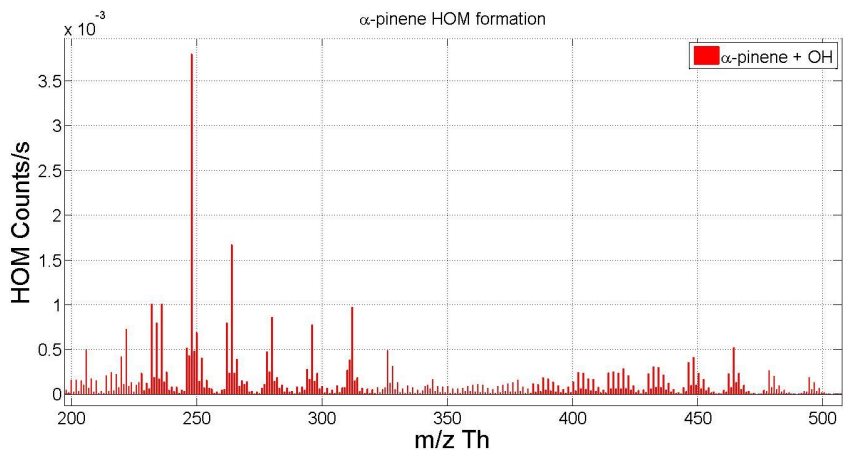


Figure A1. Example mass spectrum from α-pinene photochemical HOM formation entire HOM range.

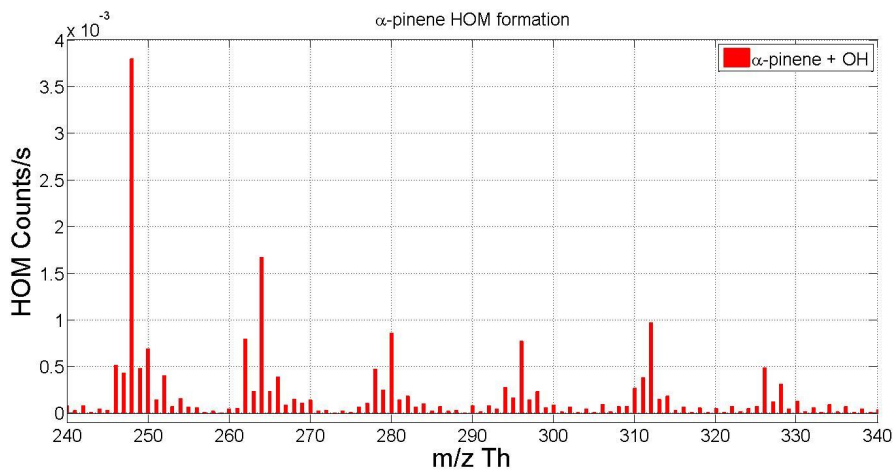


Figure A2. Example mass spectrum from α-pinene photochemical HOM formation monomer range.

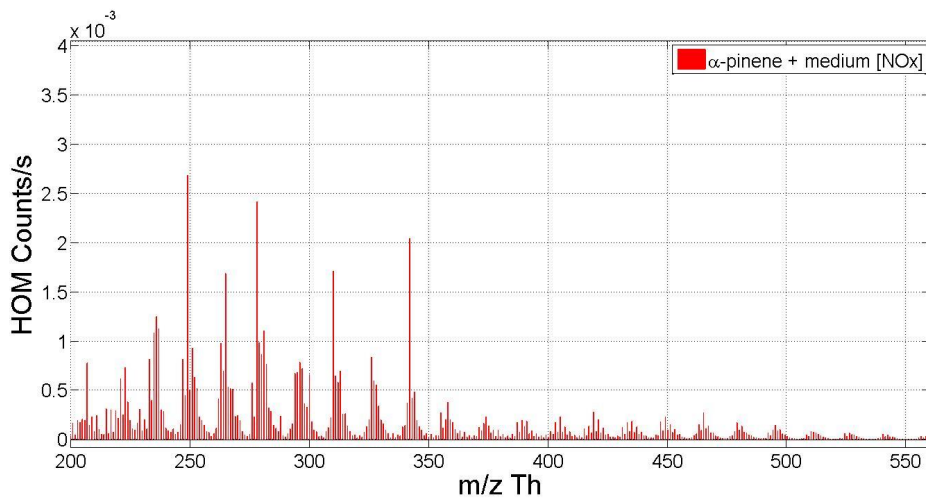


Figure A3. Example mass spectrum from  $\alpha$ -pinene photochemical HOM formation with  $\text{NO}_x$  entire HOM range.

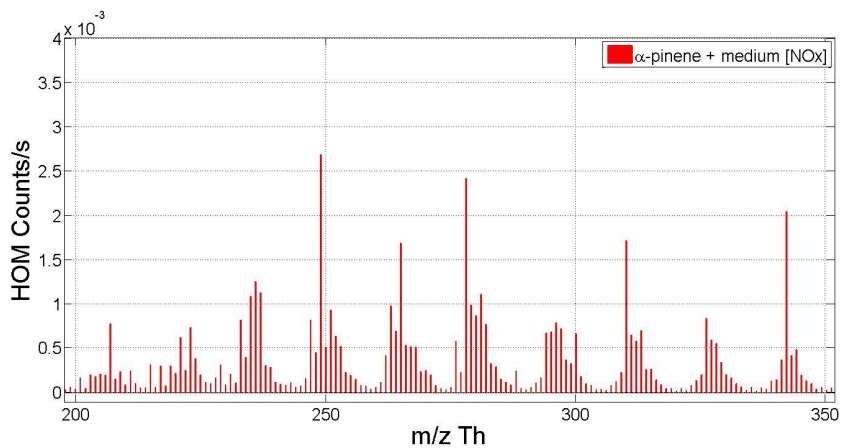


Figure A4. Example mass spectrum from  $\alpha$ -pinene photochemical HOM formation with  $\text{NO}_x$  monomer range.

## Abbreviations

$\gamma_{\text{eff}}$	effective uptake coefficient
AMS	Aerosol Mass Spectrometer (Aerodyne Research, Inc.)
API-TOF-MS	Atmospheric Pressure time-of-flight Mass Spectrometer
BVOCs	biogenic volatile organic compounds
CCN	cloud condensation nuclei
CIMS	Chemical Ionization Mass Spectrometer
CO	carbon monoxide
CSTR	continuously stirred tank reactor
ELVOC	extremely low volatility organic compound
GC-SM	Gas-Chromatography – Mass Spectrometer
HOM	highly oxidized multifunctional organic molecule
$J(\text{O}^1\text{D})$	$\text{O}_3$ photolysis frequencies
JPAC	Jülich Plant Atmosphere Chamber
$L_p$	HOM loss rate on particles
LVOC	low-volatile organic compound
MT	monoterpene
$\text{NO}_x$	nitrous oxides; $\text{NO} + \text{NO}_2$
NPF	new particle formation
$\text{O}_3$	ozone
OH	hydroxyl radical
ppb	parts per billion
ppm	parts per million
ppt	parts per trillion
PTR-Q-MS	Proton Transfer Reaction- quadrupole – Mass spectrometer

PTR-TOF-MS	Proton Transfer Reaction- time-of-flight – Mass spectrometer
RH	relative humidity
SA	sulfuric acid
SOA	Secondary Organic Aerosol
SVOC	semi-volatile organic compound
RO <sub>2</sub>	peroxy radical
RO	alkoxy radical
T	temperature
UV-C	UV lamp to produce OH
UV-A	UV lamp to photolyse NO <sub>2</sub> into NO
VOC	volatile organic compound

## Acknowledgements

This work would not have been possible if not for so many people.

I would like to offer my gratitude for Prof. Dr. Andreas Wahner for accepting the supervision of this thesis and for valuable advice during writing.

I would as well like to thank Dr. Mathias Schäfer for accepting the role of the second examiner of my work.

I want to thank both Prof. Dr. Wahner and Prof. Dr. Astrid Kiendler-Scharr for providing an opportunity to work at the Forschungszentrum Jülich.

To PD Dr. Thomas Mentel, for the supervision, guidance, discussions, and all the possible help I have received during my PhD work, and during writing. This would not have been possible without his help.

I must also acknowledge and offer my gratitude for the huge amount of help and supervision I got from PD Dr. Jürgen Wildt during my work and writing. Without his patient help and input I don't think this would ever have happened.

I want to express my gratitude for Dr. Mikael Ehn, for invaluable help and guidance during my entire work, and for patiently answering all my questions about the CIMS, as well as for offering input on data analysis.

For Dr. Einhard Kleist, I want to offer my thanks for the help with the chamber before and during experiments, and discussions regarding results and data analysis.

Additionally, I want to express my gratitude to all the plant chamber crew: Monika Springer and Stefanie Andres for all the grunt work they did around the lab; Lina Hacker for help during the experiments, and all her offerings of support and entertainment; Dr. Cheng Wu for her help and patients during our stay in the lab and during my writing; and Dr. Tinal Kasal and Sebastian Schmitt for their help and support during my experiments.

I also wish to thank all members of IEK-8, past and present, who helped and encouraged me during my PhD work. Especially Dr. Florian Rubach for the invaluable help during my first months with a barely known instrument, and the encouragement he offered during that time and after. I want to thank Dr. Ralf Tillmann for the help with PTR-MS; Dr. Franz Rohrer and Joachim Borchardt for the help with the  $\text{NO}_x$  measurements, and Dr. Defeng Zhao for the help with particle experiments.



## Erklärung

Ich versichere, dass ich die von mir vorgelegte Dissertation selbständig angefertigt, die benutzten Quellen und Hilfsmittel vollständig angegeben und die Stellen der Arbeit – einschließlich Tabellen, Karten und Abbildungen –, die anderen Werken im Wortlaut oder dem Sinn nach entnommen sind, in jedem Einzelfall als Entlehnung kenntlich gemacht habe; dass diese Dissertation noch einer anderen Fakultät oder Universität zur Prüfung vorgelegen hat; dass sie – abgesehen von unten angegebenen Teilpublikationen – noch nicht veröffentlicht worden ist sowie, dass ich eine solche Veröffentlichung vor Abschluss des Promotionsverfahrens nicht vornehmen werde. Die Bestimmungen der Promotionsordnung sind mir bekannt. Die von mir vorgelegte Dissertation ist von Prof. Dr. A. Wahner betreut worden.

Kuopio, den 14.9.2017

lida Pullinen



Band / Volume 373

**Chemical and physical properties of sodium ionic conductors for solid-state batteries**

M. Guin (2017), ix, 126 pp  
ISBN: 978-3-95806-229-0

Band / Volume 374

**Prediction of Oxidation Induced Life Time for FCC Materials at High Temperature Operation**

R. Duan (2017), vi, 180 pp  
ISBN: 978-3-95806-230-6

Band / Volume 375

**Microstructure Evolution of Laves Phase Strengthened Ferritic Steels for High Temperature Applications**

J. K. Lopez Barrilao (2017), XVI, 134 pp  
ISBN: 978-3-95806-231-3

Band / Volume 376

**Drying front formation in topmost soil layers as evaporative restraint  
Non-invasive monitoring by magnetic resonance and numerical simulation**

S. Merz (2017), xxii, 108 pp  
ISBN: 978-3-95806-234-4

Band / Volume 377

**Low Temperature Thin-Film Silicon Solar Cells on Flexible Plastic Substrates**

K. Wilken (2017), 194 pp  
ISBN: 978-3-95806-235-1

Band / Volume 378

**Dissolution Behaviour of Innovative Inert Matrix Fuels for Recycling of Minor Actinides**

E. L. Mühr-Ebert (2017), xii, 164 pp  
ISBN: 978-3-95806-238-2

Band / Volume 379

**Charakterisierung und Modifizierung von Kupferoxid- und Kupfersulfid-Nanopartikeln für Dünnschichtszell**

J. Flohre (2017), 141, iii pp  
ISBN: 978-3-95806-241-2

Band / Volume 380

**Einzelfaserkomposite aus Pulvermetallurgischem Wolfram-faserverstärktem Wolfram**

B. Jasper (2017), v, 92, XVIII pp  
ISBN: 978-3-95806-248-1

Band / Volume 381

**Untersuchungen zur Deckschichtbildung auf  $\text{LiNi}_{0,5}\text{Mn}_{1,5}\text{O}_4$ -  
Hochvoltkathoden**

Die Kathoden/Elektrolyt-Grenzfläche in Hochvolt-Lithium-Ionen-Batterien

K. Wedlich (2017), xvi, 157, xvii-xxvi pp

ISBN: 978-3-95806-249-8

Band / Volume 382

**Charakterisierung gradierter Eisen/Wolfram-Schichten  
für die erste Wand von Fusionsreaktoren**

S. Heuer (2017), x, 234 pp

ISBN: 978-3-95806-252-8

Band / Volume 383

**High resolution imaging and modeling of aquifer structure**

N. Güting (2017), viii, 107 pp

ISBN: 978-3-95806-253-5

Band / Volume 384

**IEK-3 Report 2017**

Sektorkopplung –

Forschung für ein integriertes Energiesystem

(2017), 182 pp

ISBN: 978-3-95806-256-6

Band / Volume 385

**Bestimmung der Wolframerosion mittels optischer Spektroskopie  
unter ITER-relevanten Plasmabedingungen**

M. Laengner (2017), vi, 184, XI pp

ISBN: 978-3-95806-257-3

Band / Volume 386

**IEK-3 Report 2017**

Sector Coupling –

Research for an Integrated Energy System

(2017), 175 pp

ISBN: 978-3-95806-258-0

Band / Volume 387

**Photochemistry of Highly Oxidized Multifunctional Organic Molecules:  
a Chamber Study**

L. I. M. Pullinen (2017), II, 96, xviii pp

ISBN: 978-3-95806-260-3

Weitere **Schriften des Verlags im Forschungszentrum Jülich** unter

<http://www.zb1.fz-juelich.de/verlagextern1/index.asp>



**Energie & Umwelt /  
Energy & Environment  
Band / Volume 387  
ISBN 978-3-95806-260-3**

